Effect of Chemical Reaction Rates on Aero-heating Prediction in Re-entry Flows

A thesis submitted in partial fulfillment of
the requirements for the degree of

Doctor of Philosophy

by

D. Siva Krishna Reddy
(Roll No. 06401001)

Under the guidance of
Prof. Krishnendu Sinha
and
Prof. Viren Menezes

Department of Aerospace Engineering
INDIAN INSTITUTE OF TECHNOLOGY–BOMBAY
2012

To all those persons and incidents who and which incultivated scientic curacity; inspired me to take up doctorial studies and motivated me during the thesis work.

Thesis Approval

The thesis entitled

Effect of Chemical Reaction Rates on Aero-heating Prediction in Re-entry Flows

by

D. Siva Krishna Reddy
(Roll No. 06401001)

is approved for the degree of

Doctor of Philosophy

Examiner

Examiner

Guide

Co Guide

Chairman

Date: 17-09-2012

Place: IIT Bombay

Declaration

I declare that this written submission represents my ideas in my own words and where others ideas or words have been included, I have adequately cited and referenced the original sources. I also declare that I have adhered to all principles of academic honesty and integrity and I have not misrepresented of fabricated or falsified any idea/data/fact/source in my submission. I understand that any violation of the above will be cause for disciplinary action by the institute and can also evoke panel action from the sources which have thus not been properly cited or from whom proper permission has not been taken when needed.

D. Siva Krishna Reddy

(Signature)

D. Siva Krishna Reddy

(Name of the student)

Roll No: 06401001

September 2012

Abstract

A re-entry capsule encounters a high temperature and chemically reacting flow during the re-entry phase. Computational Fluid Dynamics is extensively used to simulate these flows, as high enthalpy and low density associated with the flight conditions are difficult to reproduce in wind tunnels or shock tunnels at each re-entry trajectory point. Flowfield solution and surface predictions, such as surface heat flux and pressure, at these conditions are sensitive to chemical reaction rate constants used in the simulation. Uncertainty in the rate constants, which is inherent in their measurement, induces corresponding changes in the surface properties. Understanding the role of rate constants on the flow solution and the associated surface predictions is important.

The present thesis investigates the effect of variation in chemical reaction rate constants on aero-thermal predictions at flight conditions. With in this scope, numerical simulations are performed by varying the reaction rate constants over their uncertainty range. Freestream conditions at 35 km, 62 km and 70 km condition are chosen as the test cases. They represent typical low, intermediate and high altitude flight in the earth atmosphere. These conditions are chosen so that the effects of freestream density and stagnation enthalpy on the heating rate variations can be examined. The computations are performed with an in-house CFD code and the aero-thermal predictions are validated against available flight data. Flowfield solutions are computed by altering the reaction rates from their baseline values and they are carefully analyzed to understand the physical effects that influence the surface heat transfer rate. A controlled zonal analysis is performed to isolate the effects of shock-layer and boundary-layer chemistry on heat flux variations. The analysis is performed at different points along the vehicle forebody, afterbody and shoulder.

It is found that the dominant chemical reactions in the gas mixture; chemical state of the gas, i.e. equilibrium, frozen and non-equilibrium; and the extent of recombination reactions at the vehicle surface are the critical factors that influence the heat flux variations due to the

uncertainty in the reaction rate constants. The stagnation enthalpy of the flow determines the dominant reactions to which the surface heating rate is sensitive. On the other hand, the gas density determines the chemical state of the gas, which in turn affects the magnitude of heating rate variations. In general increasing the reaction rates enhances the recombination reactions in the boundary layer that leads to higher surface heat flux. An opposite effect is observed when the rate constants are decreased. When the gas is in chemical equilibrium state, increasing the rate constants further has a small effect on the surface heating rate. On the other hand, when the gas is in non-equilibrium state, increase or decrease of rate constants can lead to large changes in the heat flux predictions. These trends are studied in the three test cases outlined above. The results are then extrapolated to cover the entire range of Earth-reentry trajectory points with stagnation enthalpy between 2 MJ/kg and 32 MJ/kg.

Keywords: Re-entry flows, Computational fluid dynamics, Thermo-chemical non-equilibrium, Chemical reaction rate constants.

Contents

List of Tables

List of Figures

Nomenclature

English Symbols

A_{sr}	A coefficient in the calculation of Landau-Teller inter-species relaxation time
A_s	A coefficient in the Blottner viscosity model
A‘	Jacobian of flux vector
a	Speed of sound
$\tilde{a}$	Favre averaged mean speed of sound
B_s	A coefficient in the calculation of mixture viscosity using Blottner model
C_f	A coefficient in the calculation of a chemical reaction rate
C_s	A coefficient in the Blottner viscosity model
c_p	Specific heat of gas at constant pressure
c_s	Mass fraction of species s
c_v	Specific heat of gas at constant volume
$c_{v\ rot\ s}$	Rotational specific heat of species s at constant volume
c_{vs}	Translational-rotational specific heat of species s at constant volume
$c_{v\ tra\ s}$	Translational specific heat of species s at constant volume
D	Diffusion coefficient of mixture
D_s	Diffusion coefficient of species s
D_T	Turbulent diffusion coefficient
E	Total energy of the mixture per unit volume
E_v	Vibrational energy of mixture per unit volume
E_{vs}	Vibrational energy of species s per unit volume
$\overline{E}$	Reynolds averaged mean total energy of the mixture per unit volume
e	Internal energy per unit mass of mixture
e_{vs}	Vibrational energy per unit mass of species s
F, G	Flux vector components in x and y directions respectively

$\vec{F}$	Flux vector
f_{v1}, f_{v2}	Damping functions in SA turbulence model
f_w	Wall damping function in SA turbulence model
h_s	Enthalpy of species s per unit volume
h_s^0	Heat of formation of species s per kg
k	Turbulent kinetic energy
k_b	Backward reaction rate coefficient
k_f	Forward reaction rate coefficient
K_{eq}	Equilibrium constant
l	Arc length
Le	Lewis number
Le_T	Turbulent Lewis number
M	Molecular weight of mixture or Mach number
M	Collision partner in a chemical reaction
M_s	Molecular weight of species s
N	Atomic nitrogen
NO	Nitric oxide
N_2	Molecular nitrogen
ns	Number of species in the gas mixture
nd	Number of diatomic species in the gas mixture
O	Atomic oxygen
O_2	Molecular oxygen
p	Mixture pressure
$\overline{p}$	Reynolds averaged mean pressure
p'	Reynolds averaged fluctuating pressure
p_s	Partial pressure of species s
Pr	Prandtl number
Pr_T	Turbulent Prandtl number
q_j	Translational heat conduction in j direction
q_{vj}	Vibrational heat conduction in j direction
Q_{T-V}	Energy exchange rate for translation-vibration transitions
$Q_{v\ che}$	Vibrational source term due to chemical reactions

R	Mixture gas constant
R_i	Reaction rate for i^{th} reaction
R_s	Gas constant of species s
Re	Reynolds number
$\Re$	Universal gas constant
s_{ij}	Strain rate tensor
$\tilde{s}_{ij}$	Favre averaged mean strain rate tensor
T	Translational temperature of mixture
T_a	geometrically-averaged temperature
T_v	Vibrational temperature of mixture
$\tilde{T}$	Favre averaged mean translational temperature
T''	Favre averaged fluctuating translational temperature
$\mathbf{T}$	Time period
U	Conserved vector
u, v	Components of velocity vector in x and y directions respectively
$\overline{u}_i$	Reynolds averaged mean velocity
$\tilde{u}_i$	Favre averaged mean velocity
u_i'	Reynolds averaged fluctuating velocity
u_i''	Favre averaged fluctuating velocity
u_j	Mixture velocity in j direction
v_{sj}	Diffusion velocity of species s in j direction
V	Velocity vector or Volume of mixture
W	Source term vector
w_s	Chemical source term for species s
w_v	Source term for vibrational energy
x, y, z	Cartesian coordinates
Y_s	Mass fraction of species s

Greek Symbols

μ	Viscosity of mixture
μ_s	Viscosity of species s
μ_T	Turbulent viscosity or eddy viscosity
ν_T	Kinematic eddy viscosity

κ	Translational thermal conductivity of mixture
κ_v	Vibrational thermal conductivity of mixture
$\kappa_{tra\ s}$	Translational thermal conductivity of species s
$\kappa_{rot\ s}$	Rotational thermal conductivity of species s
$\kappa_{vib\ s}$	Vibrational thermal conductivity of species s
κ_T	Turbulent translational thermal conductivity of mixture
$\kappa_{v\ T}$	Turbulent vibrational thermal conductivity of mixture
θ_{vs}	Characteristic temperature of vibration for species s
ρ	Density of mixture
$\overline{\rho}$	Reynolds averaged mean density
ρ'	Reynolds averaged fluctuating density
ρ_s	Density of species s
γ	Ratio of specific heats
$\tau_{s\ L-T}$	Molar averaged Landu-Teller relaxation time
$\tau_{sr\ L-T}$	Landu-Teller inter-species relaxation time
τ_{ij}	Viscous stress tensor
$\overline{\tau}_{ij}$	Mean viscous stress tensor
τ_{ij}^T	Reynolds or turbulent stress tensor
δ	Boundary layer thickness
τ_f	Characteristic flow time
η	Coefficient in the calculation of a chemical reaction rate
θ_d	Characteristic temperature for a chemical reaction

Subscript

b	Backward
f	Forward
i, j, k	x, y and z components of vector
s	Species
v	Vibrational
∞	Freestream
I	Inviscid
V	Viscous

Superscript

$'$	Reynolds fluctuating variable
$''$	Favre fluctuating variable

Abbreviations

AOA	Angle of attack
CFD	Computational fluid dynamics
CFL	Courant Friedrichs Lewy
LHS	Left hand side
FIRE	Flight investigation of re-entry experiment
NASA	National aeronautics and space administration
NS	Navier-Stokes
RANS	Reynolds averaged Navier Stokes
RHS	Right hand side
SA	Spalart-Allmaras
V-R	Vibrational-Rotational
V-T	Vibrational-Translational
V-V	Vibrational-Vibrational
rsf	Reaction scaling factor

Chapter 1

Introduction

The quest to explore outer space and the need to have faster traveling vehicles for military and space transport has led to the development of hypersonic vehicles, which travel at a speed greater than five times the speed of sound. While cruising at hypersonic speeds, the vehicles are enveloped by a strong bow shock. The large kinetic energy of the flow, relative to the vehicle, is converted into internal energy across the shock wave. The gas in the region between the shock wave and the vehicle surface, referred to as the shock layer, is therefore extremely hot. The gas temperatures are often high enough to initiate dissociation of the gas molecules. A thick boundary layer forms on the vehicle surface, and viscous dissipation in the boundary layer can elevate the gas temperatures further. Thus, hypersonic vehicles are exposed to severe aero-thermodynamic environment.

For the past three decades there have been intensive research and developmental efforts to understand hypersonic flows. This has resulted in the development of sophisticated high-enthalpy wind tunnels, shock tunnels, and Computational Fluid Dynamics (CFD) methods. Wind and shock tunnel tests are difficult and are costly to conduct at high enthalpy conditions. CFD is a much more economical approach for studying such flows. Therefore CFD is extensively used as an analysis tool in the design of hypersonic vehicles [1]. CFD is also used as a research tool to understand the complicated hypersonic effects [2].

In this chapter, a brief description of the hypersonic flowfield over a re-entry capsule is presented. Physical processes associated with re-entry flows are explained. It is followed by literature review on CFD predictions of re-entry flows describing their potential and limitations. Motivation and objectives of the thesis are presented next. Finally, the scope of the work and a chapter-wise organization of the thesis are described.

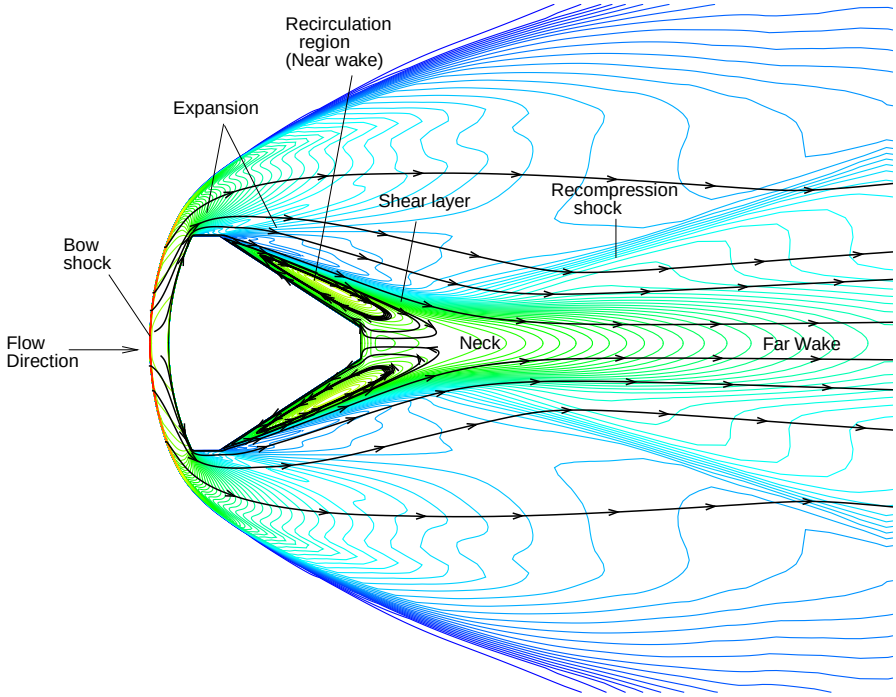

Figure 1.1: Flow around a typical re-entry capsule: streamlines are superimposed on temperature contours to highlight the main features of the flowfield.

1.1 Background

Re-entry capsules are used for space exploration applications due to their ability to withstand high heating loads during the re-entry phase [3]. A re-entry capsule or planetary probe consists of a blunt forebody, followed by a conical afterbody with straight or rounded base. A generic re-entry flowfield over a capsule is shown in Fig. 1.1 in terms of the temperature contours. Streamlines are superimposed to show the flow direction and recirculation bubble. Prominent features such as bow shock, flow expansion at the corners, shear layer and recirculation bubble are identified. Detached bow shock ahead of the forebody decelerates the flow to a subsonic Mach number and causes sudden rise of temperature at the shock. High temperature effects and thermo-chemical non-equilibrium determine the gas properties in the shock layer. Flow expansion around the shoulder accelerates the gas to supersonic Mach numbers.

The boundary layer separates on the afterbody and forms a low-speed recirculation region which is referred to as the near-wake. The recirculation bubble often consists of a single toroidal vortex. A free shear layer originates from the separation point and separates the inner recirculation region from the outer inviscid expansion region. The flow is turned to freestream direction

by a recompression shock at the neck. Re-compression shock again increases the temperature of the gas. Hence, the neck is characterized by maximum temperatures in the afterbody region. Flowfield after the neck region is referred to as the far-wake.

Hypersonic flows are characterized by high temperatures in the shock layer. These high temperatures, excite the internal energy modes and chemical reactions. Depending on the shock layer temperature, internal energy excitation can consist of rotational and vibrational relaxation and ionization. Usually internal energy excitation and chemical reactions are referred to as thermo-chemistry. This phenomenon is associated with energy exchange mechanisms such as a transfer- of translational energy to internal energy modes and to chemical enthalpy. Under these conditions, a fluid deviates from the perfect gas behavior. Therefore appropriate physico-chemical models should be used to account for the energy exchange mechanisms. The effect of thermo-chemistry is to lower post-shock temperature and reduce shock stand-off distance compared to that of a perfect gas simulation. Hence reacting gas simulations will predict less thermal load to the vehicle. Although pressure is not influenced significantly by the chemical reactions, the pitching moment coefficient increases appreciably due to the reactions [3]. If temperatures are high enough, air ionizes and results in communication block out of the vehicle with the ground.

Thermo-chemical processes require a finite number of molecular/atomic collisions to reach equilibrium. At flight conditions, the density is usually too low to induce sufficient collisions to reach equilibrium while the gas passes through the shock layer. The chemical time scales are often comparable to the fluidynamic times scales, leading to significant non-equilibrium effects in the flowfield. Therefore appropriate non-equilibrium models should be used to compute the aero-thermal loads.

As the Mach number increases, the shock comes closer to the vehicle body and can interact with the boundary layer. High temperature prevails in the hypersonic boundary layer due to viscous dissipation, which transfers the kinetic energy of the fluid to thermal energy. Hence, viscous effects should be properly modeled to accurately predict aerodynamic and thermal coefficients. Shock waves generated from the wing or control surfaces can interact with the bow shock of the vehicle. Such interactions can lead to complex flowfields and highly localized heating rates. For example, severe damage to the vehicle is practically observed in the flight test of X-15 [3]. Similarly impingement of shear layer on the afterbody portion of a capsule can result in highly localized surface loads [4]. The presence of viscous interaction, shock-shock

interaction and high temperature effects result in complex flow physics. Predicting re-entry flowfields using numerical simulation is, therefore, a challenging task.

Thermal Protection System (TPS) is used to protect a vehicle or capsule from the surrounding hot gas. Material selection and thickness of the TPS are important elements in the design of a re-entry vehicle. TPS is usually designed based on aerothermal predictions such as heat flux, surface pressure and total integrated heat load. CFD simulations are extensively used to predict the above properties. Therefore the numerical predictions need to be thoroughly validated for different phenomena occurring at re-entry conditions. A brief review of literature on the re-entry flow predictions is given below.

1.2 Review of Literature

There had been a thrust to improve the predictive capability for re-entry flows since the Apollo era. In the early 1960s, Fay and Riddell correlation [5] was developed to calculate the stagnation point heating rate, which is required for sizing the TPS of a vehicle. Different levels of approximation to the Navier-Stokes equations, such as, viscous shock layer, thin layer approximation and parabolized Navier-Stokes equations were developed overs the years. Similarly, approximate methods were developed to model the thermo-chemical phenomena with the equilibrium assumption. However, these approximations do not provide accurate information about the flowfields over re-entry vehicles [3]. This is due to the strong inviscid-viscous interactions, high-temperature and non-equilibrium effects, which are associated with high Mach number flows. This necessitated coupled solutions to the Navier-Stokes equations and the equations governing the thermo-chemical non-equilibrium. In the late 1980s, many researches, including Pratt [6], Candler [7], Josyula [8], Park [9], Tirskiy [10], and Grasso [11] obtained solutions to the complete set of Navier-Stokes and thermo-chemical equations. In these methods, the thermo-chemical and Navier-Stokes equations are strongly coupled to account for non-equilibrium effects.

CFD predictions need to be validated against experimental or flight measurements to assess the assumptions made in the physical modeling and numerical method. Shock stand-off distance, surface pressure and heating rate are frequently used to validate the thermo-chemical models used in the CFD formulation. Olejniczak and Candler [12] computed the vibrationally excited N_2 flow over a blunt body with different vibrational non-equilibrium models. The

predicted shock stand-off distance and shape were compared with the experimental measurements. They find that shock stand-off distance is relatively insensitive to the vibrational non-equilibrium models, where-as the shape of the shock wave at the shoulder region is sensitive to the thermal relaxation rates. Josyula and Shang [13] studied the effect of vibrational relaxation in re-entry flows for Mach numbers ranging from 10 to 18. They find that heating rate computed with the vibrational non-equilibrium model is nearly 10 to 20% higher than that obtained with the vibrational equilibrium assumption.

Candler [7] presented the computation of hypersonic reacting flowfields over spheres and cones considering thermo-chemical non-equilibrium effects. The predicted shock detachment distance is found to be in good agreement with the experimental measurements. Tchuen and Zeitoun [14] studied the effect of chemical reactions for a range of- freestream Mach numbers, densities, and stagnation enthalpies. They employed different rate constants for chemical reactions available in the literature to simulate the high-enthalpy test cases. The shock stand-off distance, peak translational temperature and species mass fraction in the shock layer are found to be sensitive to the reaction rates used in the simulations. The stagnation point heat flux computed using various reaction rates differs by up to 60%.

High-enthalpy flow over double-cone involves complex flow features such as shock-shock and shock-boundary layer interactions, flow separation and chemical reactions in the separation region. The inviscid shock structure, the size of the separation bubble, and the associated surface properties are highly sensitive to numerical method and thermo-chemical rate constants used in the CFD. Nompelis $et\ al.$ [2, 15, 16] studied this flowfield extensively to investigate the different aspects of CFD of hypersonic flows. They reported large number of experiments with stagnation enthalpy ranging from 3 MJ/kg to 15 MJ/kg. The test gases considered in these experiments were pure oxygen, nitrogen and air. The flowfields were computed at test conditions and the predicted shock pattern, surface pressure and heating rates were compared with experimental measurements. They find that at low enthalpies ($<$5 MJ/kg), where chemical reactions do not occur, the heating rate predictions compared well with the experimental measurements. However, at higher enthalpies ($>$5 MJ/kg), when there is significant chemistry in the flowfield, the agreement between the predictions and experiments is found to be poor.

The heating rates on the afterbody are lower compared to those of the forebody. However, predicting the surface heating and pressure loads is a difficult task due to the presence large separated regions on the afterbody. The flow separation and the resulting re-circulation bubble

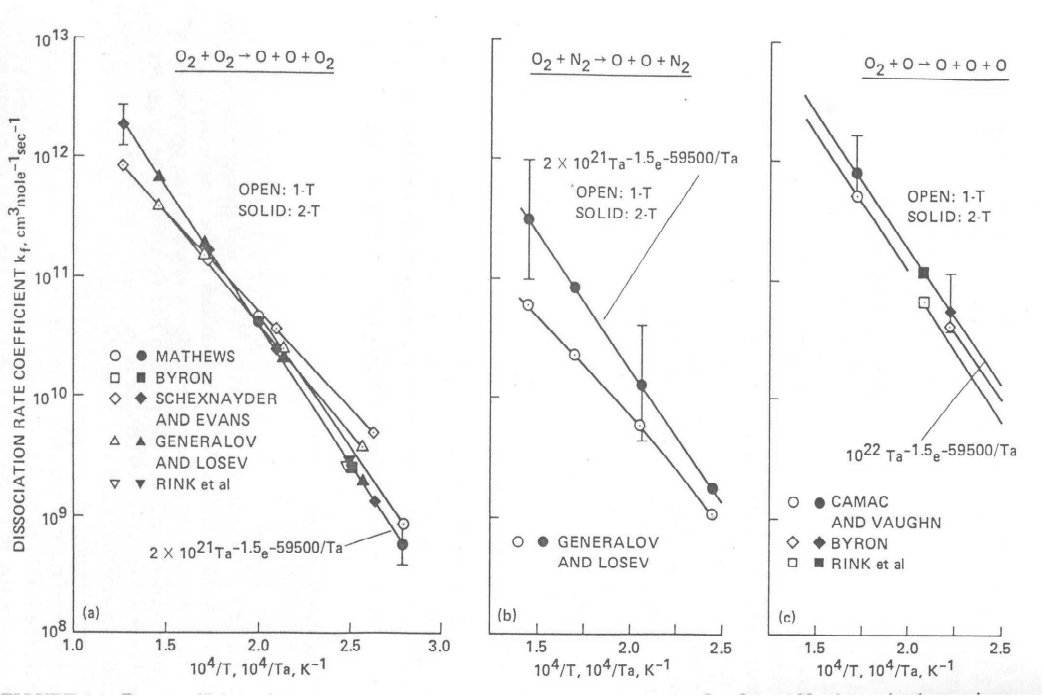

Figure 1.2: Uncertainty in the measurement of O_2 dissociation rate constant. The collision partners are O_2, N_2 and O. The figure is reproduced from Ref. 9.

have a significant effect on the static and dynamic stability of the entry capsules [4]. This has necessitated characterization of the afterbody flowfields for the design of space capsules; hence, many studies have been performed in this direction. Schneider [4] reviewed experimental studies performed on the afterbody flows in the Apollo and Gemini era.

Dogra *et al.* [17] investigated the effect of chemical reactions on the near-wake flowfield over 70° blunt cone numerically. The reacting gas computations yielded a 25% larger separation bubble compared to that obtained with the perfect gas model. Hollis [18] conducted experiments to investigate the wake flowfield over MP-1 configuration, which corresponds to the scaled model of the Mars Pathfinder space capsule. Numerical predictions compared well with the measured heating rates on the forebody. However, significant differences were noticed near the re-attachment point on the afterbody. Grasso *et al.* [19] analyzed the hypersonic near-wake flows over sharp-nosed and blunt-nosed bodies using CFD. The computed temperature profile along the wake axis compared well with that obtained from measurements. The effect of nose bluntness, Mach number, and Reynolds number on the near-wake flowfield was investigated. They found that near-wake flow properties depend on the local Reynolds number along the re-circulation dividing streamline.

The physical models of the thermo-chemical phenomena used in a CFD simulation are developed based on experimentally determined thermal relaxation rates and chemical reaction rate constants. These parameters are commonly referred to as kinetic data. High-enthalpy impulse facilities i.e. shock tunnels are used to measure these rate constants. Hence, there is always certain amount of uncertainty in the measurement of these rate constants. Figure 1.2, which is reproduced from Ref. 9 shows the uncertainty in the determination of dissociation rate constant for molecular oxygen. The rate coefficient for the reaction O_2+O_2→O+O+O_2 is measured at $10^4/T_a \approx 1.25$ and 2.75 and the corresponding uncertainty in the measurement is also marked. It is observed that the uncertainty in the measurement of rate coefficient is an order of one magnitude. Similarly, the uncertainty in the rate constant for the reaction O_2+N_2→O+O+N_2 is shown for $10^4/T_a \approx 1.5$ and 2.1. The uncertainty in these rate parameters leads to variation in the computed surface heat flux. Thus, the accuracy of the computational predictions of re-entry flowfields and the associated aero-thermal loads depend on accurate modeling of these high-temperature phenomena. For reliable and safe design of entry vehicles, the uncertainty margins on the predicted heating rate need to be estimated.

In the early 2000s, the Monte Carlo sensitivity and uncertainty analysis was developed to determine the uncertainty in the predicted heating rates. Bose and Wright [20] used these analyses to study the effect of thermo-chemical modeling parameters on the stagnation point heat transfer rate. The freestream conditions correspond to the peak heating condition of the Mars pathfinder vehicle. They varied several parameters, including reaction rate constants, diffusion coefficients and surface catalysis parameters, and performed a large number of simulations to quantify the effect of these parameters on the heating rate. They studied different flow regimes based on the wall catalytic behavior and identified the dominant parameters affecting the heating rate. For super-catalytic surfaces, the stagnation point heat transfer rate is primarily sensitive to the diffusion parameter, whereas the oxygen atom recombination rate is found to be the dominant parameter in the weakly catalytic regime. A similar uncertainty analysis was performed by Palmer [21] for Crew Exploration Vehicle at conditions representative of low earth orbit and lunar return entries. The study included radiative effects, in addition to convective heating, and it was found that changes in radiative heating are less than those in convective heating due to variation in key input parameters.

1.3 Motivation and Objectives

The chemical reactions occurring in a high-temperature gas mixture have a dominant effect on re-entry flow features and associated surface properties. Heat released or absorbed during chemical reactions affects the temperature of the gas, which in turn affects the surface heat flux. The chemical reactions also alter the gas composition and the associated properties such as conductivity and viscosity of the gas mixture. Changes in conductivity of the fluid medium have additional effects on the heat transfer rates. Variations in fluid viscosity affect the local Reynolds number. This can alter the boundary layer and the flow separation characteristics. Changes in the separation and reattachment locations alter the associated shock structure, affecting surface pressure and heat flux distribution significantly. Thus, chemical reactions affect re-entry flows in multiple ways and a detailed understanding of the chemistry and its effects on flowfield predictions is important.

The gas phase chemistry at re-entry conditions usually consists of multiple dissociation/recombination and exchange reactions. The rates of these reactions depend on the temperature and pressure of the gas mixture, and therefore varies from point to point in a re-entry flowfield. The reaction rates are also functions of the molar concentration of different species in the gas mixture. The gas dynamic and diffusion processes in the flow determine the local gas properties. They play a major role in determining the chemical activity in a region. The chemical reactions, on the other hand, alter the local gas properties, and thus can have a significant effect on the gas dynamics and heat transfer. Thus, there is a two-way interaction between the flow processes and the chemical reactions occurring in a re-entry flow.

The effect of chemical reactions on the flowfield predictions also depends on the degree of chemical non-equilibrium. This, in turn, is a function of the local gas density, which varies over a large range in the flow around a re-entry capsule. The gas density increases by an order in magnitude across the shock wave and further increases in the vicinity of an isothermal cold wall. On the other hand, flow expansion around the shoulder results in very low density on the afterbody. Therefore the local chemical state of the gas is a function of not only the nature of a chemical reaction, but also the extent of chemical non-equilibrium at a given thermodynamic condition of the gas. Studying the effects of multiple parameters, like temperature, density and gas composition, that vary from point to point in a re-entry flow is necessary for understanding the effect of chemical reactions on the flow prediction.

The thesis presents a study of the chemical reactions occurring in a re-entry flowfield around a capsule geometry. Controlled numerical experiments are performed by varying the chemical reaction rates and studying the flowfield solutions in detail. The focus is on understanding the physical mechanisms through which the chemistry and the gas dynamics influence each other. The analysis is performed at flight conditions corresponding to different points along a re-entry trajectory. The specific objectives of the thesis are as follows:

1. Analyze the chemical reactions occurring in a high-enthalpy flowfield and study their effect on the aero-thermodynamics of a re-entry capsule.

2. Investigate the sensitivity of heat flux to the variations in the chemical rate constants.

3. Identify the underlying processes and the critical factors that influence the heat flux sensitivity to the variation in reaction rates.

4. Study the chemical reactions and their effect on the flowfield predictions at different points along a re-entry trajectory.

1.4 Scope of Thesis

The thesis describes the effect of variation in chemical reaction rates on heating rate predictions at three re-entry conditions. The freestream parameters are chosen such that they represent low, medium and high altitude conditions in an earth entry trajectory. The three test cases vary significantly in terms of freestream density, velocity and Mach number. The freestream temperature is found to vary by a small amount among the three test cases. Identical wall temperature is used in each simulation at the three conditions. The geometry corresponds to FIRE II re-entry capsule at zero angle of attack for all the simulations.

Numerical simulations are performed using an in-house parallel CFD code, which accounts for finite rate thermo-chemistry occurring in high-temperature air. The code is based on the implicit DPLR [22] algorithm and has been applied to several hypersonic configurations. The flowfield over FIRE II re-entry capsule at 35 km condition is chosen for validating the CFD code predictions. A careful grid-convergence study is performed to assess the grid-independence of computed surface properties. Nose stagnation and afterbody heating rates are compared with in-flight measurements. The details are presented in Chapter 3.

The solutions computed at a chosen freestream condition are analyzed in detail in terms of the variation in gas temperature, density and composition over the entire flowfield. The manner in which these gas properties determine the local chemistry and the degree of non-equilibrium is studied. The rates of different chemical reactions and the resulting species source terms are compared to identify the dominant chemical reactions and reaction mechanisms occurring in the flow. Next, controlled numerical experiments are performed by varying the reaction rates and studying their effect on the flow processes. The flow solutions computed by altering the reaction rates are carefully analyzed to understand the physical effects that influence the surface heat transfer rate. By comparing the altered reactivity solutions with the baseline solution, rate limiting steps in the reaction mechanisms are identified.

A zonal analysis is performed to understand the effects of shock-layer chemistry and boundary-layer chemical reactions on the heating rate predictions. The factors contributing to the heat flux variations are studied in detail, and the analysis is carried out at different points on the vehicle surface. The zonal analysis gives insight into the interaction between the chemical reactions and gas dynamics. In particular, the effect of flow separation on the afterbody and flow expansion around the shoulder on the aerothermal predictions is presented. The above mentioned study at the three trajectory points is presented in Chapter 4, 5, and 6, respectively.

As the altitude of the flight decreases the density of the gas increases and stagnation enthalpy of the flow decreases. The above three trajectory points are chosen such that the effect of variation in altitude $i.e.$ changes in freestream density and stagnation enthalpy on the heating rate sensitivity can be investigated. The heat flux variations at the nose stagnation point for the three altitudes is critically analyzed and presented in Chapter 7. The rate constants of dominant chemical reactions for which heat flux is sensitive at the three trajectory points are also identified.

Chapter 2

Simulation Methodology

The details of simulation methodology used in the thesis work are presented in this chapter. First governing equations for non-equilibrium viscous laminar flows are explained. RANS and turbulence model equations for reacting flows are given next. Finally description of the finite volume method is presented.

Navier-Stokes equations represent the conservation of mass, momentum and energy in the presence of dissipative effects. Thus, NS equations are obvious choice for computing the compressible laminar flows. However for computing the re-entry flows, high temperature effects should be considered. For example, if the temperature of the air exceeds 800 K, vibrational modes excite, above 2000 K dissociation of the oxygen molecules occurs and above 4000 K dissociation of Nitrogen molecules begins. For such high temperature flows, perfect gas equation of state is not valid. Hence additional thermo-chemical equations which account for the above mentioned high-temperature phenomena need to be considered.

Vibrational excitation and chemical reactions are collision induced phenomena. Hence they require finite time to approach corresponding equilibrium states. At low densities and high velocities, typical of re-entry conditions, the time scale at which vibrational excitation and chemical reactions occur is, of the same order of fluidynamic time scales. In such conditions, gas does not approach equilibrium state corresponding to local thermodynamic condition. Thus, gas is in a thermo-chemical non-equilibrium state. Hence a coupled solution of NS equations and thermo-chemical equations is required to simulate the non-equilibrium flows.

2.1 Non-equilibrium Viscous Laminar Flows

In the present work we assume that rotational modes of the gas are in equilibrium with the translational modes where as the vibrational modes are in non-equilibrium. Further we assume that the vibration-vibration transitions are fast enough to equilibriate with each other so that a single vibrational temperature is sufficient to describe the vibrational state of the gas. The translational temperature defines the translational-rotational state of the gas. At the range of temperatures considered in the present work (below 10000 K), ionization will not occur. Hence air is treated as a neutral mixture of molecular nitrogen (N_2), molecular oxygen (O_2), nitric oxide (NO), atomic nitrogen (N) and atomic oxygen (O). Each of these species is individually treated as a perfect gas. Thermo-chemical equations described here are species continuity equations and conservation equation for mixture vibrational energy.

With these assumptions, we present the governing equations for high-temperature viscous flows in conservation form using tensor notation . For a mixture of ns species, the species continuity equation is given by

$$\frac{\partial \rho_s}{\partial t} + \frac{\partial}{\partial x_j}(\rho_s u_j) + \frac{\partial}{\partial x_j}(\rho_s v_{sj}) = w_s \tag{2.1}$$

where ρ_s is the density of the species s, u_j is the mixture velocity in the j direction, v_{sj} is the diffusion velocity, due to mass diffusion. The source term w_s represents, construction and destruction of species due to non-equilibrium chemical reactions. The expressions for source term are presented in Section 2.1.4.

The mixture momentum equation is same as that of the perfect gas flows and is given below.

$$\frac{\partial}{\partial t}(\rho u_i) + \frac{\partial}{\partial x_j}(\rho u_i u_j + p\delta_{ij}) + \frac{\partial}{\partial x_j}(\tau_{ij}) = 0 \tag{2.2}$$

where p is the mixture pressure, δ_{ij} is kr$\ddot{o}$necker delta and τ_{ij} is viscous stress tensor. Using Stokes hypothesis for a Newtonian fluid, τ_{ij} is given by

$$\tau_{ij} = -\mu 2 s_{ij} + \frac{2}{3}\mu \frac{\partial u_k}{\partial x_k}\delta_{ij} \tag{2.3}$$

Where μ is mixture viscosity and s_{ij} is strain rate tensor and is given by

$$s_{ij} = \frac{1}{2}\left(\frac{\partial u_i}{\partial x_j} + \frac{\partial u_j}{\partial x_i}\right) \tag{2.4}$$

The procedure for the calculation of mixture viscosity is presented in Section 2.1.2.

The conservation equation for mixture total energy is given by

$$\frac{\partial E}{\partial t} + \frac{\partial}{\partial x_j}((E+p)u_j) + \frac{\partial}{\partial x_j}(q_j + q_{vj}) + \frac{\partial}{\partial x_j}(\tau_{ij}u_i) + \sum_{s=1}^{ns}\frac{\partial}{\partial x_j}(h_s v_{sj}) = 0 \tag{2.5}$$

where h_s is the species enthalpy per unit volume, q_j and q_{vj} are translational and vibrational heat conduction. Both heat conduction terms are evaluated by using the Fourier's law of heat conduction

$$q_j = -\kappa\frac{\partial T}{\partial x_j}, \qquad\qquad q_{vj} = -\kappa_v\frac{\partial T_v}{\partial x_j} \tag{2.6}$$

where κ and κ_v are mixture thermal conductivities as defined in the Section 2.1.2.

The conservation equation for mixture vibrational energy is given by

$$\frac{\partial E_v}{\partial t} + \frac{\partial}{\partial x_j}(E_v u_j) + \frac{\partial}{\partial x_j}(q_{vj}) + \sum_{s=1}^{nd}\frac{\partial}{\partial x_j}(\rho_s e_{vs} v_{sj}) = w_v \tag{2.7}$$

where E_v is mixture vibrational energy per unit volume, e_{vs} is the vibrational energy per unit mass of the species s and w_v is the source term for vibrational energy, which is explained in Section 2.1.5. The derivation of the vibrational energy equation from kinetic theory of the gas, is given by Olejniczak $et\ al.$ in Ref. 12.

2.1.1 Equation of State

We require equations relating T, T_v and p to conserved variables. These equations are described below. The total energy of the gas per unit volume can be defined as

$$E = \sum_{s=1}^{ns}\rho_s c_{vs} T + \frac{1}{2}\rho u_i u_i + E_v + \sum_{s=1}^{ns}\rho_s h_s^0 \tag{2.8}$$

where c_{vs} is the translational-rotational specific heat of species s, given by

$$c_{vs} = c_{v\ tra\ s} + c_{v\ rot\ s} \tag{2.9}$$

where $c_{v\ tra\ s}$ and $c_{v\ rot\ s}$ are the translational and rotational specific heats given by

$$c_{v\ tra\ s} = \frac{3}{2}\frac{\Re}{M_s}, \qquad\qquad c_{v\ rot\ s} = \frac{\Re}{M_s}, \qquad s \leq nd \tag{2.10}$$

$\Re$ and M_s are the universal gas constant (=8.314 kJ/kg-mol-K) and species molecular weight respectively and nd is number of diatomic species in the mixture. Thus the first term in the Eq. 2.8 represents the energy due to the translational and rotational modes of the molecules. The second term represents the kinetic energy of the gas mixture and third term represents energy

Table 2.1: Characteristic harmonic oscillator vibrational temperatures (K)

Species	θ_{vs}
N_2	3395
O_2	2239
NO	2817

Table 2.2: Heats of formation (J/kg)

Species	h_s^0
N_2	0
O_2	0
NO	2.996123×10^6
N	3.362161×10^7
O	1.543119×10^7

due to vibrational modes of the gas . If we assume that the molecules of the gas are in Boltzmann distribution [3], then the vibrational energy per unit volume of the species (E_{vs}), is given by

$$E_{vs} = \rho_s \frac{\Re}{M_s} \frac{\theta_{vs}}{exp(\theta_{vs}/T_v) - 1} \tag{2.11}$$

Where θ_{vs} is the characteristic temperature of the vibration for species s and are presented for five species air in Table 2.1. Now the mixture vibrational energy is obtained by summing vibrational energy of the diatomic species

$$E_v = \sum_{s=1}^{nd} E_{vs} \tag{2.12}$$

For a gas mixture with two or more diatomic species ($nd \geq 2$), T_v cannot be calculated directly from E_v and an iterative procedure is required. The last term in the in Eq. 2.8 represents the heat of formation of each species. h_s^0 is known as the heat of formation. The values of the h_s^0 for each species are presented in the Table 2.2.

The mixture pressure can be obtained by using the Dalton's law. Hence sum of the partial pressures of the individual species will give mixture pressure. Partial pressure of the species can be determined from the perfect gas law.

Table 2.3: Viscosity coefficients for Blottner model

Species	A_s	B_s	C_s
N_2	0.0268142	0.3177838	-11.3155513
O_2	0.0449290	-0.0826158	-9.2019475
NO	0.0436378	-0.0335511	-9.5767430
N	0.0115572	-0.6031679	-12.4327495
O	0.0203144	0.4294404	-11.6031403

$$p = \sum_{s=1}^{ns} p_s, \qquad p_s = \rho_s \frac{\Re}{M_s} T \tag{2.13}$$

2.1.2 Species and Mixture Transport Properties

In this section, procedure for calculating the mixture viscosity, thermal conductivity and species diffusion coefficients is presented. The viscosity of the each species is determined using curve fit data of Blottner $et\ al.$ [23], which is given below

$$\mu_s = 0.1\ exp[(A_s ln\ T + B_s) ln\ T + C_s] \tag{2.14}$$

where A_s, B_s and C_s are curve fit constants. The values of these constants for each species are listed in the Table 2.3. This curve fit data is valid up to the $10000\ K$, which is much higher than the temperatures encountered in the present work. Viscosity coefficient of the species, which are not mentioned in the Blottner $et\ al.$ curve fit data, or beyond $10000\ K$ can be computed from kinetic theory using cross section data [24], [25].

The thermal conductivities for the translational and rotational energy modes are determined using the Eucken relation [26], which correlates thermal conductivity for individual energy mode to corresponding specific heat and viscosity of the species. Thus we have

$$\kappa_{tra\ s} = \frac{5}{2} \mu_s c_{v\ tra\ s}, \qquad \kappa_{rot\ s} = \mu_s c_{v\ rot\ s} \tag{2.15}$$

Now the mixture viscosity and thermal conductivity are computed using the Wilke's mixing rule [27]

$$\mu = \sum_s \frac{X_s \mu_s}{\phi_s} \qquad \kappa = \sum_s \frac{X_s \kappa_s}{\phi_s} \tag{2.16}$$

where

$$X_s = \frac{c_s M}{M_s}, \qquad M = (\sum_s \frac{c_s}{M_s})^{-1}, \tag{2.17}$$

$$\phi_s = \sum_r X_r \left[1 + \sqrt{\frac{\mu_s}{\mu_r}} \left(\frac{M_r}{M_s}\right)^{1/4}\right]^2 \left[\sqrt{8\left(1 + \frac{M_s}{M_r}\right)}\right]^{-1} \tag{2.18}$$

Mixture vibrational thermal conductivity is given by

$$\kappa_v = 1.2\mu \sum_{s=1}^{nv} \frac{\rho_s}{\rho} \tag{2.19}$$

Where the summation is over all the vibrational modes.

2.1.3 Species Diffusion Coefficients

In the present work, mass diffusion due to concentration gradient is considered. The diffusion due to pressure and temperature gradients are neglected as their contribution to total mass diffusion is relatively small. Using Fick's law, the diffusion term in the species continuity equation (Eq. 2.1) can be written as

$$\rho_s v_{sj} = -\rho D_s \frac{\partial c_s}{\partial x_j} \tag{2.20}$$

where D_s is the diffusion coefficient of species s. In the present work we assume that, diffusion coefficient is same for all the species. The value of D is obtained by assuming a constant Lewis number, Le, defined by

$$Le = D\frac{\rho c_p}{\kappa} \tag{2.21}$$

where c_p is constant pressure translational-rotational specific heat. For air, the Lewis number assumed to be 1.4. Multi component diffusion coefficient D_s can be obtained from curve fit data of Blottner $et\ al.$ [23]. However it was shown for air flows that the multi component diffusion data has little effect on the computed flowfield [28].

2.1.4 Chemical Source Terms

Species continuity equation has a source term, due to production and destruction of species, caused by the non-equilibrium chemical reactions. The specific expressions for the each species source term are presented in the present section.

In high temperature non-ionized air, the following five reactions are important.

$$
\begin{aligned}
\mathrm{N_2 + M} &\rightleftharpoons \mathrm{2N + M} \\
\mathrm{O_2 + M} &\rightleftharpoons \mathrm{2O + M} \\
\mathrm{NO + M} &\rightleftharpoons \mathrm{N + O + M} \\
\mathrm{N_2 + \ O} &\rightleftharpoons \mathrm{NO + N} \\
\mathrm{NO + O} &\rightleftharpoons \mathrm{O_2 + N}
\end{aligned}
\tag{2.22}
$$

In the above reactions, the bidirectional arrows indicates that the reaction can proceed in both directions. In the present work, a forward direction indicates, the direction in which reaction is endothermic. The first three reactions represent the dissociation of N_2, O_2 and NO molecules respectively. In the dissociation reactions, M is collision partner, which provides the required energy, to break the chemical bond. The collision partner can be any of the five species, and it is unaltered in the reaction. The reverse of the dissociation reactions is a recombination reaction, in which, the atomic species releases chemical energy and the collision partner is energy absorber. The last two reactions are the Zeldovich exchange reactions. These Zeldovich reactions govern the concentration of NO in hypersonic flows.

Now the forward and backward reaction rates for the above five reactions are given by

$$
\begin{aligned}
R_1 &= \textstyle\sum_{m=1}^{5} \left[k_{b_{1m}} \frac{\rho_{\mathrm{N}}}{M_{\mathrm{N}}} \frac{\rho_{\mathrm{N}}}{M_{\mathrm{N}}} \frac{\rho_m}{M_m} - k_{f_{1m}} \frac{\rho_{\mathrm{N_2}}}{M_{\mathrm{N_2}}} \frac{\rho_m}{M_m} \right] \\
R_2 &= \textstyle\sum_{m=1}^{5} \left[k_{b_{2m}} \frac{\rho_{\mathrm{O}}}{M_{\mathrm{O}}} \frac{\rho_{\mathrm{O}}}{M_{\mathrm{O}}} \frac{\rho_m}{M_m} - k_{f_{2m}} \frac{\rho_{\mathrm{O_2}}}{M_{\mathrm{O_2}}} \frac{\rho_m}{M_m} \right] \\
R_3 &= \textstyle\sum_{m=1}^{5} \left[k_{b_{3m}} \frac{\rho_{\mathrm{N}}}{M_{\mathrm{N}}} \frac{\rho_{\mathrm{O}}}{M_{\mathrm{O}}} \frac{\rho_m}{M_m} - k_{f_{3m}} \frac{\rho_{\mathrm{NO}}}{M_{\mathrm{NO}}} \frac{\rho_m}{M_m} \right] \\
R_4 &= k_{b_4} \frac{\rho_{\mathrm{NO}}}{M_{\mathrm{NO}}} \frac{\rho_{\mathrm{N}}}{M_{\mathrm{N}}} - k_{f_4} \frac{\rho_{\mathrm{N_2}}}{M_{\mathrm{N_2}}} \frac{\rho_{\mathrm{O}}}{M_{\mathrm{O}}} \\
R_5 &= k_{b_5} \frac{\rho_{\mathrm{O_2}}}{M_{\mathrm{O_2}}} \frac{\rho_{\mathrm{N}}}{M_{\mathrm{N}}} - k_{f_5} \frac{\rho_{\mathrm{NO}}}{M_{\mathrm{NO}}} \frac{\rho_{\mathrm{O}}}{M_{\mathrm{O}}}
\end{aligned}
\tag{2.23}
$$

In the above equations k_f and k_b are forward and backward reaction rate constants. Suffix m

indicates collision partner. ρ_i and M_i represent the i^{th} species density and molecular weight respectively. The species source term can be represented in terms of the reaction rates as shown below.

$$\begin{aligned} w_{\mathrm{N}_2} &= M_{\mathrm{N}_2}\left(R_1 + R_4\right) \\ w_{\mathrm{O}_2} &= M_{\mathrm{O}_2}\left(R_2 - R_5\right) \\ w_{\mathrm{NO}} &= M_{\mathrm{NO}}\left(R_3 - R_4 + R_5\right) \\ w_{\mathrm{N}} &= M_{\mathrm{N}}\left(-2R_1 - R_3 - R_4 - R_5\right) \\ w_{\mathrm{O}} &= M_{\mathrm{O}}\left(-2R_2 - R_3 + R_4 + R_5\right) \end{aligned} \tag{2.24}$$

Note that sum of the source terms for elemental species is identically zero, as required by the global conservation of mass in the system.

Now we require expressions for forward and backward reaction rate constants, to close the chemical source terms. These reaction rates should consider the chemical non-equilibrium effects. The important mechanism that needs to be considered in defining the non-equilibrium reactions rates is physical coupling between the vibration relaxation process and dissociation and recombination reactions. The effect of this coupling is to reduce the dissociation reaction rate for non-equilibrium state, until equilibrium is reached. Many models are proposed to account for this vibration-dissociation coupling effect such as coupled vibration-dissociation-vibration model [29], Macheret-Rich model [30] and Park model [31].

Of all the models, most extensively used one is Park model. This model is relatively easy to implement in CFD codes. Also for many hypersonic re-entry flows, Park model is shown to give satisfactory results [9]. In the present work we have employed Park model. In this model reaction rates are evaluated at an effective temperature, T_a, which is a function of translational and vibrational temperature. The forward reaction rates are expressed using a modified Arrhenius form, as given below.

$$k_{fm}(T_a) = C_{fm} T_a^{\eta_m} exp\left(-\theta_{dm}/T_a\right) \tag{2.25}$$

where $C_{fm},\ \eta_m$ and θ_{dm} are experimentally determined curve fit data over a given temperature range [9]. m is a index notation for reactions. The backward reaction rate is obtained using the

principle of detailed balance

$$k_{bm}(T_a) = \frac{k_{bm}(T_a)}{K_{eq\ m}} \tag{2.26}$$

where K_{eq} is equilibrium constant. K_{eq} is function of temperature only, and expression is given by

$$K_{eq\ m} = C_m exp\left(A_{1m} + A_{2m}Z + A_{3m}Z^2 + A_{4m}Z^3 + A_{5m}Z^4\right) \tag{2.27}$$

where $Z = 10,000/T$. The constants C_m, A_{nm} are curve fit to the experimental data [9].

Now the effective temperature for dissociation is taken as the geometric average of the translational-rotational and vibrational temperature.

$$T_a = \sqrt{(TT_v)} \tag{2.28}$$

However the backward reaction rates (recombination reaction) are function of T only. The reaction rates for exchange reactions are also calculated at T, as these reactions depends only on the relative speed of the collision which depends upon translational temperature.

2.1.5 Vibrational Source Term

In this section, the expression for the vibrational energy source term in Eq. 2.7 is presented. This source term represents the gain or loss in the vibrational energy due to exchange of energy among the translational, rotational and vibrational modes and chemical reactions. The important energy exchange mechanisms are V-T (Vibrational-Translational), V-R (Vibrational-Rotational) and V-V (Vibration-Vibration) transitions. As stated earlier, V-V transitions equilibriate with each other, so that single vibrational temperature uniquely defines vibration state of all diatomic molecules in the gas. V-T and V-R can be clubbed into one exchange rate, referred to as Q_{T-V}. With the above assumptions, Q_{T-V} can be defined by using Landau-Teller model. [26]

$$Q_{T-V\ L-T} = \rho_s \frac{e^*_{vs} - e_{vs}}{< \tau_{s\ L-T} >}, \tag{2.29}$$

where e^*_{vs} is the vibrational energy per unit mass of species s calculated at the local translational temperature, and $< \tau_{s\ L-T} >$ is the molar averaged Landau-Teller relaxation time, given by Lee [32]

$$< \tau_{s\ L-T} >= \frac{\sum_r X_r}{\sum_r X_r/\tau_{sr\ L-T}} \tag{2.30}$$

where $\tau_{sr\ L-T}$ is the Landau-Teller inter-species relaxation time, given by Millikan $et\ al.$ [33], which is reproduced below

$$\tau_{sr\ L-T} = \frac{1}{p} exp\left[A_{sr}\left(T^{-1/3} - 0.015\mu_{sr}^{1/4}\right) - 18.42\right] \qquad (p\ in\ atm)$$

$$A_{sr} = 1.16 \times 10^{-3}\mu_{sr}^{1/2}\theta_{vs}^{4/3}, \tag{2.31}$$

$$\mu_{sr} = M_s M_r / \left[M_s + M_r\right]$$

The second contribution to the vibrational source term is due to chemical reactions. The dissociation of a molecule results in drain of vibrational energy and a recombination reactions results in the increase of the vibrational energy of the gas. The amount of energy removed or added during chemical reactions depends upon the vibration-dissociation model used. In the present work we assume that, the diatomic molecules are created or destroyed with vibrational energy, defined at the local value of T_v. Hence the rate of vibrational energy production due to chemical reactions is

$$Q_{vs\ che} = w_s e_{vs} \tag{2.32}$$

The total source term due to chemical reactions is obtained by summing over all diatomic species.

$$Q_{v\ che} = \sum_{s=1}^{nd} w_s e_{vs} \tag{2.33}$$

Now the the total source term for the vibrational energy is sum of $Q_{T-V\ L-T}$ and $Q_{v\ che}$.

$$w_v = Q_{T-V\ L-T} + Q_{v\ che} \tag{2.34}$$

2.2 Governing Equations for Turbulent Flows

Turbulent flow is a randomly fluctuating flow. These fluctuations result in enhanced mixing and diffusion compared to those of laminar flow, which lead to increased heat transfer and skin friction at the wall boundaries and delayed separation. For engineering predictions, Reynolds averaging is the most widely employed method to account for the effect of these fluctuations and is explained below.

For a statistically stationary turbulent flow the instantaneous variable can be written as the sum of time averaged quantity and fluctuating quantity. Let us consider $u_i(x,t)$ as the instantaneous velocity. The time averaged velocity is known as mean velocity and is defined as follows.

$$\overline{u}_i(x) = \lim_{\mathbf{T}\to\infty} \frac{1}{\mathbf{T}} \int_t^{t+\mathbf{T}} u_i(x,t)dt \tag{2.35}$$

where $\mathbf{T}$ is time period of averaging. The time period should be selected such that it is larger than fluctuations and less than the mean flow variations. Now the instantaneous velocity can be written as

$$u_i(x,t) = \overline{u}_i(x) + u_i'(x,t) \tag{2.36}$$

where $u_i'(x,t)$ represents the fluctuations over the mean velocity. In short hand notation Eq. 2.36 is written as $u = \overline{u} + u'$. Similarly instantaneous density and pressure can be decomposed into mean variable and fluctuating variable and shown below.

$$\begin{aligned} \rho &= \overline{\rho} + \rho' \\ p &= \overline{p} + p' \end{aligned} \tag{2.37}$$

To consider the effect of density fluctuations in compressible flows, Favre or mass-weighted averaging is employed. The Favre averaged velocity ($\tilde{u}_i$) is defined as follows.

$$\tilde{u}_i(x) = \frac{1}{\overline{\rho}} \lim_{\mathbf{T}\to\infty} \frac{1}{\mathbf{T}} \int_t^{t+\mathbf{T}} \rho(x,t)u_i(x,t)dt \tag{2.38}$$

Now the instantaneous velocity is written as $u = \tilde{u} + u''$. Similarly instantaneous temperature, energy and enthalpy can be written as

$$\begin{aligned} T &= \tilde{T} + T'' \\ e &= \tilde{e} + e'' \\ h &= \tilde{h} + h'' \end{aligned} \tag{2.39}$$

The convention used in the Reynolds averaging is an over line represents averaged quantity and a single prime represents its fluctuating part. Similarly in Favre averaging a tilde represents averaged quantity and a double prime represents its fluctuating part.

2.2.1 Favre Averaged Equations

Now consider the species continuity equation Eq. 2.1 presented in Section 2.1.

$$\frac{\partial \rho_s}{\partial t} + \frac{\partial}{\partial x_j}(\rho_s u_j) - \frac{\partial}{\partial x_j}\left(\rho D \frac{\partial c_s}{\partial x_j}\right) = w_s$$

Favre averaged species continuity equation is obtained by averaging each term.

$$\frac{\partial \overline{\rho}_s}{\partial t} + \frac{\partial}{\partial x_j}(\overline{\rho}_s \tilde{u}_j) - \frac{\partial}{\partial x_j}\left(\overline{\rho} D \frac{\partial \tilde{c}_s}{\partial x_j}\right) - \frac{\partial}{\partial x_j}\left(\overline{\rho} D_T \frac{\partial \tilde{c}_s}{\partial x_j}\right) = \overline{w}_s \tag{2.40}$$

where $\tilde{u_j}$ is Favre-averaged velocity component, $\overline{\rho}_s$ is averaged species density, $\overline{\rho} = \sum_s \overline{\rho}_s$ is average mixture density and $\tilde{c_s}$ is Favre-averaged mass fraction defined as

$$\tilde{c_s} = \frac{\overline{\rho}_s}{\overline{\rho}} \tag{2.41}$$

The first and second terms in Eq. 2.40 represent unsteady and convection terms respectively and third term represents species diffusion due to concentration gradients. The last term represents species diffusion due to turbulent mixing of the fluid. In the equation D_T is turbulent diffusivity and is calculated as follows.

$$Le_T = D_T \frac{\overline{\rho} Pr_T}{\mu_T} \tag{2.42}$$

where μ_T is turbulent viscosity, Pr_T is turbulent Prandtl number and Le_T is turbulent Lewis number. Procedure to calculate these turbulent quantities is explained in the subsequent sections. The mean source term ($\overline{w}_s$) in Eq. 2.40 is calculated using the relations given in Section 2.1.4 evaluated using mean flow variables.

The Favre averaged momentum equations are

$$\frac{\partial \overline{\rho} \tilde{u}_i}{\partial t} + \frac{\partial}{\partial x_j}(\overline{\rho} \tilde{u}_i \tilde{u}_j + \overline{p}\delta_{ij}) + \frac{\partial}{\partial x_j}(\overline{\tau}_{ij}) + \frac{\partial}{\partial x_j}(\tau_{ij}^T) = 0 \tag{2.43}$$

where $\overline{\tau}_{i,j}$ is mean viscous stress tensor and $\tau_{i,j}^T$ is the Reynolds stress tensor which represents the momentum exchange due to turbulent fluctuations. $\overline{\tau}_{i,j}$ is given by

$$\overline{\tau}_{ij} = -\mu \left(\frac{\partial \tilde{u}_i}{\partial x_j} + \frac{\partial \tilde{u}_j}{\partial x_i} \right) + \frac{2}{3}\mu \frac{\partial \tilde{u}_k}{\partial x_k}\delta_{ij} \tag{2.44}$$

The Favre averaged total energy equation is

$$\frac{\partial \overline{E}}{\partial t} + \frac{\partial}{\partial x_j}((\overline{E} + \overline{p})\tilde{u}_j) - \frac{\partial}{\partial x_j}\left[(\overline{\tau}_{ij} + \tau_{ij}^T)\tilde{u}_i\right] - \frac{\partial}{\partial x_j}\left[(\overline{\kappa} + \kappa_T)\frac{\partial \tilde{T}}{\partial x_j}\right] - \tag{2.45}$$

$$\frac{\partial}{\partial x_j}\left(\left(\overline{\mu} + \frac{\mu_T}{\sigma_k}\right)\frac{\partial k}{\partial x_j}\right) - \frac{\partial}{\partial x_j}\left[(\overline{\kappa}_v + \kappa_{v\,T})\frac{\partial \tilde{e}_v}{\partial x_j}\right] - \frac{\partial}{\partial x_j}\sum_{s=1}^{ns}\overline{\rho} D \tilde{h}_s \frac{\partial \tilde{c_s}}{\partial x_j} - \frac{\partial}{\partial x_j}\sum_{s=1}^{ns}\overline{\rho} D_T h_s^0 \frac{\partial \tilde{c_s}}{\partial x_j} = 0$$

The first term represents the transient variations in the averaged total energy. The second term represents the convection of mean energy and mean pressure work. The third term represents the work done by the viscous and Reynolds stress. The fourth term represents the mean molecular

heat conduction and transport of the energy due to turbulent motion. The fifth term represents the molecular and turbulent diffusion of the turbulent kinetic energy, which is defined below. The sixth term represents the molecular and turbulent vibrational energy conduction. The last two terms represents energy transfer due to the viscous diffusion and turbulent diffusion of species. In the above equation $\overline{E}$ is Reynolds averaged total energy and is given below.

$$\overline{E} = \sum_{s=1}^{ns} \overline{\rho}_s c_{vs} \tilde{T} + \frac{1}{2}\overline{\rho}\tilde{u}_i\tilde{u}_i + \overline{E}_v + \sum_{s=1}^{ns} \overline{\rho}_s h_s^0 + \overline{\rho}k \tag{2.46}$$

where k is turbulent kinetic energy (TKE) as defined below.

$$k = \frac{1}{2}\frac{\overline{\rho u'' u''}}{\overline{\rho}} = \frac{1}{2}\widetilde{u_i'' u_i''} \tag{2.47}$$

In Eq. 2.45 κ_T and $\kappa_{v\,T}$ are turbulent translational and vibrational thermal conductivity of mixture and are given by

$$\kappa_T = \frac{\mu_T c_p}{Pr_T}, \qquad \kappa_{v\,T} = 1.2\mu_T \sum_{s=1}^{nv} \frac{\overline{\rho}_s}{\overline{\rho}} \tag{2.48}$$

where the summation is over all the vibrational modes.

The Favre averaged vibrational energy equation is given below

$$\frac{\partial \overline{E}_v}{\partial t} + \frac{\partial}{\partial x_j}(\overline{E}_v \tilde{u}_j) - \frac{\partial}{\partial x_j}\left[(\overline{\kappa}_v + \kappa_{v\,T})\frac{\partial \tilde{e}_v}{\partial x_j}\right] - \frac{\partial}{\partial_{x_j}}\sum_{s=1}^{nd}(\overline{\rho}\tilde{e}_{vs} D \frac{\partial \tilde{c}_s}{\partial x_j}) = \overline{w}_v \tag{2.49}$$

The first two terms represents the unsteady and convection of the vibrational energy. The third term represents the mean and turbulent conduction of vibrational energy. The last term represents the transport of the vibrational energy due to the molecular diffusion of the species. The effect of the turbulent fluctuations on the this term are neglected. w_v is mean source term for vibrational energy and is calculated using the relations given Section 2.1.5 evaluated using mean flow variables.

In Favre averaged equations the Reynolds stresses ($\tau_{i,j}^T$) are calculated using Boussinesq assumption, which states that the Reynolds stresses are proportional to mean velocity gradients and turbulent viscosity (μ_T). The turbulent viscosity is also known as the eddy viscosity. Hence $\tau_{i,j}^T$ is given by

$$\tau_{ij}^T = -\mu_T\left[\tilde{s}_{ij} + \frac{2}{3}\frac{\partial \tilde{u}_k}{\partial x_k}\delta_{ij}\right] - \frac{2}{3}\overline{\rho}k\delta_{ij} \tag{2.50}$$

Where $\tilde{s}_{ij}$ is mean strain rate tensor given by

$$\tilde{s}_{ij} = \frac{1}{2}\left[\frac{\partial \tilde{u}_i}{\partial x_j} + \frac{\partial \tilde{u}_j}{\partial x_i}\right] \tag{2.51}$$

In the present work, we assume constant turbulent Prandtl number (Pr_T) of 0.9 and constant turbulent Lewis number (Le_T) of 1.

Now specification of μ_T is required to close the above Favre averaged equations. Turbulence models are employed to compute μ_T. Turbulence models are classified based upon the number of equations that are solved to calculate μ_T. One equation models solve one extra transport equation to compute the eddy viscosity. In two equation models two extra transport equations are solved to compute the eddy viscosity. In the present thesis, one equation Spalart-Allmaras model is used and its details are described below.

2.2.2 Spalart-Allmaras Model [34]

In Spalart-Allmaras (SA) one equation model [34], kinematic eddy viscosity ($\nu_T = \mu_T/\rho$) is calculated using the following relation.

$$\nu_T = \tilde{\nu} f_{v1} \tag{2.52}$$

where f_{v1} is damping function and $\tilde{\nu}$ is flow dependent variable, for which the following transport equation is solved.

$$\frac{\partial \tilde{\nu}}{\partial t} + \tilde{u_j}\frac{\partial \tilde{\nu}}{\partial x_j} = c_{b1}\tilde{S}\tilde{\nu} - c_w f_w \left(\frac{\tilde{\nu}}{d}\right)^2 + \frac{1}{\sigma}\left[\nabla.\left(((\nu+\tilde{\nu})\nabla\tilde{\nu}) + c_{b2}(\nabla\tilde{\nu})^2\right)\right] \tag{2.53}$$

First term and second terms on right hand side (RHS) of Eq. 2.53 represent the production and destruction of the eddy viscosity. The last term represents the turbulent diffusion of the eddy viscosity. The wall damping function f_w, f_{v1} and $\tilde{S}$ are defined as follows.

$$f_w = g\left[\frac{1+c_{w3}^6}{g^6+c_{w3}^6}\right], \quad f_{v1} = 1 - \left[\frac{\chi^3}{\chi^3+c_{v1}^3}\right], \quad \tilde{S} = S + f_{v2}\left(\frac{\tilde{\nu}}{\kappa^2 d^2}\right) \tag{2.54}$$

where

$$g = r + c_{w2}(r^6 - r), \quad r = \frac{\tilde{\nu}}{\tilde{S}\kappa^2 d^2}, \quad \chi = \frac{\tilde{\nu}}{\nu}, \quad f_{v2} = 1 - \left[\frac{\chi}{1+\chi f_1}\right] \tag{2.55}$$

d is distance from the wall and S is vorticity magnitude, given by

$$S = \sqrt{2\Omega_{ij}\Omega_{ij}}, \qquad \Omega_{ij} = \frac{1}{2}\left[\left(\frac{\partial \tilde{u_i}}{\partial x_j}\right) - \left(\frac{\partial \tilde{u_j}}{\partial x_i}\right)\right] \tag{2.56}$$

Where Ω_{ij} is the rotation tensor. The closure constants are $c_{b2} = 0.1355$, $c_{b1} = 0.622$, $c_{v1} = 7.1$, $\sigma = 2/3$, $\kappa = 0.41$, $c_{w1} = \frac{c_{b1}}{\kappa^2} + \frac{(1+c_{b2})}{\sigma}$, $c_{w2} = 0.3$ and $c_{w3} = 2$. The boundary conditions for $\tilde{\nu}$ are $\tilde{\nu}_\infty = \frac{0.1\mu_\infty}{\rho_\infty}$ in the freestream, and $(\nu_T)_w = 0$ at the wall.

2.3 Finite Volume Method

Finite volume methods (FVM) are based on integral form of fluid flow equations and hence capable of capturing the shock waves and contact discontinuities. The basic concept of FVM is to divide the domain into finite number of grid cells and approximate the total integral of conserved quantities ($i.e.$ mass, momentum and energy) over the grid cell divided by cell volume as the cell average of conserved quantity and these values are modified in each time step by flux through the cell edges. Cell-averaged values are used for calculating fluxes.

Let us consider this approach in more detail. The governing equations presented in previous section can be written in conservation form as follows.

$$\frac{\partial U}{\partial t} + \frac{\partial F_I}{\partial x} + \frac{\partial G_I}{\partial y} + \frac{\partial F_V}{\partial x} + \frac{\partial G_V}{\partial y} = W \tag{2.57}$$

Where U is the vector of conserved variables.

$$U = (\rho_1, \rho_2, ..., \rho_{ns}, \rho u, \rho v, E_v, E)^T \tag{2.58}$$

F and G are flux vectors in x and y directions respectively. The subscripts I and V represent inviscid and viscous fluxes respectively. The flux terms are given by

$$F_I = \begin{bmatrix} \rho_1 u \\ \rho_2 u \\ . \\ . \\ . \\ \rho_{ns} u \\ \rho u v + p \\ \rho v u \\ E_v u \\ (E+p)u \end{bmatrix} \qquad G_I = \begin{bmatrix} \rho_1 v \\ \rho_2 v \\ . \\ . \\ . \\ \rho_{ns} v \\ \rho u v \\ \rho v u + p \\ E_v v \\ (E+p)v \end{bmatrix} \tag{2.59}$$

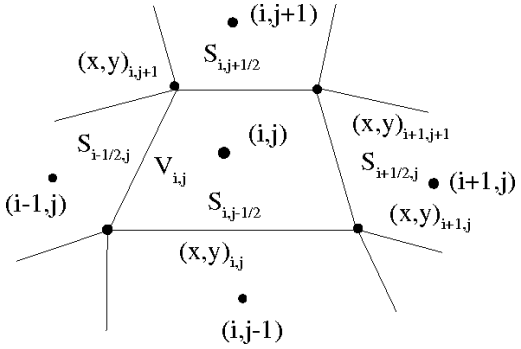

Figure 2.1: A typical quadrilateral finite volume cell. Cell centers and nodes are marked with filled symbols.

$$F_V = \begin{bmatrix} \rho_1 u_1 \\ \rho_2 u_2 \\ . \\ . \\ . \\ \rho_{ns} u_{ns} \\ -\tau_{xx} \\ -\tau_{xy} \\ q_{v_x} + \sum_{s=1}^{nd} (r_s e_{v_s} u_s) \\ q_x + q_{v_x} - (\tilde{\tau}\vec{u})_x + \sum_{s=1}^{nd} (r_s h_s u_s) \end{bmatrix} \quad G_V = \begin{bmatrix} \rho_1 v_1 \\ \rho_2 v_2 \\ . \\ . \\ . \\ \rho_{ns} v_{ns} \\ -\tau_{yx} \\ -\tau_{yy} \\ q_{v_y} + \sum_{s=1}^{nd} (r_s e_{v_s} v_s) \\ q_y + q_{v_y} - (\tilde{\tau}\vec{u})_y + \sum_{s=1}^{nd} (r_s h_s v_s) \end{bmatrix} \tag{2.60}$$

The source term vector W is given by $U = (w_1, w_2, ..., w_{ns}, 0, 0, w_v, 0)^T$. The Eq. 2.57 can be represented in compact form as follows

$$\frac{\partial U}{\partial t} + \bigtriangledown . \vec{F} = W \tag{2.61}$$

Where $\vec{F}$ is the flux vector and is given by

$$\vec{F} = (F_I + F_V)\hat{i} + (G_I + G_V)\hat{j} \tag{2.62}$$

Integrating the Eq. 2.61 over a finite volume, Ω_i shown in Fig. 2.1

$$\int_{\Omega_i} \frac{\partial U}{\partial t} d\Omega + \oint_{\Omega_i} (\bigtriangledown . \vec{F}) d\Omega = \oint_{\Omega_i} W d\Omega \tag{2.63}$$

Using Gauss divergence theorem and assuming that boundary and volumes of the discretized cells do not change with time, we get

$$\frac{\partial}{\partial t}\int_{\Omega_i} U d\Omega + \oint_{\partial\Omega} (\vec{F}.\hat{n}) dS = \oint_{\Omega_i} W d\Omega \tag{2.64}$$

Where $\hat{n}$ is surface normal and dS is surface area of the cell. Assuming U to be an averaged value which is constant with in the finite volume cell, then first integral can be written as

$$\frac{\partial}{\partial t}\int_{\Omega_i} U d\Omega = V_{i,j}\frac{d\bar{U}}{dt} \tag{2.65}$$

For a typical quadrilateral cell shown in Fig. 2.1 the second integral can be written as

$$\oint_{\partial\Omega} \vec{F}.\hat{n} dS = \sum_{k=1}^{4} (\vec{F}.\hat{n})_k S_k \tag{2.66}$$

$$= (\vec{F}.\hat{n})_{i+\frac{1}{2},j} S_{i+\frac{1}{2},j} - (\vec{F}.\hat{n})_{i-\frac{1}{2},j} S_{i-\frac{1}{2},j} + (\vec{F}.\hat{n})_{i,j+\frac{1}{2}} S_{i,j+\frac{1}{2},j} - (\vec{F}.\hat{n})_{i,j-\frac{1}{2}} S_{i,j-\frac{1}{2}}$$

The expression $\vec{F}.\hat{n}$ represents the normal flux through the face under consideration (as indicated by subscripts) and S is area of the corresponding face. Time derivative in Eq. 2.65 is discretized using backward Euler time integration

$$\frac{d\bar{U}}{dt} = \frac{U_{i,j}^{n+1} - U_{i,j}^{n}}{\triangle t} \tag{2.67}$$

Substituting the above approximated integrals in Eq. 2.64, we get the discretized form of the finite volume approach

$$\begin{aligned} \frac{U_{i,j}^{n+1} - U_{i,j}^{n}}{\triangle t} = \frac{1}{V}\left[(\vec{F}.\hat{n})_{i+\frac{1}{2},j} S_{i+\frac{1}{2},j} - (\vec{F}.\hat{n})_{i-\frac{1}{2},j} S_{i-\frac{1}{2},j}\right] + \\ \frac{1}{V}\left[+(\vec{F}.\hat{n})_{i,j+\frac{1}{2}} S_{i,j+\frac{1}{2},j} - (\vec{F}.\hat{n})_{i,j-\frac{1}{2}} S_{i,j-\frac{1}{2}}\right] + \bar{W} \end{aligned} \tag{2.68}$$

Where $\bar{W}$ is averaged source term over the cell Ω. Finite volume method requires the integration of the fluxes at the cell interfaces, and these details are explained next.

2.3.1 Integration of the Inviscid Fluxes

In the present work, modified stegar-warming flux vector splitting [35] approach is used to evaluate the inviscid fluxes. Brief details of the method are given below.
consider the inviscid normal flux through the face

$$F_I' = \vec{F}.\hat{n} = \begin{bmatrix} \rho_1 u' \\ \rho_2 u' \\ . \\ . \\ . \\ \rho_{ns} u' \\ \rho u u' + p s_x' \\ \rho v u' + p s_y' \\ E_v u' \\ (E+p)u' \end{bmatrix} \tag{2.69}$$

Where $u' = u s_x' + v s_y'$ is velocity normal to the face; s_x' and s_y' are direction-cosines of the surface normal vector $\hat{n}$. The inviscid flux terms can be written as

$$F_I' = A'U \tag{2.70}$$

Where A' is jacobian of flux vector F_I' and it is diagonalized as follows

$$A' = \frac{\partial F_I'}{\partial U} = S^{-1}C^{-1}\lambda CS \tag{2.71}$$

Where $\lambda = \mathrm{diag}(u', u', u', u'-a, u'+a)$ is a diagonal matrix whose elements are eigen values. The flux vector is now splitted into positive and negative parts depending on the sign of eigen values.

$$F' = F_+' + F_-' \tag{2.72}$$

$$F_+ = A_+U \qquad\qquad F_- = A_-U \tag{2.73}$$

Now the flux at cell boundary, $i+\frac{1}{2}, j$ can be evaluated using Eqs. 2.71 and 2.74

$$F'_{i+\frac{1}{2},j} = SC\lambda_+C^{-1}S^{-1}U_{i,j} + SC\lambda_-C^{-1}S^{-1}U_{i+1,j} \tag{2.74}$$

Where λ_+ and λ_- consist of positive and negative eigen values respectively. In the above expression the jacobians are calculated based on the cell averaged values which was proposed by stegar-warming. However it is found to result in excessive dissipation in the boundary layer. Candler and Mac-Cormack proposed a low-dissipation scheme [35], where the jacobian matrices are evaluated at the cell interface. This is found to reduce the numerical dissipation. The fluxes in the modified steger-Warming method are calculated as follows

$$
\begin{aligned}
F'_{+_{i+\frac{1}{2},j}} &= A_{+_{i+\frac{1}{2},j}} U_{i,j} \\
F'_{-_{i+\frac{1}{2},j}} &= A_{-_{i+\frac{1}{2},j}} U_{i+1,j}
\end{aligned}
\tag{2.75}
$$

Average of $U_{i,j}$ and $U_{i+1,j}$ will be used for evaluating $A_{\pm_{i+\frac{1}{2},j}}$

$$
A_{\pm_{i+1/2}} = A_{\pm}\left[\frac{1}{2}(U_i + U_{i+1})\right] \tag{2.76}
$$

2.3.2 Second Order Spacial Accuracy

The finite volume scheme said to be first order accurate when interface fluxes are calculated using cell averaged values ($U_{i,j}$), on the other hand, if one uses point values of U at the cell boundary, then the scheme said to be higher order scheme. Hence cell averaged values need to be reconstructed to cell edges, to obtain the point values at the interface. A scheme said to be second order spacial accurate, when liner interpolation is used in the reconstruction of solution. The flux expressions for second order spacial accuracy are

$$
\begin{aligned}
F'_{+_{i+\frac{1}{2},j}} &= A_{+_{i+\frac{1}{2},j}} U^L_{i+\frac{1}{2},j} \\
F'_{-_{i+\frac{1}{2},j}} &= A_{-_{i+\frac{1}{2},j}} U^R_{i+\frac{1}{2},j}
\end{aligned}
\tag{2.77}
$$

Where the superscripts L and R refers to cells on left and right side of $i+\frac{1}{2}$ face respectively, and the corresponding state vectors are evaluated as follows

$$
\begin{aligned}
U^L_{i+\frac{1}{2},j} &= \tfrac{3}{2}U_i - \tfrac{1}{2}U_{i-1} \\
U^R_{i+\frac{1}{2},j} &= \tfrac{3}{2}U_{i+1} - \tfrac{1}{2}U_{i+2}
\end{aligned}
\tag{2.78}
$$

2.3.3 Evaluation of the Viscous Fluxes

The viscous normal flux across a cell face in the finite volume formulation is given by (from Eqs. 2.60 and 2.62)

$$
F'_V = F_V s'_x + G_V s'_y \tag{2.79}
$$

The vectors F_V and G_V contain shear stress and heat flux terms (see Eq. 2.60) which are function of velocity and temperature gradients. Due to elliptic nature these terms, a central difference approximation can be used to calculate the gradients. However co-ordinate transformation is required to compute these derivatives on arbitrary ξ-η coordinate system. Now consider the velocity derivative

$$\frac{\partial u}{\partial x} = \frac{\partial u}{\partial \xi}\frac{\partial \xi}{\partial x} + \frac{\partial u}{\partial \eta}\frac{\partial \eta}{\partial x} \tag{2.80}$$

The derivatives in ξ-η co-ordinates are given by

$$\frac{\partial u}{\partial \xi} = \frac{u_{i+1,j} - u_{i,j}}{1} \tag{2.81}$$

$$\frac{\partial u}{\partial \eta} = \frac{u_{i+1/2,j+1} - u_{i+1/2,j-1}}{2} \tag{2.82}$$

The values $u_{i+1/2,j+1}$ and $u_{i+1/2,j-1}$ are obtained by averaging the adjacent cells of face $i + 1/2$ at $j + 1$ and $j - 1$ (see Fig. 2.1). Hence

$$\frac{\partial u}{\partial \eta} = \frac{1}{2}\left[\frac{1}{2}\left(u_{i,j+1} + u_{i+1,j+1}\right) - \frac{1}{2}\left(u_{i,j-1} + u_{i+1,j-1}\right)\right] \tag{2.83}$$

The other parameters in the shear stress and heat flux $i.e.$ viscosity, μ and thermal conductivity κ need to be evaluated at the cell face. For example, κ should be calculated at temperature that is obtained by averaging across the cell face.

The turbulent fluxes are also evaluated in a similar method. The source terms are computed at the cell centers and the derivatives required to calculate the source terms are evaluated using central differences.

2.3.4 Time Integration

Advancing the solution from current iteration to next iteration is referred to as time integration. In explicit formulation, the solution is advanced in time using the update function Eq. 2.68. The flux and source terms in this equation are evaluated from the solution of n^{th} iteration.

$$\begin{aligned}\triangle U^n_{i,j} = \tfrac{\triangle t}{V_{i,j}}\left[(\vec{F}.\hat{n})_{i+\frac{1}{2},j} S_{i+\frac{1}{2},j} - (\vec{F}.\hat{n})_{i-\frac{1}{2},j} S_{i-\frac{1}{2},j}\right]^n \\ + \tfrac{\triangle t}{V_{i,j}}\left[(\vec{F}.\hat{n})_{i,j+\frac{1}{2}} S_{i,j+\frac{1}{2},j} - (\vec{F}.\hat{n})_{i,j-\frac{1}{2}} S_{i,j-\frac{1}{2}} + \bar{W}\right]^n\end{aligned} \tag{2.84}$$

Where $\triangle U^n_{i,j} = U^{n+1}_{i,j} - U^n_{i,j}$ is the residual or correction factor. Starting with an initial guess, the solution is iteratively updated until the solution converges when the L_2 norm of the residual becomes small compared to its initial value.

The stability criteria restricts the time step to lower values in the explicit methods. Therefore with the lower time steps, many iterations are required to obtain a steady state solution. This is much more severe when computing the non-equilibrium reacting flows. To alleviate

time step restriction, implicit methods are developed. In these methods large time steps can be taken. As a result, a steady state solution can be obtained with lesser number of iterations compared to those of the explicit method.

In the implicit method, solution at a point depends on the solution of its neighboring points at the same time level. This requires the fluxes at the cell interfaces in Eq. 2.68 to be evaluated at the $(n+1)^{\text{th}}$ level. Following linearization is used to obtain the implicit fluxes at $(n+1)^{\text{th}}$ level.

$$F_I'^{n+1} = F_I'^{n} + \left[\frac{\partial F_I'}{\partial U}\right]^n \left(U^{n+1} - U^n\right) \approx F_I'^{n} + A'^{n}\delta U^n \tag{2.85}$$

where $\delta U^n = U^{n+1} - U^n$. The viscous fluxes are linearized as follows.

$$F_V'^{\,n+1} = F_V'^{\,n} + \delta F_V'^{\,n} \tag{2.86}$$

The correction terms $\delta F_V'^{\,n}$ is calculated using thin layer approximation [3], $i.e.$ only derivatives in the normal direction are retained.

$$\delta F_V'^{\,n} \approx M_\eta \frac{\partial V}{\partial \eta} = M_\eta N \frac{\partial U}{\partial \eta} \tag{2.87}$$

Where $V = (\rho_1, \rho_2, ..., \rho_{ns}, u, v, T_v, T)^T$ and $N = \partial V/\partial U$ is the corresponding jacobian. The matrices M_η and N are given Ref. 7. The final form of the viscous flux at $(i, j+\frac{1}{2})$ is given by

$$F_{V\,i,j+\frac{1}{2}}'^{\,n+1} = F_{V\,i,j+\frac{1}{2}}'^{\,n} + \left(M_\eta N\right)^n_{i,j+\frac{1}{2}} \left(\delta U^n_{i,j+1} - \delta U^n_{i,j}\right) \tag{2.88}$$

Additional details about the linearization of the viscous fluxes can be found in [7]. substitution of jacobians given by Eqs. 2.85 and 2.88 in Eq. 2.68 gives the following implicit formulation for the update function.

$$\hat{A}_{i,j}\delta U^n_{i,j} + \hat{B}_{i,j}\delta U^n_{i,j+1} + \hat{C}_{i,j}\delta U^n_{i,j-1} + \hat{D}_{i,j}\delta U^n_{i+1,j} + \hat{E}_{i,j}\delta U^n_{i-1,j} = \triangle U^n_{i,j} \tag{2.89}$$

where $\triangle U^n_{i,j}$ is the explicit residual given by Eq. 2.84. In the above equation the coefficients are given by

$$\begin{aligned}
\hat{A}_{i,j} &= \tfrac{V_{i,j}}{\triangle t} I + (A'^{n}_{+i+\frac{1}{2},j} S_{i+\frac{1}{2},j} - A'^{n}_{-i-\frac{1}{2},j} S_{i-\frac{1}{2},j} \\
&\qquad + B'^{n}_{+i,j+\frac{1}{2}} S_{i,j+\frac{1}{2}} - B'^{n}_{-i,j-\frac{1}{2}} S_{i,j-\frac{1}{2}}) - V_{i,j} C^n_{i,j} \\
\hat{B}_{i,j} &= B'^{n}_{-i,j+\frac{1}{2}} S_{i,j+\frac{1}{2}} \\
\hat{C}_{i,j} &= B'^{n}_{+i,j-\frac{1}{2}} S_{i,j-\frac{1}{2}} \\
\hat{D}_{i,j} &= A'^{n}_{-i+\frac{1}{2},j} S_{i+\frac{1}{2},j} \\
\hat{E}_{i,j} &= A'^{n}_{+i-\frac{1}{2},j} S_{i-\frac{1}{2},j}
\end{aligned} \tag{2.90}$$

Where $C^n_{i,j}$ is the jacobian of W with respect to U.

2.3.5 Solution Procedure

A solution can be obtained by applying the implicit update function Eq. 2.89 at all the grid points in the computational domain. This results in a system of liner equations, which can be solved by matrix inverse methods. However the resulting matrix is a large banded matrix, and inverting the matrix for each iteration is computationally intensive task. Therefore approximate methods are developed to reduce the computational time, without losing accuracy. In the present work, Data Parallel Line Relaxation method [22] is used to obtain a approximate solution to Eq. 2.89. A brief description of the method is given below.

In case of external flows, gradients in the body-normal direction are larger than those in the body-parallel direction. Therefore, the physical problem is strongly coupled in the body-normal direction. This fact is used to obtain a solution to the Eq. 2.89. Only j terms are solved by moving $i+1$ and $i-1$ terms to the right hand side. The resulting equation is

$$\hat{A}_{i,j}\delta U + \hat{B}_{i,j}\delta U_{i,j+1} + \hat{C}_{i,j}\delta U_{i,j-1} = \triangle U_{i,j} - \hat{D}_{i,j}\delta U_{i+1,j} + \hat{E}_{i,j}\delta U_{i-1,j} \tag{2.91}$$

The above equation is solved for all j- points at a fixed i- location. Therefore the method is fully coupled in j- direction. The above equation is solved along each i- line in alternating forward and backward sweeps through the flowfield in the i- direction.

2.4 Summary

In this chapter, governing equations for thermo-chemical non-equilibrium flows and numerical details of the in-house CFD code are presented. Air is treated as a mixture of five perfect species: N_2, O_2, NO, N and O. A single vibrational temperature defines the mixture vibrational energy. Blottner model is used to calculate the viscosity of individual species. Wilke's mixing rule is used to calculate the mixture transport properties. The Arrhenius rate constants for the chemical reactions are evaluated using curve fits to experimental data by Park. Landu-Teller model is used to calculate the vibrational relaxation rate. The axisymmetric form of the governing equations is discretized using the finite-volume method. Inviscid fluxes are computed using a modified (low-dissipation) form of the Steger-Warming flux splitting approach. The implicit data parallel line relaxation method is used to obtain steady-state solutions.

Chapter 3

Aero-heating Predictions at Flight Condition

The chapter addresses the computation of re-entry flowfield at flight condition considering the finite rate thermo-chemistry. Simulations are performed over FIRE II re-entry capsule at 35 km altitude trajectory point. The chosen capsule is a practical geometry of the vehicle that was flight tested. The computations are performed on the entire vehicle that includes afterbody portion also. The computed surface properties are validated against the flight data. The capability of CFD in predicting the afterbody separated flows is shown through this case study.

3.1 FIRE II Configuration

Project FIRE (Flight Investigation Reentry Experiment) flights [36] were conducted to investigate the heating environment on a blunt-nosed, Apollo-shaped vehicle entering the earth's atmosphere at a velocity in excess of the escape velocity. Fig. 3.1(a) and 3.1(b), taken from Ref. 36, show a schematic of the FIRE II vehicle. The spherical forebody consisted of a multi-layer configuration made of three protective phenolic asbestos heat shields sandwiched between three beryllium calorimeters. The first two calorimeters and their associated heat shields were jettisoned during the flight at predetermined deceleration loads. The third heat shield was not ejected and this gives the shape of the vehicle through the later part of the re-entry that is of interest in this work. The outer mold line used in the current simulations is shown in Fig. 3.1(c). The vehicle diameter is 58.79 cm with a nose radius of 70.2 cm. The shoulder/corner radius is 0.61 cm and the base radius is 4.2 cm. The afterbody is conical with a 66^0 included angle, and

Table 3.1: Freestream conditions at the 35 km altitude trajectory point.

Free-stream Conditions	
Time from launch (sec)	1652.75
ρ_∞ (kg/m^3)	0.0082
U_∞ (m/s)	4950
T_∞ (K)	237
M_∞	16
$Re_{\infty D}$	1.76×10^6
H_0 (MJ/kg)	12.42

the C-band antenna at the base is replaced by a flat base for simplicity. Also, geometrical details at the heatshield-aftshell junction and the ring-like structure at the base are not considered in the outer mold line presented in Fig. 3.1(c). Their effect on the flow structure is studied separately in section IV D.

The FIRE II vehicle entered earth atmosphere at 11.2 km/s. It decelerated to a velocity of 4950 m/s (Mach 16) at 35 km altitude. Slocumb [36] presents the time history of altitude and velocity over the entire descent. We simulate the conditions (listed in Table. 3.1) at the 35 km trajectory point, which corresponds to one of the lowest altitudes and highest Reynolds numbers for which measurements are available. The Reynolds number based on freestream conditions and body diameter is 1.76×10^6. Blunt body separation shear layer and inner wake transition correlations are presented by Lees [37]. A transition criteria is defined in terms of the Reynolds number computed using local flow properties outside the wake. The distance measured along the shear layer, starting from the separation point, is used as the relevant length scale to identify the physical location where the Reynolds number approaches transitional range. Based on these correlations and data from preliminary simulations of the FIRE II configuration, the wake is expected to transition upstream of the neck.

The vehicle afterbody was instrumented for pressure and surface temperature measurements. Pressure was measured at a single location and twelve gold calorimeters were placed at four axial locations along three circumferential rays ($\phi = 0$, 120 and 240 degs). Here, ϕ denotes the azimuthal angle around the vehicle, as shown in Fig. 3.1(b). The system accuracy, including that of sensors and telemetry system, was approximately $\pm 20\%$ for the pressure data

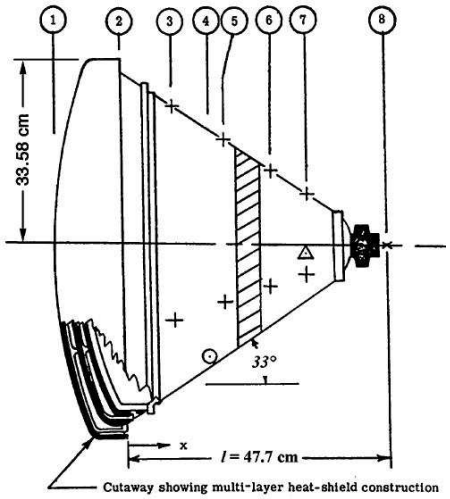

(a)

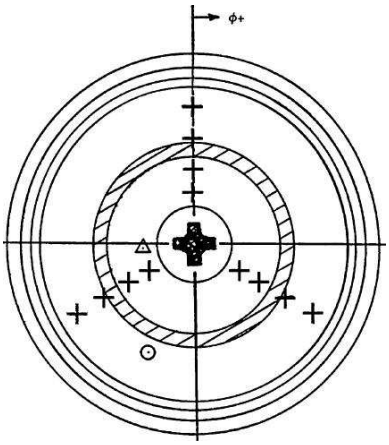

(b)

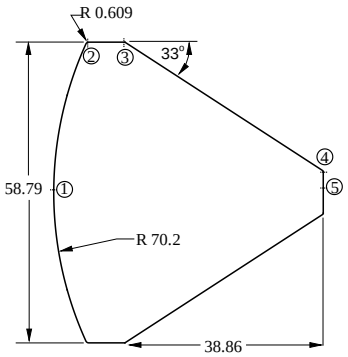

(c)

Figure 3.1: FIRE II re-entry vehicle with afterbody instrumentation[32] (a) side view (b) rear view. $+$, $\triangle$ and $\odot$ represents gold calorimeters, pressure sensor and radiometer respectively. (c) Outer mold line used for the current simulations. All dimensions are in cm. Critical geometrical points are (1) fore stagnation point, $s/D = 0$ (2) fore shoulder, $s/D = 0.51$ (3) heatshield-backshell interface, $s/D = 0.64$ (4) aft shoulder, $s/D = 1.42$ (5) aft stagnation point, $s/D = 1.49$.

and about $\pm 28^{\circ}$ K for the temperature measurements. The corresponding error in heat transfer measurement is estimated to be $\pm 15\%$ [38]. The surface temperature measured by the calorimeters is presented as a function of re-entry elapsed time. From this temperature-time history, an average wall temperature of 553.3 K is taken at 35 km altitude. In the later part of the trajectory the vehicle has periodic motion about its axis, resulting in oscillations in the effective angle of attack. However, there is negligible effect of angle of attack variation on the afterbody measurements, with no appreciable difference between the heating rates along the three circumferential rays [36]. The angle of attack is therefore assumed to be zero in the current simulations.

3.2 Simulation Methodology

The chemically reacting turbulent hypersonic flow around the FIRE II re-entry configuration is simulated by solving the Reynolds-averaged Navier-Stokes (RANS) equations along with a finite rate chemistry model. The details of the RANS and chemistry model are presented in Chapter 2. The freestream total enthalpy at the current condition (12.73 MJ/kg) is similar to that of Apollo AS-202 computations in Ref. 39, where ionization is found to be negligible. Hence air is modeled as a neutral mixture of five perfect species (N_2, O_2, NO, N and O) with three dissociation and two exchange reactions. The Spalart-Allmaras (SA) model [34] is used for turbulence closure. The standard form of the turbulence model, without compressibility corrections, is used in the present work. Chemical and vibrational source terms are evaluated using mean flow properties, such that effect of turbulence-chemistry interaction is neglected.

No-slip, non-catalytic and isothermal boundary conditions are specified at the wall. The boundary conditions for turbulent quantities are $\nu_{T\infty} = 0.1\mu_{\infty}/\rho_{\infty}$ and $\nu_{T,w} = 0$ as given in Ref. 34. Freestream conditions are applied at the outer boundary and extrapolation boundary condition is imposed at the exit station. The simulation results are found to be insensitive to the specific values of ν_T prescribed in the freestream.

3.2.1 Computational Grid

A typical grid used in the simulations is shown in Fig. 3.2. The outer boundary follows the shape of the bow shock and extends up to 2.5 diameters downstream of the vehicle base. The flow at this point is found to be supersonic and therefore the location of the exit boundary is not expected to alter the flow solution in the vicinity of the vehicle. A typical grid consists of

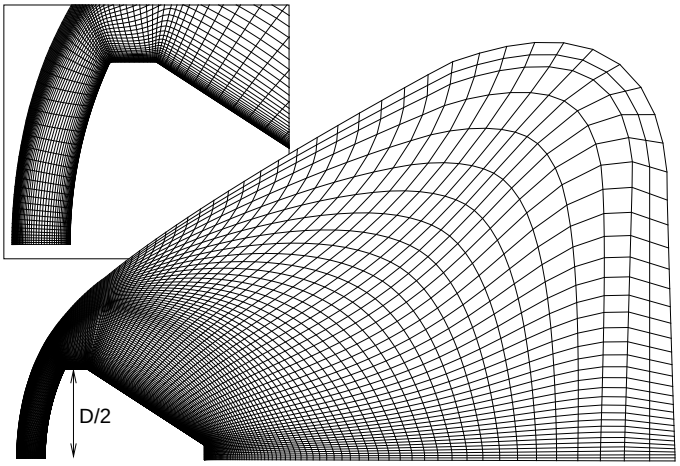

Figure 3.2: Computational domain and a typical grid used in the simulations. The inset shows a magnified view of the grid near the vehicle, where every second point is shown in each direction.

about 160 points in the wall parallel direction (i) and 150 points in the wall normal direction (j). Grids with larger number of points are also used in some cases.

The forebody grid in the i-direction is designed such that points are clustered in the nose stagnation region and at the shoulder expansion corner. The grid in the j-direction is refined both in the vicinity of the shock wave as well as in the near wall region. In addition, the outer boundary is carefully tailored to the bow shock wave. The forebody grid refinement follows the same procedure as delineated in Ref. 40 and details are omitted for the sake of brevity. The current paper is focussed on the afterbody solution and a careful grid refinement in the afterbody region is presented below.

A careful grid refinement study was undertaken for the afterbody flowfield by identifying the critical regions, where the flow solution is most sensitive to the computational mesh. The grid is successively refined with a focus on the critical zones and the grid lines are adapted to the prominent flow features like the free-shear layer enclosing the recirculation bubble. The effect of grid changes on the afterbody surface pressure and heating rate is studied, and a tolerance of 2% of the base stagnation point value is taken as the grid-independence criterion. Figures 3.3 and 3.4 show the results from the grid refinement study using the SA turbulence model, where pressure, normalized by its freestream value, and heat transfer rate are plotted as a function of the normalized arc-length (s/D) measured from the nose of the vehicle. The extent of conical frustum and flat base are marked by vertical lines.

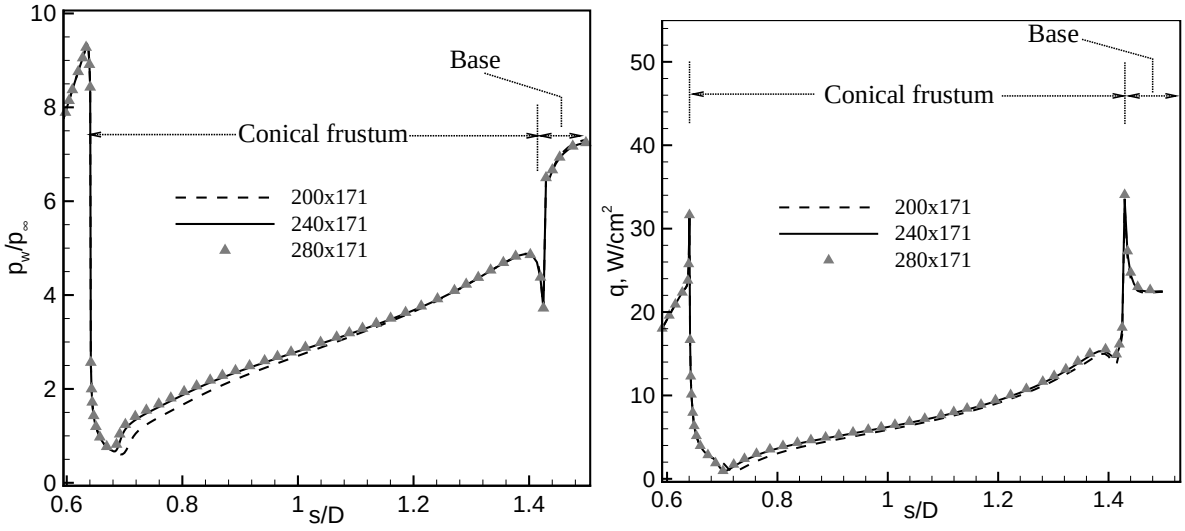

Figure 3.3: (a) Normalized pressure and (b) heat transfer rate on the afterbody computed using successively refined grids in wall-parallel direction.

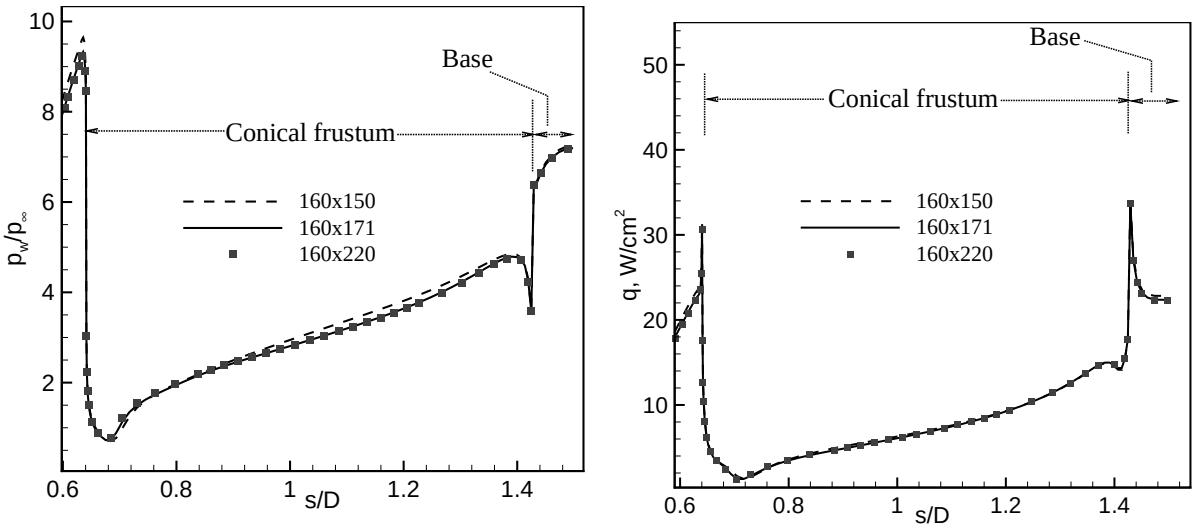

Figure 3.4: (a) Normalized pressure and (b) heat transfer rate on the afterbody computed using successively refined grids in wall-normal direction.

Afterbody flowfield is sensitive to the distribution of grid points and the quality of the computational mesh in regions where the flow gradients are high. In the wall parallel direction, for example, these correspond to the geometric corners, stagnation point at the base, and the separation point on the conical frustum. Zonal grid refinement in these regions is done to identify the most critical requirements. It is found that a fine grid near the separation point

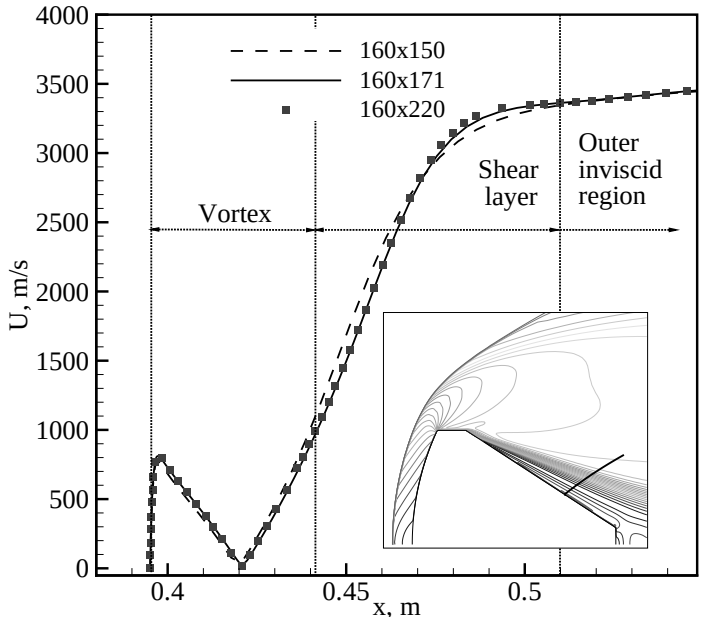

Figure 3.5: Effect of wall normal grid refinement on velocity distribution across the free shear layer. Data is plotted along the line shown in the inset.

along with a low stretching factor on the conical frustum is necessary for grid convergence. The results are however not so sensitive to the grid spacing at the rear stagnation point and the expansion corner at the base. Three grids with successive refinement along the conical frustum, especially near the separation point, are used to compute the flow and the results are presented in Fig. 3.3. The two finer grids (240×171 and 280×171) yield practically identical (within 1%) pressure and heat transfer results on the afterbody. 240 points in the wall-parallel direction is therefore taken to be adequate for a grid-independent solution.

In the wall-normal direction, special attention is given to the accurate resolution of the free shear layer enclosing the recirculation bubble. Three grids (160×150, 160×171, and 160×220) with successive refinement in the j-direction are used to compute the flow. Majority of the refinement is localized in the free shear layer and the recirculation bubble. The velocity distribution across the shear layer (see Fig. 3.5) shows almost overlapping results from the two finer grids. Also the pressure and heating rates obtained on the three grids are comparable, with negligible difference between the two finer grids (Fig. 3.4). 171 points are therefore taken to be adequate in the wall-normal direction.

Further, the computational mesh in the near wake is modified such that the grid lines are parallel to the shear layer. This is done by identifying a separate grid block enclosing the

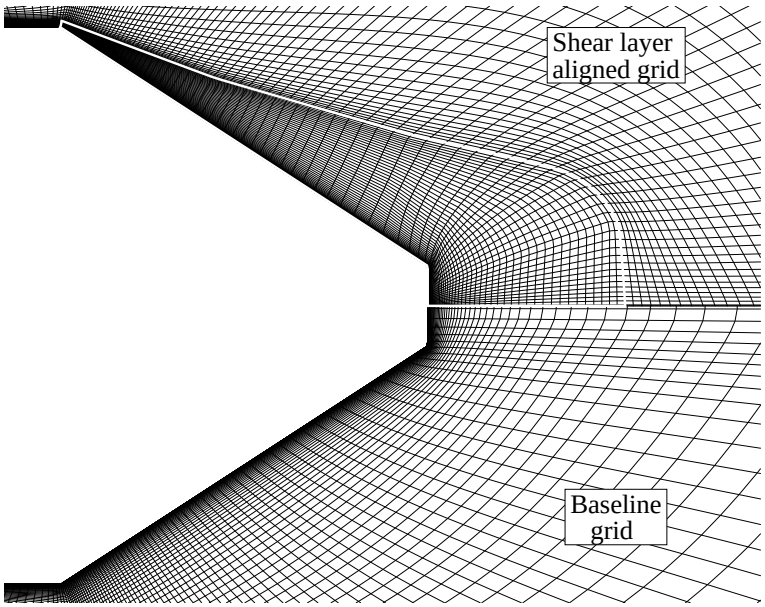

Figure 3.6: Grid point distribution in the baseline grid (bottom half) and a modified grid that is adapted to the shear layer (top half). White line identifies the boundary of the grid block enclosing the shear layer and separation bubble.

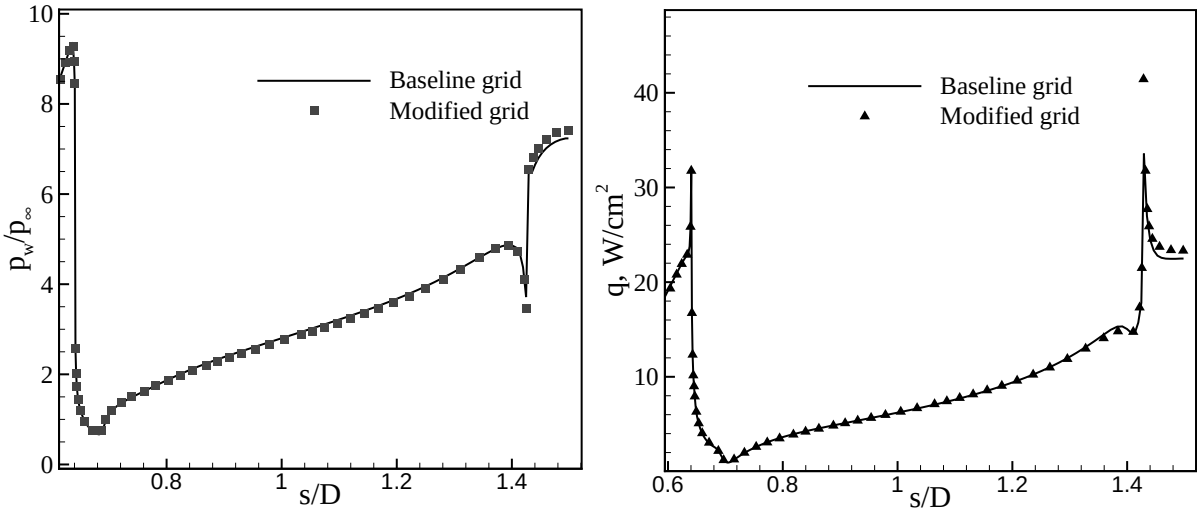

(a) (b)

Figure 3.7: (a) Normalized pressure and (b) heat transfer rate on the afterbody computed using the baseline grid and a modified grid that is adapted to the shear layer.

recirculation bubble and the shear layer (see Fig. 3.6), and carefully controlling the distribution of points along the block boundaries. The shear-layer adapted grid yields practically identical size of separation bubble and shear layer location compared to the baseline grid (bottom half of

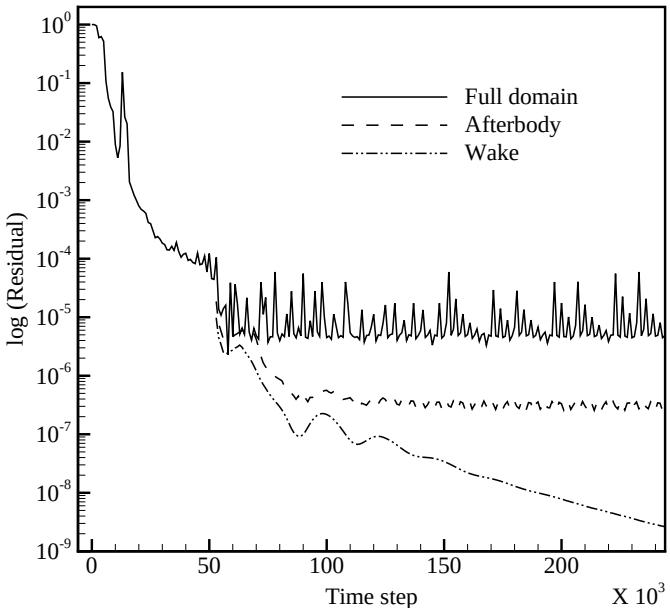

Figure 3.8: Residual history for a typical simulation. 'Full domain' indicates the rms residual in the entire computation domain, 'afterbody' refers to the rms residual in the afterbody domain and 'wake' residual corresponds to the afterbody region of the grid downstream of the separation point.

Fig. 3.6). The surface pressure and heating rate show negligible difference between the results computed on the two grids (see Fig. 3.7).

Based on the foregoing study, the 240×171 baseline grid was finalized and all results using SA model presented below are computed on this grid.

All the grids presented above for the SA model have a wall-normal spacing of 10^{-6} m on the entire vehicle. This is equivalent to y^+ of 0.9 or less along the forebody attached boundary layer and 0.02 or less on afterbody. Further refinement is found to have negligible (less than 0.2%) effect on the heat transfer rate obtained using the SA model.

3.2.2 Iterative Convergence

The flowfield is initialized to freestream values, except for a small region next to the conical afterbody and flat base, where the velocity is set to zero. The advancement of the solution is studied in terms of flow feature development and the corresponding residual history. The rms density residual, normalized by its initial value, is plotted in Fig. 3.8 as a function of the number of time steps. The corresponding physical time, normalized by τ_f, is discussed below.

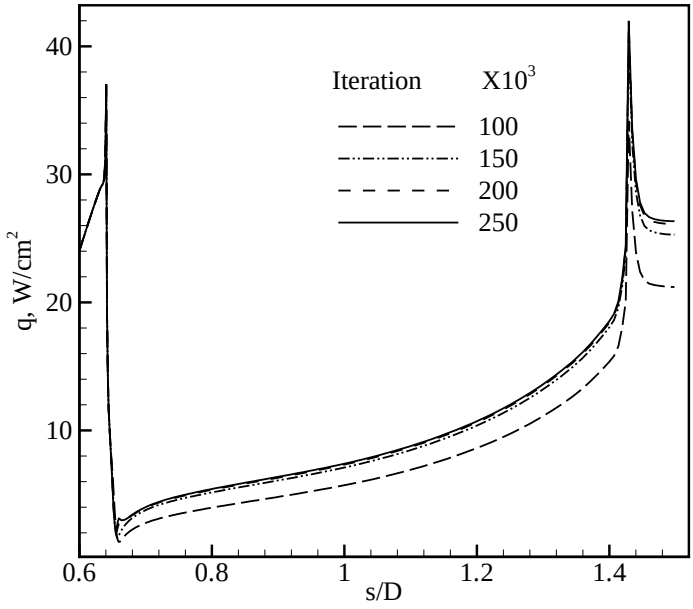

Figure 3.9: Afterbody heat transfer rate after different time steps.

The characteristic flow time τ_f is defined as $\tau_f = D/U_\infty$, and is 1×10^{-4} s for the current configuration.

There is a rapid drop in the residual for the first 20,000 time-steps. This corresponds to the development of the bow shock and the boundary layer on the forebody, and the expansion fans at the shoulder. The flow on the forebody reaches steady state during this period, which corresponds to about 12 τ_f. The separation bubble starts forming at this time and it grows to its full size by about 46 τ_f. The recirculating flow in the near wake shows a very slow convergence to the steady state and it take up to 2×10^5 iterations at a Courant-Friedrichs-Levy (CFL) number of 100 to arrive at the final solution.

Beyond the initial drop, the rms residual continues to fluctuate between 2×10^{-5} and 10^{-4}. These fluctuations correspond to a grid point located along the bow shock near the first expansion corner on the shoulder. This may be caused by a slight mis-alignment of the shock with the grid lines. There is, however, no noticeable change in the shock location or shape at this point, and the large value of the local residual does not appear to affect the rest of the flowfield.

The high local residual value at the bow shock mis-alignment point masks the iterative convergence of the afterbody flowfield after the first 50,000 time steps. A second rms residual is therefore computed in the region downstream of the shoulder, and is referred to as the afterbody

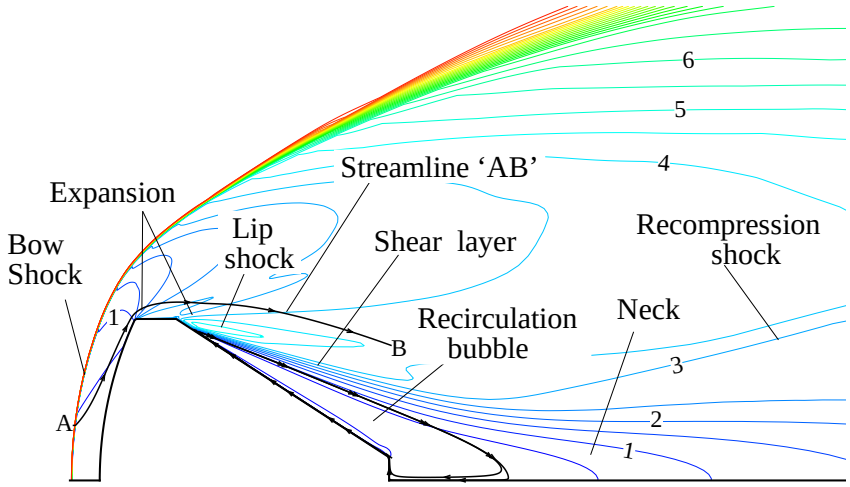

Figure 3.10: Mach number distribution in the turbulent (SA model) flowfield around the FIRE II re-entry capsule at Mach 16 and 35 km altitude. Representative streamlines are shown to identify the recirculation bubble.

residual in Fig. 3.8. Compared to the full-domain residual, the afterbody residual drops to a lower value, but oscillates around 2.5×10^{-7}. The origin of these oscillations is traced to the separation point on the conical frustum. In the vicinity of separation point, all the flow variables are found to fluctuate with very small amplitude (less than 0.05 % of the mean). The location of the separation point is however not altered and therefore these oscillations have negligible effect on the remainder of the flowfield. This can be seen from the residual computed only in the region downstream of the separation point, denoted by the wake residual in Fig. 3.8. This includes majority of the recirculation bubble, the neck region and the far wake. The wake residual shows a steady drop to about 3×10^{-9} after 2.5×10^5 time steps. The iterative convergence of the afterbody heating rate to its steady-state value is shown in Fig. 3.9. There is no noticeable difference between the heat transfer rates obtained after 2×10^5 and 2.5×10^5 time steps, and this is taken as an indicator for terminating the time-iteration process.

Overall, it typically requires computing over 220 τ_f to reach the final steady state solution for the current FIRE II flowfield. For a 240×171 grid, this takes about 230 cpu-hours on a 2.6 GHz Intel processor based machine.

3.3 Results

Figure 3.10 shows the RANS solution computed using the SA turbulence model in terms

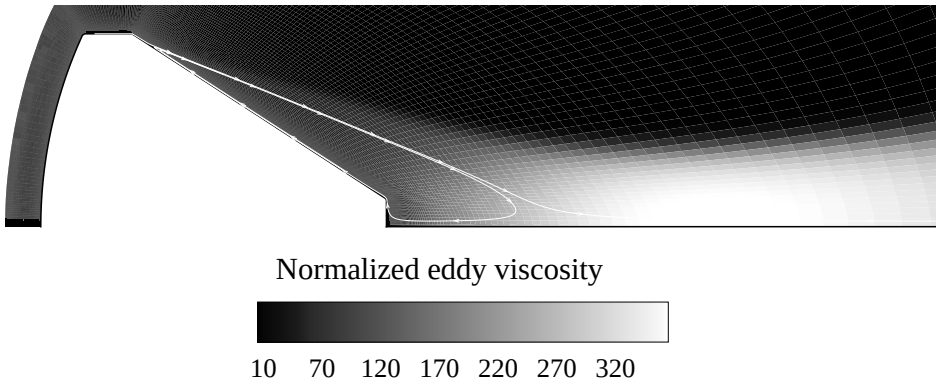

Figure 3.11: Normalized eddy viscosity distribution computed by turbulent (SA model) simulation. Representative streamlines are shown to identify the recirculation bubble.

of the Mach number contours. The prominent features like bow shock and flow expansion at the corners can be easily identified. The flow on the entire forebody is subsonic with Mach number approaching unity close to the first expansion corner. The boundary layer remains attached through the two successive expansions, and separates downstream of the second corner. Flow separation on the conical frustum is found to generate a mild lip shock. The recirculation bubble on the afterbody is characterized by a single toroidal vortex that extends up to about 0.36 diameter downstream of the base. The shear layer enclosing the recirculation region coalesce at the neck and a recompression shock wave is generated. The flow is subsonic in the recirculation bubble, and it expands to supersonic Mach numbers downstream of the neck.

The post-shock temperature in the fore stagnation region is about 5700 K and it varies less than 5% on the forebody. At this temperature oxygen is completely dissociated, whereas nitrogen is mostly in its molecular form. There is a small amount of NO formed in this region. Isothermal condition drops the temperature to 553.3 K at the wall causing recombination of oxygen atoms in the boundary layer. Rapid drop in fluid density associated with the expansion process leads to a frozen thermo-chemical state of the gas. The gas composition on the afterbody is approximately same as that in the forebody inviscid region.

Figure 3.11 shows the distribution of eddy viscosity normalized by the local molecular viscosity. This ratio quantifies the effect of turbulence at each point in the domain. Eddy viscosity is negligible compared to molecular viscosity in the nose stagnation region. The boundary layer is initially laminar, and it becomes transitional with $\mu_T/\mu \simeq 5$ just upstream of the first corner. Strong flow expansion at the shoulder relaminarizes the boundary layer.

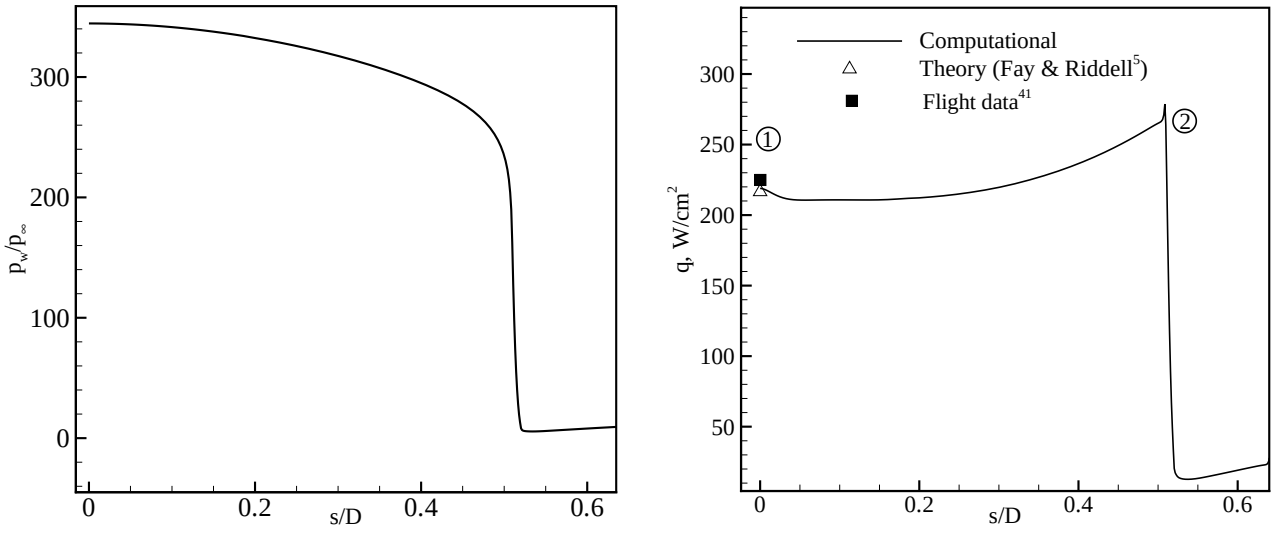

(a) (b)

Figure 3.12: Surface properties obtained using the SA turbulence model on the forebody: (a) normalized pressure, and (b) heat transfer rate. Geometry points 1 and 2 are identified in Fig. 3.1(c).

Subsequently, there is a build-up of turbulence in the shear layer. $\mu_T \geq 20\mu$ in the recirculation region, and its value increases through the neck up to about 360μ in the wake.

3.3.1 Description of the Surface Properties

Figure 3.12 presents the computed surface properties on forebody of the vehicle. The wall pressure follows a parabolic profile with maximum at nose stagnation point ($s/D = 0$) and a rapid drop due to expansion at the shoulder ($s/D = 0.52$). Heat transfer rate varies gradually on the forebody with a maximum value of 219 $\mathrm{W/cm^2}$ at the nose. The stagnation point heating rate matches well with the theoretical estimate of Fay and Riddell [5] and flight data [41] (shown by symbols in Fig. 3.12(b)). At the expansion corner the heating rate has a local peak followed by a sharp decrease as the gas temperature drops due to flow expansion.

The pressure and heating rate on the afterbody surface are presented in Fig. 3.13. The vertical scales are magnified as compared to Fig. 3.12 to highlight the low afterbody levels. The extent of the conical frustum and flat base are identified in the figure. Flow expansion on to the conical afterbody results in a sharp decrease in pressure at $s/D \simeq 0.65$. A similar pressure drop due to the expansion of the reversed flow at the base corner is observed at $s/D \simeq 1.42$. The pressure at the base stagnation point is about 7.23 p_∞, which is about 2% of the nose stagnation

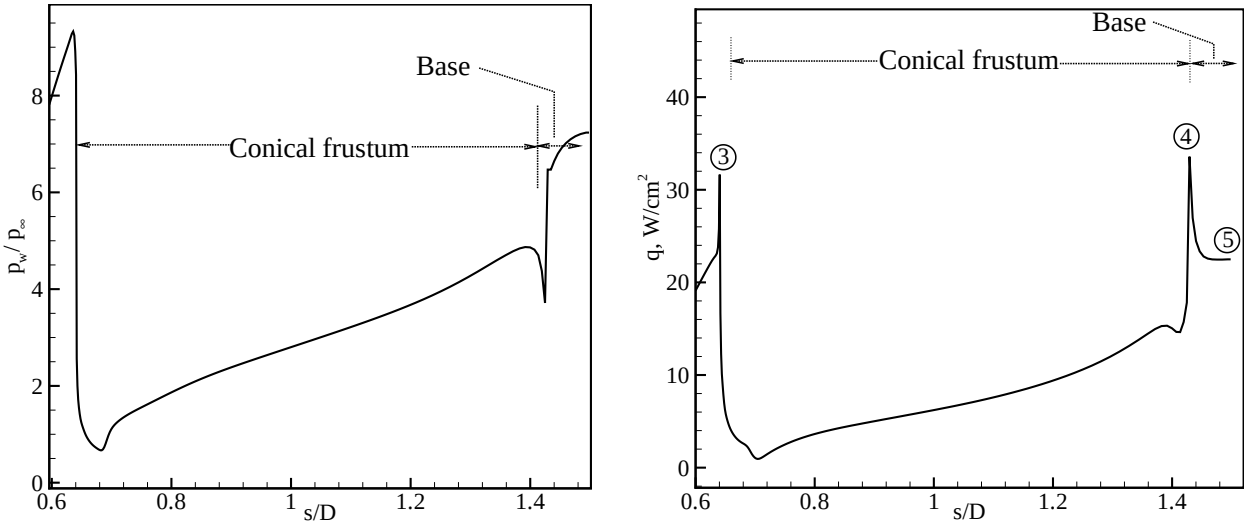

Figure 3.13: Surface properties obtained using the SA turbulence model on the afterbody: (a) normalized pressure, and (b) heat transfer rate. Geometry points 3, 4 and 5 are identified in Fig. 3.1(c).

point value. The expansion corners are also marked by local peaks in the heat transfer rate. In between the two expansion corners, the afterbody pressure and heating rate show a monotonic increase from the separation point at the shoulder to the base corner. The base stagnation point heating rate is 22.48 $\mathrm{W/cm^2}$, which is 10.3% of the corresponding nose stagnation point value.

The afterbody heating rate predicted by the SA model is found to exhibit small waviness along the conical frustum. This waviness occurs when the value of the damping function f_w in the eddy viscosity equation drops below zero. The model equation with the damping function limited to non-negative values results in a smooth variation of the afterbody heating rate, which is shown in Fig. 3.13(b). This modification to the SA turbulence model does not affect any other part of the flow solution.

3.3.2 Effect of Geometric Simplifications

The FIRE II vehicle geometry has ring like structures at the heatshield-aftshell interface and at the base corner. The simplified geometry presented above does not include these details. An updated outer mold line is simulated to study the effect of these additional geometrical features, if any, on the computed flow predictions. The exact dimensions of these ring-like structures could not be found in the literature. Their sizes are approximated from geometry sketches given

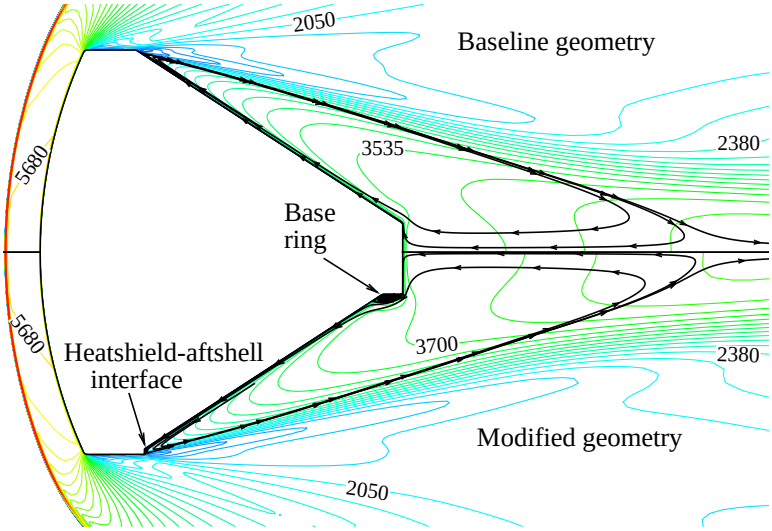

Figure 3.14: Comparison of temperature contours and separation bubble between baseline geometry (top half) and modified geometry (bottom half) using the k-ω model.

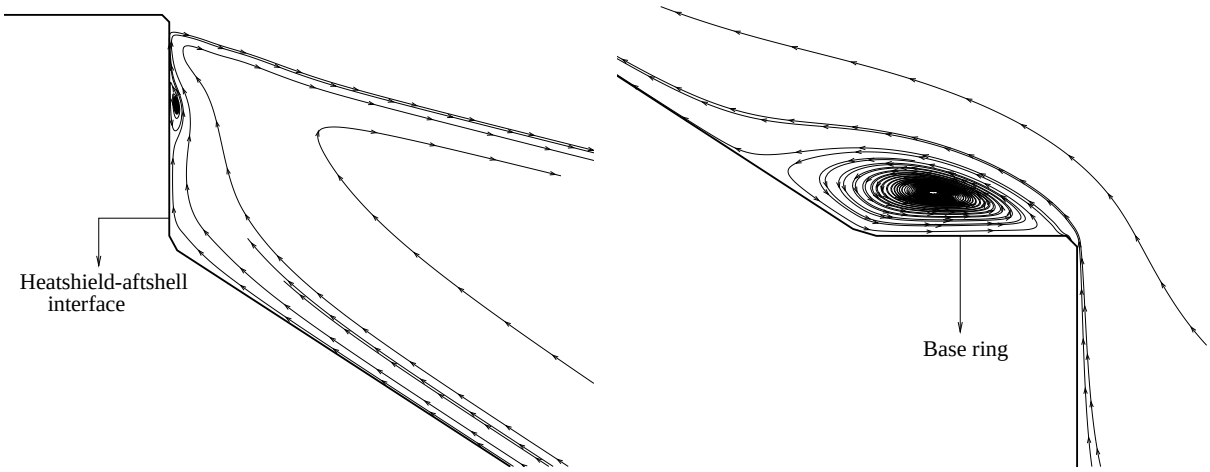

Figure 3.15: Enlarged view of secondary flow separation regions in the flowfield over modified geometry model (a) heatshield-aftshell interface (b) base ring.

in Ref. 41 and they are modeled as finite height steps at the respective locations (see Fig. 3.14).

The finite step at the beginning of the conical afterbody moves the separation point upstream to the corner location. A small secondary vortex (see Fig. 3.15(a)) is formed close to the separation point. Secondary separation is also observed at the base ring (see Fig. 3.15(b)). In spite of these changes, the overall size of the recirculation bubble and the shear layer angle are found to be comparable to the baseline geometry (Fig. 3.14).

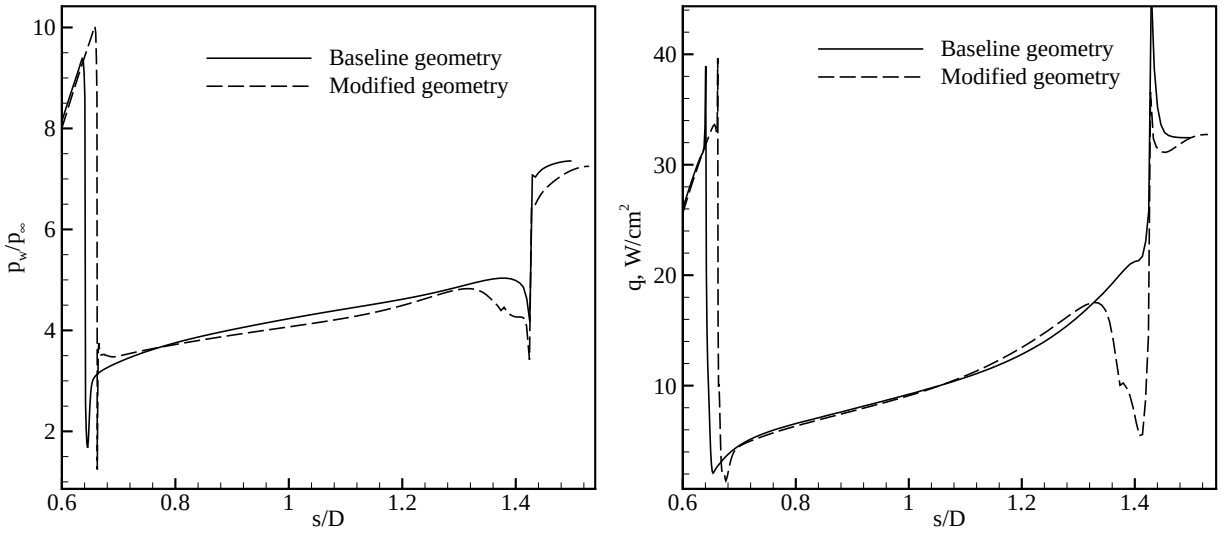

(a) (b)

Figure 3.16: Effect of heatshield-aftshell interface and base ring on surface properties: (a) normalized pressure (b) heat transfer rate.

The surface pressure and heat transfer rates computed using the modified geometry are close to that of the baseline geometry over majority of the conical frustum (Fig. 3.16). The only differences are localized in the regions of geometry variation. The finite step at the heatshield-aftshell interface is found to increase the surface pressure in this region. On the other hand, the secondary vortex at the base corner reduces the surface pressure and heating rate. There is negligible effect of the geometry variations on the heat transfer prediction in the range $0.7 < s/D < 1.3$, where comparison is made with the in-flight measurements.

3.3.3 Comparison with Flight Data

The pressure and heating rate measured during flight are compared to the different computational results in Fig. 3.17. Pressure is measured at $s/D = 1.27$ and surface heating values are available at $s/D = 0.77,\ 0.96,\ 1.13$ and 1.27. For a fixed axial station, there is little variation between the heating data at different circumferential locations. Therefore the heat transfer rates along the three circumferential rays ($\phi = 0^o,\ 120^o$ and 240^o) are not distinguished in Fig. 3.17(b).

Experimental measurements in turbulent base flow yield uniform pressure in the separation bubble [43]. This may be because of the unsteady turbulent mixing in the core flow that helps in equalizing the pressure on the base, and thus yield a uniform surface pressure in the time-

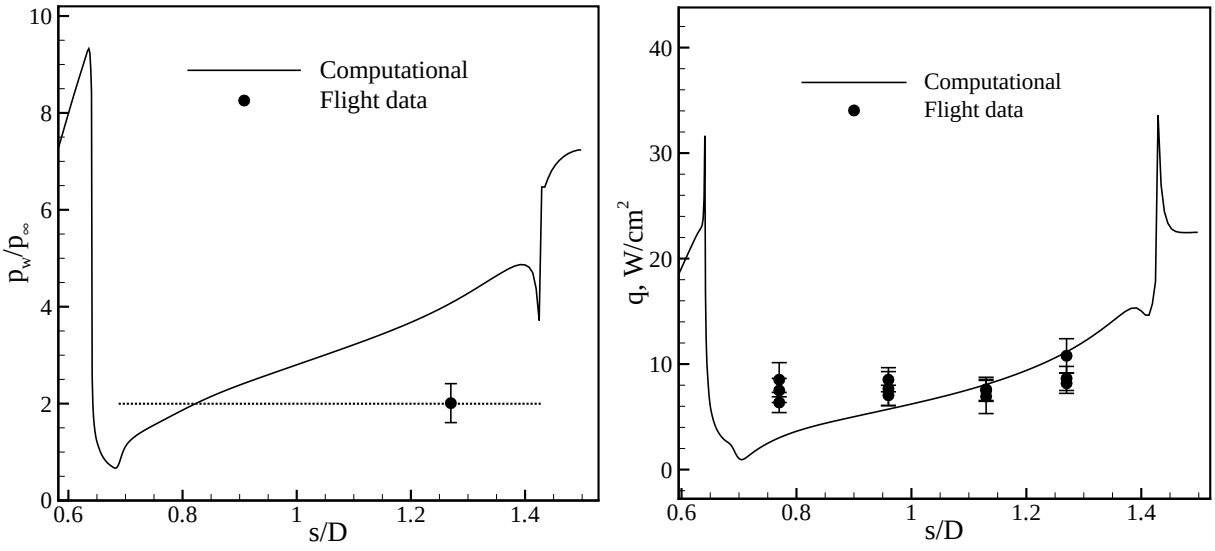

Figure 3.17: Comparison of computed afterbody (a) surface pressure and (b) heat transfer rate with in-flight measurements [36] for flow over FIRE II capsule at 35 km altitude.

averaged solution. Similar trend is expected to be valid in the turbulent recirculation bubble at the current conditions, and therefore the single pressure data point is taken as representative of the entire conical frustum. This is indicated by the dotted line in Fig. 3.17(a). The in-flight measurement is lower than the CFD prediction.

There is large scatter in the pressure measurement between the range 1651.75 to 1655.75 sec which brackets the current trajectory point. This is because the afterbody pressure levels during this period are close to upper operating limit of the pressure sensing system. The actual afterbody pressure may therefore be higher than the value reported in Ref. 36. A higher in-flight pressure level is expected to improve the comparison between computation and measurement.

Comparison of the computed heating rate with the flight data is presented in Fig. 3.17(b). The predicted heating rate is lower than measurement at the beginning of the recirculation bubble. Due to monotonic increase, the computed heat flux exceeds the flight data in the later part of the conical frustum. The predicted heat flux at $s/D = 0.96,\ 1.13$ and 1.27 is within the flight measurement uncertainty. Overall, the computed heat flux compares well with the flight data.

3.4 Summary

Hypersonic turbulent flow around the FIRE II re-entry module at 35 km altitude condition is computed using Reynolds-averaged Navier Stokes method. Five species air chemistry and a two-temperature vibrational relaxation model is used in the simulations. Turbulence closure is achieved using the one-equation Spalart-Allmaras (SA) model. Effects of geometric simplifications made in approximating the outer mold line of the capsule are studied. The computations found to predict the in-flight heating rate measurements at the nose stagnation point and on the conical frustum reasonably well. The in-flight measurement of pressure is higher than that of the computed values.

Chapter 4

Heating Rate Variations at 35 km Altitude

In this Chapter effects of chemical reaction rates on aero-heating predictions have been investigated. Numerical simulations are performed by varying the reaction rate constants on the FIRE capsule at the freestream conditions corresponding to the 35 km trajectory point. CFD solutions obtained by altering the rate constants are carefully analyzed to understand the physical effects that influence the surface heat transfer rate. Initially, the flowfield solutions are computed by varying the rate constants only in the boundary layer. Subsequently, simulations are performed by varying the rate constants in the entire domain. This enables us to isolate the effects of shock layer chemistry from those of the boundary layer chemistry on the flowfield and surface properties.

4.1 Simulation Methodology

The re-entry flowfield at 35 km altitude is simulated by solving the Reynolds-averaged Navier-Stokes (RANS) equations along with a finite rate chemistry model and the procedure is identical to that presented in Sec. 3.2. A separate grid convergence study has not been performed as the test case chosen is same as that presented in Chapter 3. Therefore, 240×171 is used for the altered reactivity simulations (see Sec. 3.2.1). The procedure for altered reactivity simulations is explained below.

4.1.1 Chemical Reaction Kinetics

The rates of chemical reactions are function of concentrations of participating species, temperature and rate constants. The details are given in Sec. 2.1.4 and are repeated below. The rate

constants k_b and k_f are given by

$$k_{f_n}(T_a) = C_{fn} T_a^{\eta_n} \exp\left(\theta_{dn}/T_a\right) \qquad (n = 1, ..., 5) \tag{4.1}$$

where $C_{fn},\ \eta_n$ and θ_{dn} are experimentally determined curve fit data for the n^{th} reaction over a given temperature range. T_a is the effective temperature and for dissociation reactions ($n = 1,\ 2,\ 3$) it is taken as the geometric average of the translational-rotational and vibrational temperature $i.e.\ T_a = \sqrt{TT_v}$. For exchange reactions $T_a = T$. The backward reaction rate constant is obtained using the principle of detailed balance

$$k_{b_n}(T) = \frac{k_{f_n}(T)}{K_{eq,n}} \tag{4.2}$$

where $K_{eq,n}$ is the equilibrium constant given in Ref. 9.

The above set of equations define the chemical kinetics used in the current CFD algorithm. The data presented in Ref. 9 show that the uncertainty in the measurement of rate constants is about one order of magnitude. Hence simulations are performed by increasing and decreasing the chemical reaction rate constants (k_f and k_b) by ten times compared to the baseline values. We change the rate constants for both the forward and backward reactions so that the equilibrium constant remains the same for the given local thermodynamic conditions. Similar procedure is used in Ref. 43. Rate constants are altered for all five reactions simultaneously.

In the CFD algorithm, the reaction rates are altered by multiplying the rate constants by a reaction scaling factor (rsf). The modified forward rate constant at each point is given by rsf$*k_{f_n}$, where k_{f_n} is calculated using Eq. 4.1. The backward reaction rates are also multiplied by the same factor. Hence a value of rsf=10 corresponds to the higher reactivity case, where reaction rate constants are increased by ten times. On the other hand, rsf=0.1 represents lower reactivity case where reaction rate constants are decreased by ten times, and rsf=1 indicates baseline simulation. Note that the chemical source terms in all the simulations are evaluated using mean flow properties, such that the effect of turbulent fluctuations on the reaction rates is neglected. The interaction of turbulence and chemistry can lead to additional variation in the reaction rates, which is beyond the scope of the present paper.

The surface heat transfer rate is directly influenced by the gas composition and temperature in the thermal boundary layer adjacent to the wall. The gas properties in this region are primarily determined by the exothermic recombination reactions caused by the isothermal cold wall condition. The thermo-chemical reactions at the shock wave and in the inviscid post-shock

region affects the flow properties at the boundary layer edge. The thermo-chemistry at the shock wave is predominantly endothermic and variation in the corresponding reaction rates can alter the boundary layer edge conditions and therefore the heating rate predictions.

We first study the changes in surface heat flux due to the alteration in reaction rates only in the boundary layer. In the baseline simulation, the maximum boundary layer thickness is found to be 2.6 mm, which corresponds to about 80 wall-normal points in the computational grid. In this region, the reaction rates are altered by setting rsf $\neq$ 1. Outside the boundary layer, a value of rsf = 1 is used, such that the reaction rates match the baseline values. This results in boundary layer edge conditions that are identical to the baseline solution. Variation in fluid properties at the boundary layer edge caused by the thermo-chemistry at the shock wave are subsequently studied by altering the reaction rates uniformly over the entire computational domain. A controlled study of this nature allows us to isolate the physical effects in different parts of the flowfield.

4.2 Results

A brief description of the computed FIRE II re-entry flowfield and surface properties are given below. Next, the details of the thermo-chemical state of the gas and chemical reactions in the boundary layer are presented. The effect of variation in the chemical reaction rates on heating predictions is explained subsequently.

Main features of the flowfield are shown in Fig. 4.1 in terms of the Mach number contours. The prominent features like bow shock and flow expansion at the corners can be easily identified. The flow on the entire forebody is subsonic with Mach number approaching unity close to the first expansion corner. The post-shock temperature in the nose stagnation region is about 5700 K and it varies less than 5% on the forebody. Flow expansion at the first corner results in decrease of temperature to 4100 K. Further expansion around the second corner decreases the temperature to about 1800 K.

The boundary layer remains attached through the two successive expansions, and separates downstream of the second corner. The recirculation bubble on the afterbody is characterized by a single toroidal vortex that extends up to about 0.36 diameter downstream of the base. Flow in the separation bubble is subsonic with vortex core temperature of about 4000 K. The shear layer enclosing the recirculation region coalesce at the neck, and a recompression shock wave

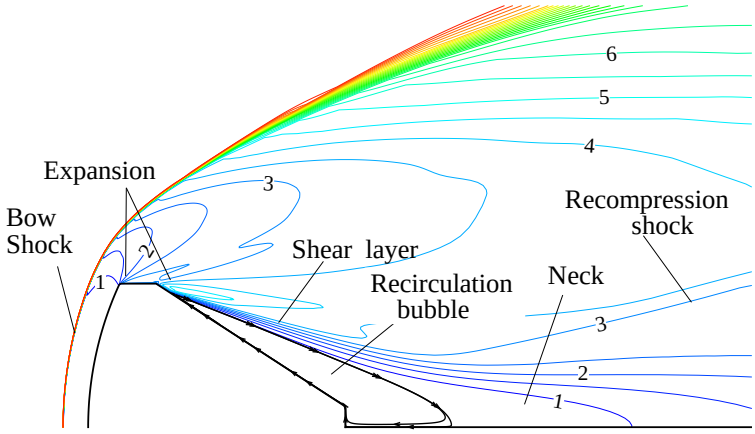

Figure 4.1: Mach number distribution in the flow around FIRE II re-entry capsule at Mach 16. Representative streamlines are shown on the afterbody to identify the recirculation bubble.

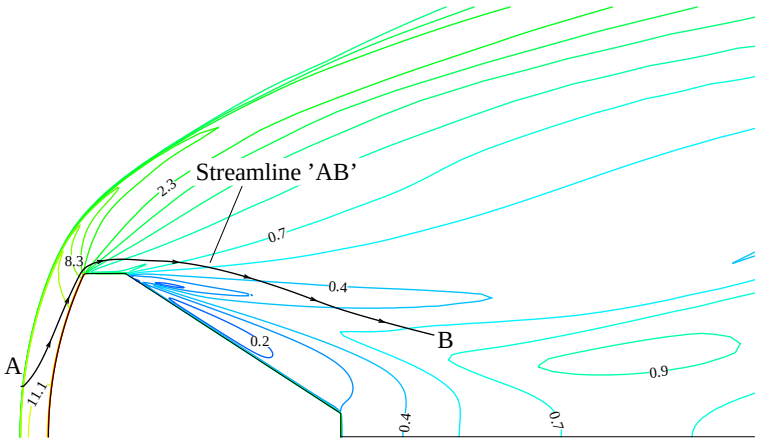

Figure 4.2: Distribution of the gas density, normalized by freestream density, in flow around FIRE II re-entry capsule.

is formed. The temperature of the gas in the neck region is close to 4900 K. The temperature in the inviscid region outside the wake is about 2000 K and the Mach number there is about 3.5.

Figure 4.2 shows normalized density distribution in the flowfield. Density of the gas increases across the bow shock to 11 times the freestream density in the nose stagnation region. Rapid expansion at the shoulder reduces the density of the mixture to 0.2–0.4 ρ_∞ on the afterbody. At the boundary layer (not visible on the scale of Fig. 4.2) gas temperature decreases to the cold wall value, which increases the mixture density to about $100\rho_\infty$ at the wall. The density of the gas in the afterbody near-wall region is about $2\rho_\infty$. Overall the density of the gas changes by three orders of magnitude in the computational domain, and it determines the

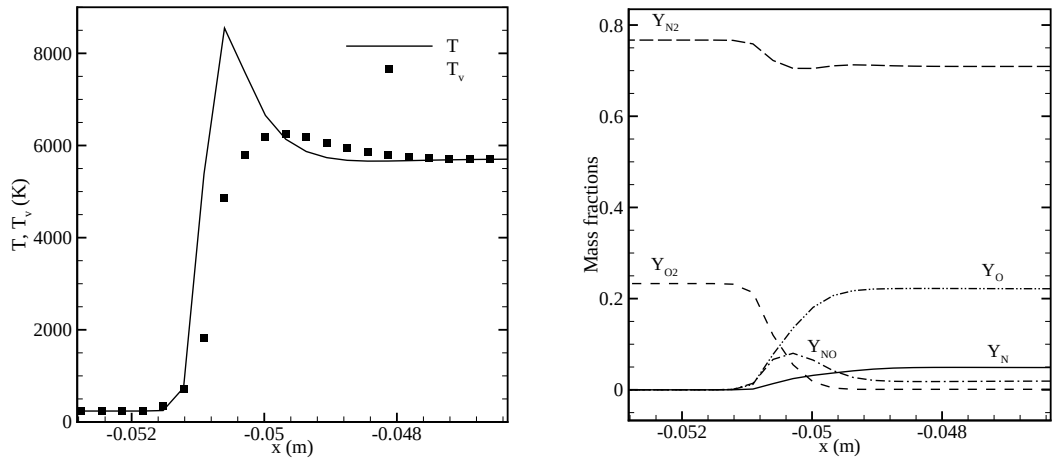

(a) (b)

Figure 4.3: Gas properties at the shock wave along the stagnation streamline: (a) translational-rotational and vibrational temperatures and, (b) species mass fractions.

degree of thermo-chemical activity in the different parts of the flowfield. The thermo-chemical state of the gas has an important influence on the surface heating rate as explained below.

The variation in the gas temperatures and composition at the shock wave are shown in Fig. 4.3. The data is plotted along the stagnation stream line such that the flow is in the positive x-direction and the nose stagnation point is at x=0. The translational-rotational temperature peaks at about 8500 K immediately downstream of the shock wave, followed by rapid decrease due to transfer of translational energy into vibrational and chemical energies. The vibrational temperature shows a gradual rise to about 6200 K. As the chemical reactions progress, there is a drain of translational and vibrational energies. This results in decrease of both temperatures to a equilibrium value of 5700 K in the post-shock region.

Oxygen molecules are mostly dissociated in the post-shock region with an atomic oxygen mass fraction of 0.22. NO is formed behind the shock to a maximum level of 8%. It decreases to 2% in the post-shock region. The exchange reactions result in an increase of Y_{N} up to 0.05 and decrease of $Y_{\mathrm{N_2}}$ to 0.71. The gas composition in the majority of the forebody inviscid region is close to the post-shock values in Fig. 4.3(b). The flow expansion at the shoulder results in a slight increase in $Y_{\mathrm{N_2}}$ and Y_O with a corresponding decrease in Y_{N} and Y_{NO}. The gas composition in the afterbody inviscid expansion region is primarily composed of N_2 and O with mass fraction of 0.75 and 0.23 respectively. Minor changes in the mass fraction of N_2, N

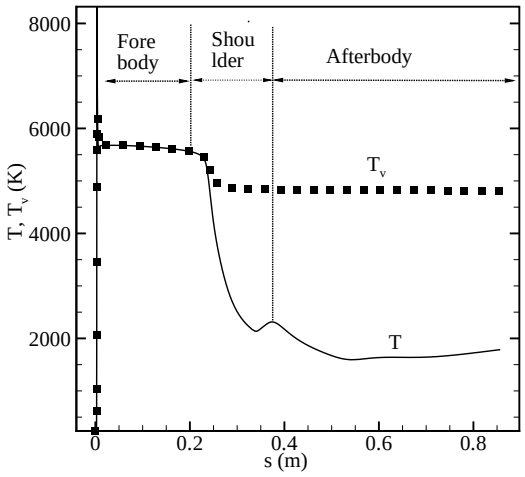

Figure 4.4: Translational-rotational and vibrational temperatures of the gas along a streamline (identified as streamline 'AB' in Fig. 4.2) that passes through the bow shock wave, forebody and afterbody inviscid regions.

and NO are observed in the separation bubble due to chemical reactions in the hot vortex core.

The thermal state of the gas in the flowfield is explained with the aid of Fig. 4.4, which plots the translational-rotational and vibrational temperatures along a stream line (identified as streamline 'AB' in Fig. 4.2) passing through the bow shock and the inviscid regions on the fore-body, shoulder and afterbody. The two temperatures are identical in the post-shock region on the forebody. A high fluid density in this region equilibrates both the translational and vibrational temperatures leading to a thermal equilibrium state. As the gas expands around the shoulder, a low density in the afterbody flowfield freezes the energy exchange between the translational and vibrational modes, resulting in a thermally frozen state on the afterbody. The vibrational temperature freezes at about 5000 K, whereas the translational-rotational temperature drops to values lower than 2000 K. The transition between the thermal equilibrium on forebody and frozen state on afterbody occurs through a thermal non-equilibrium state in the shoulder region. Chemical state of the gas follows a trend similar to that of the thermal state. The gas approaches a chemical equilibrium state in the nose stagnation region with a non-equilibrium state on the shoulder. The chemistry is in a frozen state in the afterbody region.

Figure 4.5(a) shows the variation of the two temperatures in the thermal boundary layer at the nose stagnation point. Local boundary layer thickness is used to non-dimensionalize the wall normal distance, such that $l/\delta = 0$ represents the wall location and $l/\delta = 1$ corresponds to the thermal boundary layer edge. Both the translational-rotational and vibrational temperatures

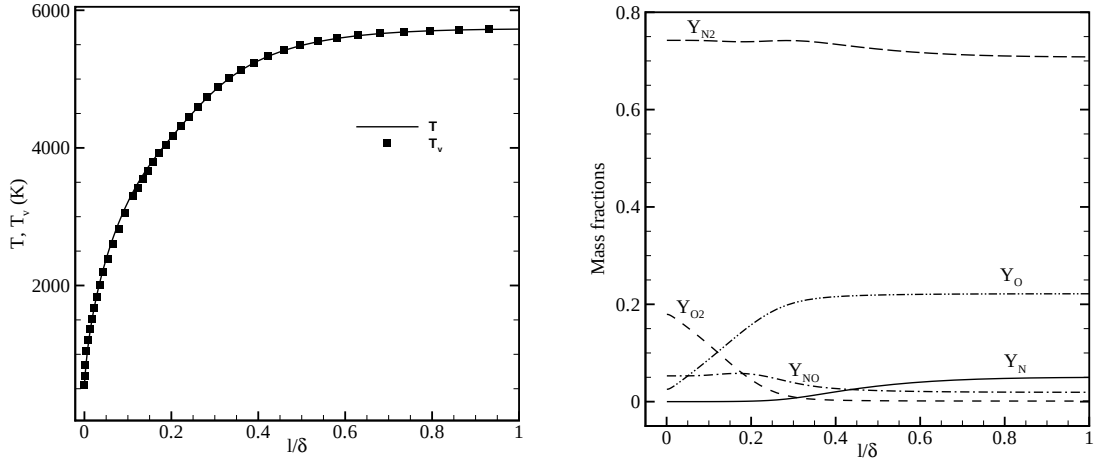

(a) (b)

Figure 4.5: Boundary layer profiles of (a) translational-rotational and vibrational temperatures and (b) species mass fractions at the nose stagnation point.

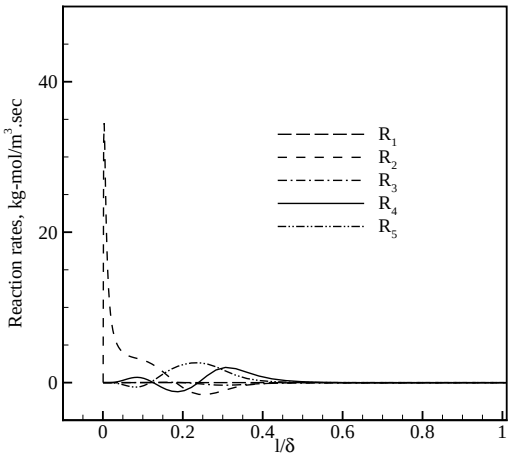

Figure 4.6: Rates of the different chemical reactions occurring in the thermal boundary layer at the nose stagnation point.

of the gas decrease from 5700 K in the outer inviscid flow to 553.3 K at the isothermal wall. In the boundary layer mass fraction of atomic species $i.e.$ O and N decrease, and a corresponding increase in mass fractions of O_2 and N_2 can be noticed in Fig. 4.5(b). $Y_{\rm NO}$ also increases from 0.02 at edge of boundary layer to 0.05 at wall.

Figure 4.6 depicts the rate of the different chemical reactions in the boundary layer. In the immediate vicinity of the wall, recombination of O is predominant and this leads to an increase in $Y_{\rm O_2}$. The rate of the exchange reactions (R_4 and R_5) have non-negligible values for $0.2 < l/\delta < 0.4$ and they increase the mass fractions of N_2 and NO with a corresponding decrease in

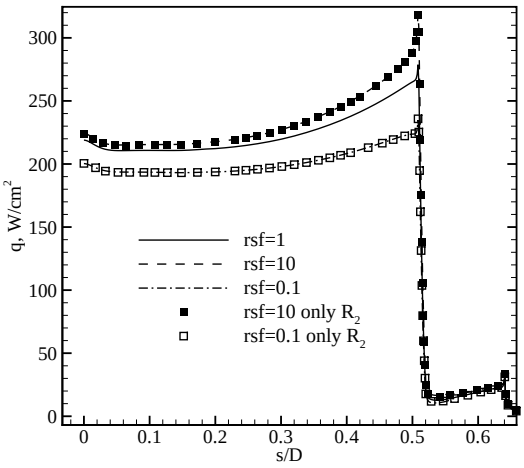

Figure 4.7: Effect of variation in reaction rates on the forebody surface heat flux.

Y_{N}. However these changes are smaller compared to the changes in oxygen mass fractions. In the outer portion of the boundary layer ($l/\delta > 0.5$), the reaction rates are approximately zero.

4.2.1 Effect of Reaction Rates Variation on the Heating rate

Figure 4.7 compares the forebody heat transfer rate obtained by varying the reaction rate constants with those of the baseline simulation (rsf=1). Lowering the reaction rates in the boundary layer (rsf=0.1) decreases the heating rate and enhancing the reaction rates (rsf=10) results in an increase in the heat transfer rate. Also, the heating rate obtained by altering only the rate constant of oxygen recombination reaction are identical to that when all the five reactions rates are changed simultaneously. Therefore at the chosen freestream conditions, the surface heating rate is primarily influenced by the rate of oxygen recombination, which is the dominant reaction in the near wall region (see Fig. 4.6).

As noted earlier, the cold wall condition favors recombination reactions in the boundary layer. Increasing the reaction rates therefore enhances the formation of diatomic species. Figure 4.8 shows that in the boundary layer, the mass fraction of oxygen molecules increases for the higher reactivity case compared to the baseline simulation, and vice-versa. The recombination reactions are exothermic, and higher reactivity results in higher heat release. The gas temperature is therefore elevated in the rsf=10 simulation as compared to baseline case. Opposite is true for lower reactivity simulation. This trend is depicted in Fig. 4.9(a) which shows the gas temperature at the first cell next to the wall.

The change in the gas composition due to recombination reactions leads to change in the

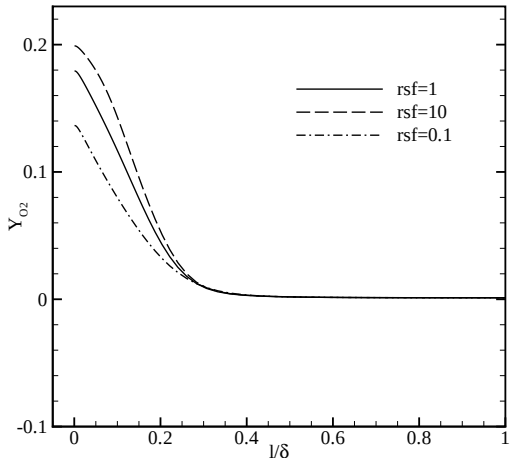

Figure 4.8: Effect of variation in reaction rates on Y_{O_2} in the boundary layer at the nose stagnation point.

mixture conductivity. For the current range of thermodynamic conditions, the relative magnitude of thermal conductivity among the species is

$$\kappa_{\mathrm{N}} > \kappa_{\mathrm{O}_2} > \kappa_{\mathrm{N0}} > \kappa_{\mathrm{N}_2} > \kappa_{\mathrm{O}} \tag{4.3}$$

As molecular oxygen has higher thermal conductivity than its atomic counterpart, the rsf=10 case has higher thermal conductivity of the gas mixture (see Fig. 4.9(b)). An elevated gas temperature and mixture conductivity in the higher reactivity case leads to the higher heating rate. The reverse is true for the lower reactivity simulation.

The heat flux to the wall can be written as

$$q = -\kappa \frac{\partial T}{\partial \eta} = -\kappa \frac{T_2 - T_w}{\triangle \eta} \tag{4.4}$$

where the mixture conductivity is a function of its composition and local thermodynamic condition. The wall-normal temperature gradient is discretized in terms of the gas temperature at the first cell next to the wall, the wall temperature, and the wall-normal distance, $\triangle\eta$. The change in heat flux due to varying reaction rates can therefore be expressed in terms of change in κ and T_2. The quantities T_w and $\triangle\eta$ remain fixed in all the three simulations.

$$\frac{\triangle q}{q} = \frac{\triangle \kappa}{\kappa} + \frac{\triangle T_2}{T_2 - T_w} \tag{4.5}$$

where higher-order terms are neglected. A quantitative analysis of the changes in heat transfer flux due to the varying reaction rates at different locations on the body is given below.

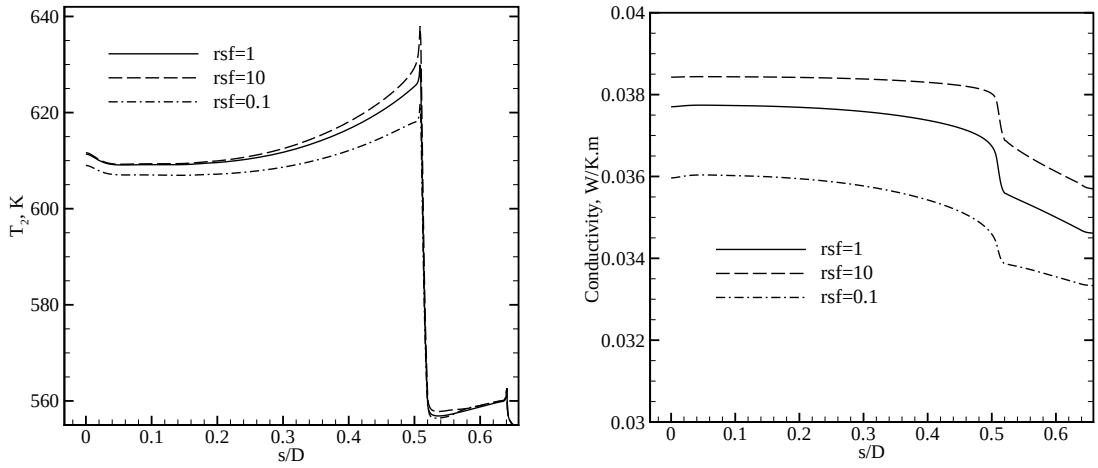

(a) (b)

Figure 4.9: Changes in (a) T_2, and (b) mixture conductivity on forebody due to variation in reaction rates.

4.2.2 Nose Stagnation Point

Table 4.1 shows a budget of Eq. 4.5 at the nose stagnation point for the higher and lower reactivity cases, where the changes are calculated with respect to the baseline solution. The positive values listed for rsf=10 represent increase in the mixture conductivity and the gas temperature. The negative values, on the other hand, correspond to a reduction in the respective values when the reaction rate constants are decreased. The heating rate is enhanced by 2.4% for rsf=10 and reduced by 8.5% for rsf=0.1. Note that the stagnation point heating rate is more sensitive to lowering the reaction rates than to increasing the reactivity. A similar trend in heat transfer rate variations is seen all along the forebody boundary layer (see Fig. 4.7). The reason for this trend in heating rate can be explained in terms of the chemical state of the gas (equilibrium, non-equilibrium or frozen) and the extent of the recombination reactions.

In the forebody shock layer, the gas is in chemical equilibrium, $i.e.$ as $T \rightarrow T_w$, the gas composition approaches its equilibrium value given by the local thermodynamic conditions. Hence increasing the reaction rates does not alter the gas composition significantly. In the baseline simulations, majority of the atomic species recombine to form diatomic molecules. At the wall, the mass fraction of O_2 is close to its maximum achievable freestream value. Hence enhancing the recombination reactions further increases O_2 mass fraction by a small amount (0.02) (see Fig. 4.8), which has minimal effect on the heating rate. When reaction rates are decreased, recombination reactions are suppressed and it leads to an appreciable change in O_2

Table 4.1: Contribution of $\triangle\kappa/\kappa$ and $\triangle T_2/(T_2 - T_w)$ to $\triangle q/q$ at the nose stagnation point.

% change	rsf=10	rsf=0.1
$\triangle\kappa/\kappa$	1.91	-4.61
$\triangle T_2/(T_2 - T_w)$	0.48	-4.08
$\triangle q/q$	2.40	-8.50

concentration in the boundary layer compared to the baseline solution. The heating rate is therefore altered significantly for lower reactivity case.

4.2.3 Expansion Region

Figure 4.7 shows that the variations in surface heating rate due to the alterations in reaction rate constants increases as we go from the stagnation point (s/D=0) to the shoulder (s/D=0.51). Similar trends can be observed in T_2 and κ in Fig. 4.9. This is because of flow expansion along the forebody, which is characterized by a decrease in pressure, temperature and density with increasing distance from the stagnation point.

As the density decreases from the stagnation region to the shoulder, the reactions get slower and the chemical state of the gas changes from equilibrium to non-equilibrium. The gas composition does not approach equilibrium values corresponding to local thermodynamic condition at the cold wall temperature, and an appreciable fraction of the gas is in its atomic state. The extent of recombination is lower than that at the nose stagnation point and the mass fraction of O_2 molecules is not recovered to its freestream value. For example, at $s/D = 0.52$ located at the first expansion corner Y_{O_2} reaches a value of 0.13 at the wall, as compared to a maximum possible value of 0.22 (see Fig. 4.10).

Increasing the reaction rate constants (rsf=10) takes the gas closer to the chemical equilibrium state. It increases the extent of recombination (see Fig.4.10) appreciably, which in turn results in an appreciable increase in the mixture conductivity and the gas temperature. Table 4.2 shows the contribution of $\Delta\kappa$ and ΔT_2 to the overall heating rate enhancement at the expansion corner. Increased mixture conductivity (due to the additional O_2 recombination), and increased gas temperature (due to the exothermic reactions) result in a 16.8% enhancement in the surface heating rate. Decreasing the reaction rate constants (rsf=0.1) has the opposite effect. It results

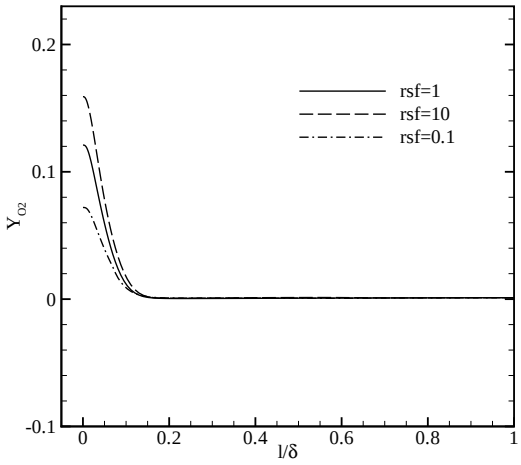

Figure 4.10: Change in Y_{O_2} in the boundary layer at $s/D = 0.52$ (first expansion corner) due to variations in reaction rates.

Table 4.2: Contribution of $\triangle\kappa/\kappa$ and $\triangle T_2/(T_2 - T_w)$ to $\triangle q/q$ in the shoulder expansion corner (s/D=0.52).

% change	rsf=10	rsf=0.1
$\triangle\kappa/\kappa$	3.92	-5.55
$\triangle T_2/(T_2 - T_w)$	12.38	-10.22
$\triangle q$	16.80	-15.20

in a significant decrease in O_2 mass fraction. The corresponding changes in $\Delta\kappa$ and ΔT_2 are listed in Table 4.2 and they add up to a 15.2% decrease in the surface heating rate.

4.2.4 Afterbody

The changes in surface heat flux along the afterbody frustum and base due to changes in the reaction rate constants are shown in Fig. 4.11. The change in afterbody heating rate is much less than that observed on the forebody. Increasing the reaction rates results in only two appreciable changes in heat flux distribution. First, there is a rise in the base heating value as compared to the baseline simulation. Second, the location of the separation point (at $s/D \simeq 0.7$) changes, resulting in a corresponding variation in heating rate in this region. We study the flow solution at the base stagnation point ($s/D = 1.5$) in detail.

The lower changes in the afterbody heat flux to the variation in reaction rates is due to

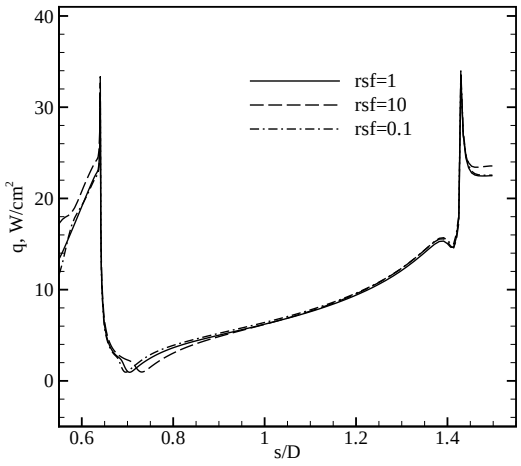

Figure 4.11: Effect of variation in reaction rates on the afterbody heating rate.

Table 4.3: Contribution of $\triangle\kappa/\kappa$ and $\triangle T_2/(T_2 - T_w)$ to $\triangle q/q$ at base stagnation point ($s/D = 1.5$).

% change	rsf=10	rsf=0.1
$\triangle\kappa/\kappa$	2.38	-1.46
$\triangle T_2/(T_2 - T_w)$	2.32	1.77
$\triangle q$	4.76	0.27

a frozen chemical state of the gas in this region. This inhibits recombination reactions in the boundary layer as evident in Fig. 4.12(a). Oxygen is mostly in its atomic form in the baseline (rsf=1) simulation, with $Y_{O_2} = 0.02$ at the wall. Y_{O_2} increases to 0.05 for rsf=10, and decreases below 0.01 for rsf=0.1. Unlike the forebody and shoulder boundary layers, the changes in Y_{O_2} observed in Fig. 4.12(a) are not entirely because of variation in reaction rate constants in the near-wall region. There is a noticeable difference between the Y_{O_2} values computed at the edge of the boundary layer in the three simulations. The reason for this is explained below.

The gas that is trapped in the recirculation bubble originates from the forebody boundary layer. Changes in the gas composition in the forebody boundary layer caused by the variation in reaction rates is convected into the vortex core and free shear layer on the afterbody. This results in an appreciable variation in Y_{O_2} at the boundary layer edge between the three simulations. Changes in the mixture composition at the boundary layer edge and increased reactivity in the boundary layer lead to an increase in the mixture conductivity by about 2.4% in the

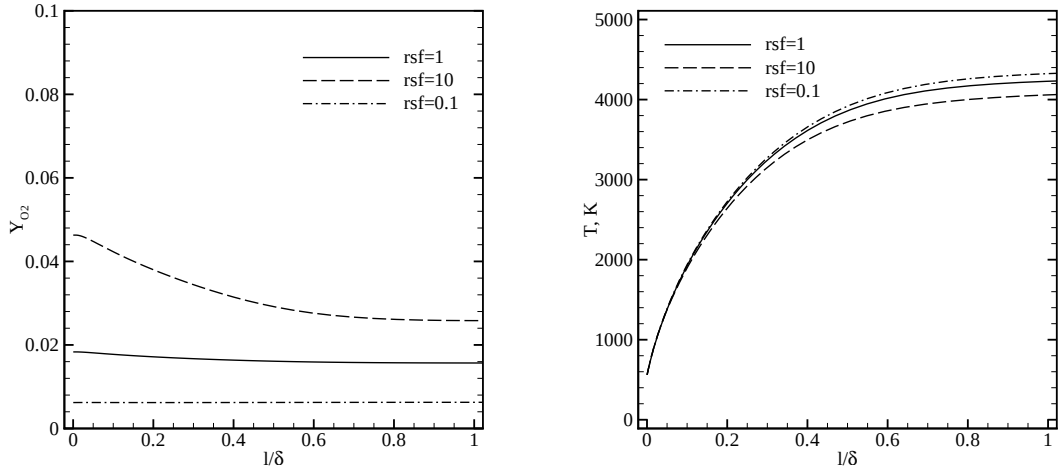

(a) (b)

Figure 4.12: Profiles of (a) Y_{O_2} and (b) temperature in the thermal boundary layer at the base stagnation point.

rsf=10 simulation. The conductivity decreases by about 1.5% in the lower reactivity case (see Table 4.3).

Similar to the mixture conductivity, the gas temperature adjacent to the wall is also determined by a combination of the boundary layer edge effect and the changes caused by altering the reaction rates in the near-wall region. Figure 4.12(b) shows that the boundary layer edge temperature is lower for rsf=10 compared to the baseline simulation and it counteracts the increase in T_2 due to enhanced exothermic reactions in the boundary layer. The opposite is true for rsf=0.1 solution. The net effect is an increase in T_2 by 2.3% in the higher reactivity case and an increase of 1.8% in the lower reactivity simulation (see Table 4.3). For rsf=10 case, changes in gas temperature add to the changes in the mixture conductivity leading to a 4.8% increase in the base heating rate. On the other hand, changes in κ and T_2 due to reduced reaction rates cancel each other to yield a negligible effect on the base heating rate for rsf=0.1.

4.2.5 Increased Reactivity in the Entire Domain

Figure 4.13 compares the flowfield solutions obtained from the baseline simulation (top half) and a higher reactivity simulation in which the rate constants are increased (rsf=10) uniformly over the entire computational domain. The shape of the bow shock wave, the shock stand-off distance and the temperature of the gas in the inviscid shock layer are essentially same in the two solutions. However the afterbody flowfield shows some marked changes. In the higher

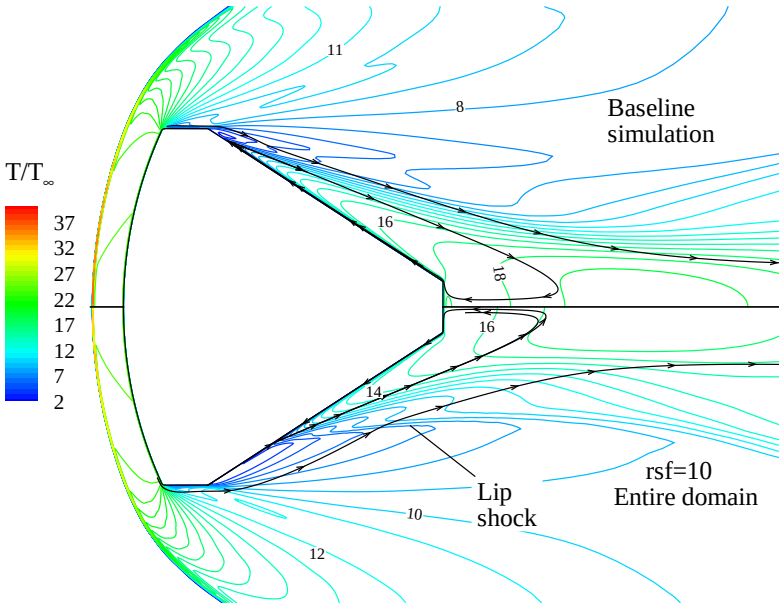

Figure 4.13: Comparison of non-dimensional temperature distribution and separation bubble obtained from the baseline (top half) and higher reactivity (bottom half) simulations. Streamlines are drawn to demarcate the separation point and recirculation bubble size.

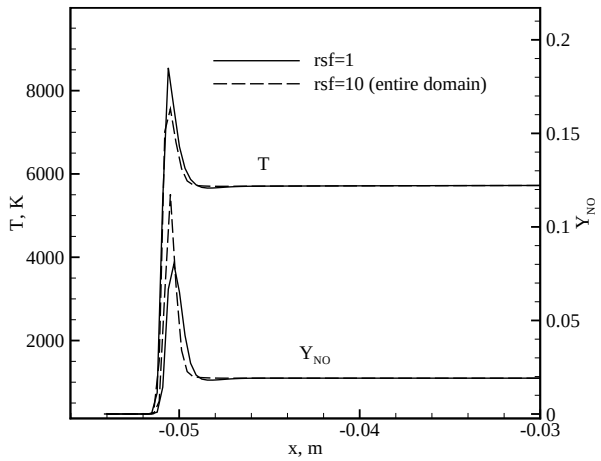

Figure 4.14: Effect of increasing the reaction rates in the entire domain on gas temperature and Y_{NO} along the stagnation streamline.

reactivity simulation, the separation point shifts downstream compared to that of the baseline case, resulting in a significant reduction in the separation bubble size. A lip shock originating at the separation point can be clearly seen in the higher reactivity case, and the shear layer angle is lower by 2.32° as compared to the baseline simulation.

The variation of gas temperature and Y_{NO} along the stagnation stream line is shown in

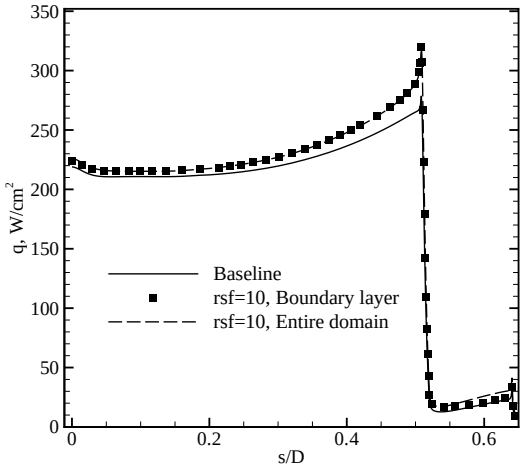

Figure 4.15: Effect of increasing the reaction rates in the entire domain on forebody heating rate.

Fig. 4.14. Increased reactivity (rsf=10) at the shock wave enhances the dissociation of N_2 and O_2, leading to a higher level of NO formation. As the dissociation is an endothermic process, higher dissociation at the shock wave leads to a lower temperature (by about 1000 K) than the baseline solution. Downstream of the shock wave, the two solutions are identical in terms of T and Y_{NO}. This corresponds to the thermo-chemical equilibrium region, where $T = T_v$ and all the species concentrations attain their equilibrium values. This gives identical solution at the boundary layer edge in the baseline and higher reactivity simulations. Further changes in the thermal boundary layer in the higher reactivity case match those obtained (see Fig. 4.8) when the reaction rates are enhanced only in the near-wall region. This is reflected in the overlapping heat transfer predictions obtained from the two rsf=10 simulations in Fig. 4.15.

The gas approaches thermo-chemical equilibrium in the entire region between the bow shock and the spherical forebody. As a result, the changes in T and Y_{NO} induced by higher reactivity at the shock (see Fig. 4.14) have a negligible effect on the shape and location of the bow shock. Also, the changes at the shock wave have no effect on the surface heating augmentation on the entire forebody, up to the first expansion corner (see Fig. 4.15).

Increasing the reaction rates outside the boundary layer has a much larger effect on the surface heat flux at the shoulder. Flow expansion in this region and the associated temperature drop causes recombination and exchange reactions. The gas is in a state of thermo-chemical non-equilibrium, so that increasing the chemical rate constants results in a higher degree of these reactions. The gas chemistry in this zone is exothermic, and therefore a higher reactivity

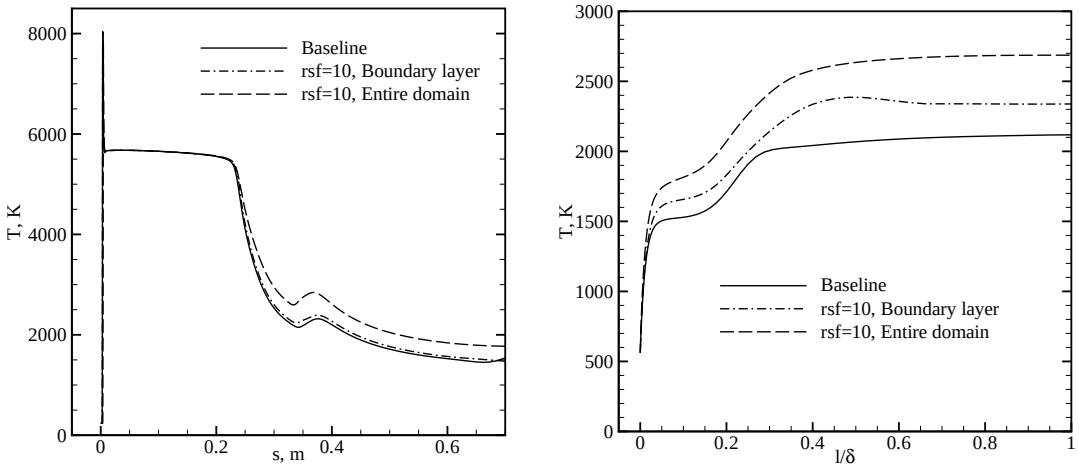

(a) (b)

Figure 4.16: Effect of increasing the reaction rates on gas temperature: (a) along the streamline AB shown in Fig. 4.2, and (b) across the boundary layer at the second expansion corner, $s/D = 0.64$.

results in a hotter gas in the outer inviscid flow than in the baseline simulation. Figure 4.16(a) shows this effect in terms of the temperature distribution along the streamline AB that spans the inviscid region on the forebody, shoulder and afterbody.

An elevated gas temperature in the rsf=10 simulation increases the surface heating rate on the shoulder ($0.54 < s/D < 0.64$), as can be observed in Fig. 4.17(a). The effect is localized in the vicinity of the first expansion corner, when the reaction rates are altered only in the near-wall region. The gas chemistry is frozen in the later part of expansion, leading to heating rates comparable to the baseline predictions. By comparison, when the reaction rates are altered in the entire domain, its effect is carried further by the inviscid flow outside the boundary layer. The resulting increase in gas temperature at the boundary layer edge (see Fig. 4.16(b)) has a major effect. The heating rate in this case is enhanced over the entire shoulder region, up to the second expansion corner. Table 4.4 shows the contribution of $\triangle\kappa$ and $\triangle T_2$ to the heating rate increment at $s/D = 0.64$ obtained from the two higher reactivity simulations. The change in the mixture conductivity is similar in the two cases. The dominant effect is the increase of $\triangle T_2$ when rsf=10 in the entire domain and it raises the surface heat flux by 32%.

The effect of increased reactivity on surface pressure (see Fig. 4.17(b)) is similar to that observed for the heat flux. Compared to the baseline values, the pressure level on the shoulder is elevated when the reaction rates are enhanced by a factor of ten.

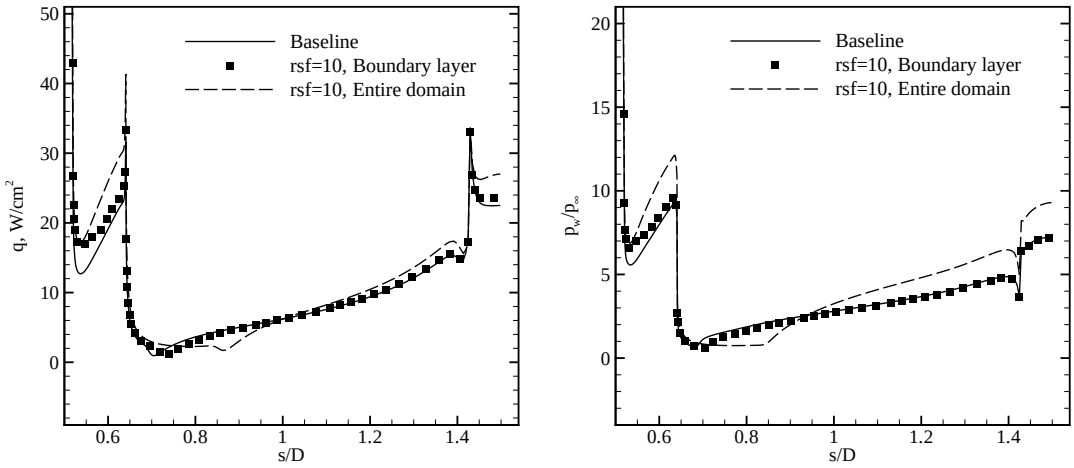

(a) (b)

Figure 4.17: Effect of increasing the reaction rates in the entire domain on afterbody surface properties: (a) heat transfer, and (b) normalized pressure.

Table 4.4: Contribution of $\triangle\kappa/\kappa$ and $\triangle T_2/(T_2 - T_w)$ to $\triangle q/q$ at the second expansion corner ($s/D = 0.64$) in the two higher reactivity simulations.

% Change	Boundary layer	Entire domain
$\triangle\kappa/\kappa$	3.22	3.02
$\triangle T_2/(T_2 - T_w)$	2.37	27.37
$\triangle q$	5.70	32.01

On the conical frustum, heating rates predicted by the three simulations follow the same trend (see Fig. 4.17(a)). There is a rapid drop in heat transfer at the expansion corner, followed by a local minimum at the separation point. The heating rate increases along the separation bubble, with a relatively high value at the base stagnation point. Enhanced reactivity in the entire domain shifts the separation point downstream (also see Fig. 4.13). There is a slight increase in the heat flux on the later part of the conical frustum and a relatively larger increase in the base heating rate compared to the baseline simulation. Similar trends, but smaller in magnitude, are also observed when the reaction rates are altered only in the near-wall region.

The pressure data shown in Fig. 4.17(b) shows a similar pattern. The pressure rise at the separation point is shifted downstream for higher reactivity cases. As expected altering the rate constants only in the near wall region has negligible effect on the pressure distribution. On the

Table 4.5: Contribution of $\triangle\kappa/\kappa$ and $\triangle T_2/(T_2 - T_w)$ to $\triangle q/q$ at the at base stagnation point ($s/D = 1.5$) in the two higher reactivity simulations.

% Change	Boundary layer	Entire domain
$\triangle\kappa/\kappa$	2.38	2.51
$\triangle T_2/(T_2 - T_w)$	2.32	16.89
$\triangle q$	4.76	18.23

other hand, enhanced reactivity in the entire domain changes the size and shape of the separation bubble, resulting in a higher pressure on the afterbody frustum and base.

Note that enhancing the reaction rate constants in the entire domain increases the base heating rate by about 18.2% of the baseline value. Table 4.5 lists the contributions of increased mixture conductivity and gas temperature to the rise in surface heating. The change in mixture conductivity and therefore the extent of recombination in this case are similar in magnitude to that obtained when the chemical rate constants are altered only in the boundary layer. However, the gas temperature in the immediate vicinity of the wall is significantly higher for the case of enhanced reactivity in the entire domain. As discussed earlier (section III. 4.2.4), the gas temperature and the mixture composition at the base stagnation point are determined by a combined effect of their boundary layer edge values and by the extent of exothermic recombination reactions in the boundary layer. The effect of enhanced reactivity in the outer flow on boundary layer edge values is the dominant factor in raising the heating rate. The chemical reactions in the near-wall region has a minor effect on the surface heat flux. This is due to the low density and consequently a frozen thermo-chemical state of the gas in this region.

4.2.6 Decreased Reactivity in the Entire Domain

Figure 4.18 compares of non-dimensional temperature contours and separation bubble streamlines obtained from the baseline case (top half) and the lower reactivity simulation (bottom half) in which rate constants are decreased (rsf=0.1) uniformly in the entire computational domain. In the lower reactivity case, the gas temperature at the bow shock wave is higher, and the shock stand-off distance marginally increases compared to the baseline simulation. Location of the separation point and the shear layer angle are approximately same in both solutions.

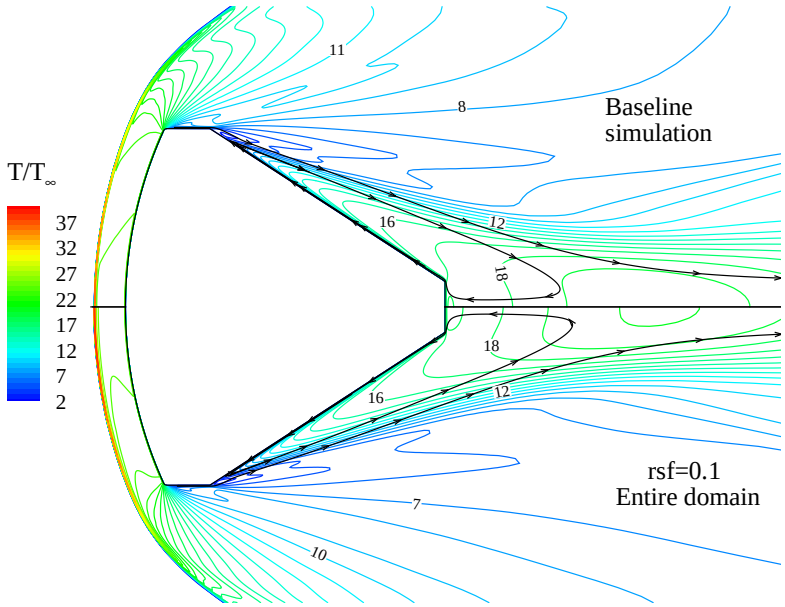

Figure 4.18: Comparison of non-dimensional temperature distribution and separation bubble between the baseline (top half) and lower reactivity (bottom half) simulations.

The separation bubble is, however, slightly larger in the lower reactivity case than the baseline simulation.

The variation of gas temperature and Y_{NO} along the stagnation stream line (Fig. 4.19) shows that the shock wave moves slightly upstream when the reaction rates are reduced. A decrease in reaction rates suppresses the dissociation of N_2 and O_2. This leads to lower level of NO and a higher peak temperature at the shock. The trend is exactly opposite to that observed in the higher reactivity case (cf. Fig. 4.14). A lower reactivity also results in a slower approach to the thermo-chemical equilibrium state downstream of the shock. As expected, the gas properties in the equilibrium region are identical in the two solutions. This results in identical values at the boundary layer edge. Further changes in the thermal boundary layer in the lower reactivity case match those obtained (in Fig. 4.8) when the reaction rates are suppressed only in the near-wall region. The heat transfer rates predicted by the lower reactivity (entire domain) simulation is same as the rsf=0.1 values presented in Fig. 4.7 over majority of the forebody surface and hence not repeated here.

A lower reactivity suppresses the recombination and exchange reactions in the shoulder expansion region. This results in a lower mass fraction of the molecular species and a lower gas temperature. Both lead to a reduction in surface heat flux (see Fig. 4.20(a)) on the shoulder, as

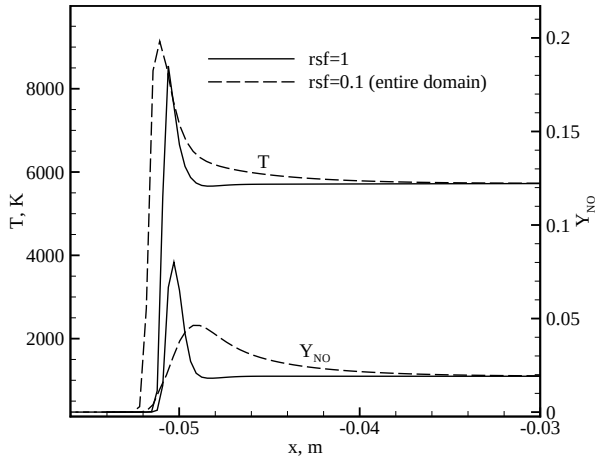

Figure 4.19: Effect of decreasing the reaction rates in the entire domain on gas temperature and Y_{NO} along the stagnation streamline.

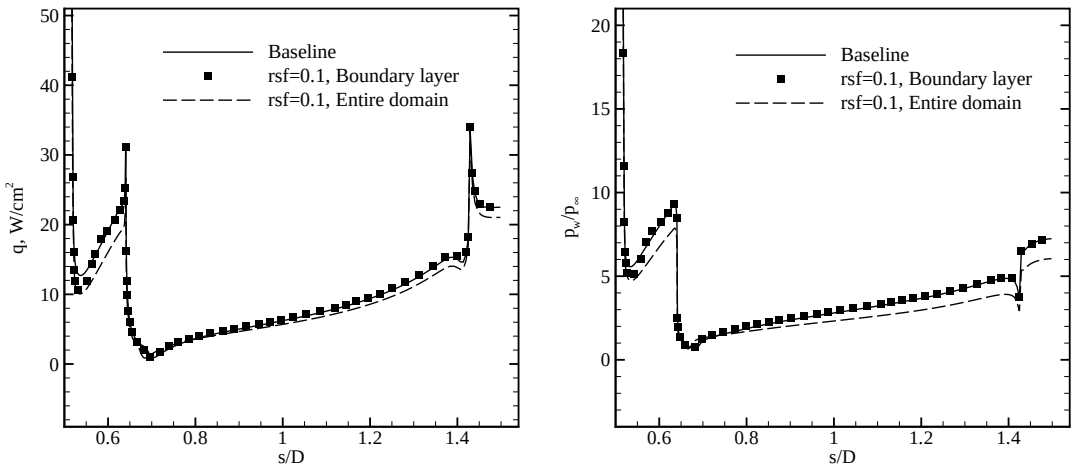

(a) (b)

Figure 4.20: Effect of decreasing the reaction rates in the entire domain on afterbody surface properties: (a) heat flux, and (b) normalized pressure.

explained in Section 4.2.3 Once again, the effect is localized in the vicinity of the first expansion corner when the reaction rate constants are decreased only in the boundary layer region. For the case with reduced reactivity in the entire domain, the surface heating rate is reduced over the entire shoulder region ($0.52 < s/D < 0.64$). A similar reduction in the surface pressure on the shoulder can be seen in Fig. 4.20(b).

The afterbody surface data presented in Fig. 4.20 shows a marginal reduction in heating rate when the rate constants are decreased in the entire flowfield. The base heat flux is lower than the baseline value by 6.5%. The pressure predictions show a relatively larger deviation from the

baseline values, with a 16% reduction at the base stagnation point when the rate constants are lowered in the entire domain. The surface pressure is found to be more sensitive than the heat transfer rate to variation in separation bubble size, reported in Fig. 4.18.

4.3 Summary

Thermo-chemical state of the gas in the re-entry flowfield over FIRE II re-entry capsule at 35 km altitude is studied. Next, sensitivity of the aero-heating predictions is investigated by changing the chemical reaction rate constants from their baseline values reported in the literature. Reaction rate constants (both forward and backward) are increased by a factor of ten and then decreased by a factor of ten, while keeping the equilibrium constant same. The flow features such as shock stand-off distance, structure and size of the afterbody separation bubble; gas temperature and conductivity in the near-wall region computed from the altered reactivity simulations are compared with those obtained from the baseline rate constants. This comparison provides insight into the physical mechanism that leads to the variation in the heat flux. The contributions of the near-wall gas temperature and thermal conductivity to the heating rate variations are analyzed at nose stagnation point, shoulder and base stagnation point. At the current freestream conditions, typical of a low altitude re-entry trajectory point, surface heat transfer rate is mainly affected by the variations in oxygen atom recombination rate in the boundary layer. Increasing the reaction rate enhances the heating rate, and vice versa. Nose stagnation point heat flux is found to be relatively insensitive to an enhancement in rate constants, on the other hand a higher sensitivity is observed at the shoulder region.

Chapter 5

Heating Rate Variations at 70 km Altitude

The changes in the heat flux due to the variation in reaction rates at a typical high altitude condition is examined in this chapter. 70 km altitude point of AS-202 re-entry trajectory [39] is chosen as a higher altitude condition and the corresponding freestream conditions are listed in Table. 5.1. The stagnation enthalpy at this condition is higher than that of the 35 km case where as the density is two orders orders of magnitude lower. The high freestream Mach number at this condition leads to a non-smooth variation in the heat flux at the nose stagnation point. A method to alleviate this irregularity in the computed heat flux is explained. Thermo-chemistry of the flowfield is studied in detail to understand the effects of higher total enthalpy and lower density of the freestream.

5.1 Simulation Methodology

The procedure followed to study the heating rate variations due to the uncertainty in reaction rates is similar to that presented in Sec. 4.1.1. Initially rate constants are varied only in the boundary layer to study the local chemistry effects of boundary-layer. Subsequently simulations are performed by varying the rate constants in the entire domain to study the effects of chemical reactions occurring in the shock layer. The grid topology used in these simulations is similar to that used at 35 km condition. However the outer boundary is modified according to the shock location at this condition.

No-slip, non-catalytic and isothermal boundary conditions are specified at the wall. The temperature of the wall is assumed to be 553.3 K, and is same as that used in the lower altitude simulations. The vibrational temperature is assumed to equilibriate with the translational tem-

Table 5.1: Freestream conditions at 70 km altitude trajectory point.

Free-stream Conditions	
ρ_∞ (kg/m^3)	0.000152
U_∞ (m/s)	7920
T_∞ (K)	227
M_∞	26.2
$Re_{\infty D}$	4.79×10^4
H_0 (MJ/kg)	31.53

perature at the wall. Freestream conditions are applied at the outer boundary and extrapolation condition is imposed at the exit station. A grid convergence study is performed to find out the minimum requirements of grid-point density and is explained below.

5.1.1 Grid Convergence

Simulations are performed on successively refined grids to assess the sensitivity of the computed solution to the grid-point density. Grid independence is evaluated in terms of the predicted surface heat flux, which is found to be most sensitive to the variation in computational mesh. Tolerance levels for grid independence are reported below. First, grid convergence of the forebody solution is presented. Next, sensitivity of the nose stagnation-point heating to the shock-grid misalignment is described. Finally, the afterbody grid-refinement study is discussed.

Figure 5.1 shows the forebody surface heat flux computed on three successively refined meshes. The 120$\times$101 grid has 50 wall-parallel points on the forebody, while the 240$\times$171 and 400$\times$241 grids have 100 and 160 forebody points. In the wall-normal direction the three grids have 101, 171 and 241 points respectively. The surface heat flux is plotted as a function of the normalized arc length (s/D) measured from the nose stagnation point. There is noticeable difference between the first two grid solutions, both on the forebody and shoulder. By comparison, the heat transfer rates obtained from the two finer grids (240$\times$171 and 400$\times$ 241) are almost identical, except for the nose stagnation region ($s/D < 0.1$).

All the grids show a dip in the heating rate near $s/D = 0$. This non-physical effect is due to the numerical errors caused by a mis-alignment of the grid lines to the bow shock contours.

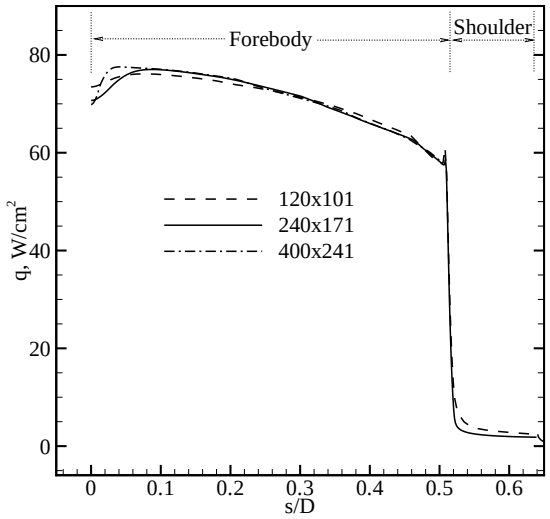

Figure 5.1: Effect of successive grid refinement on forebody heat flux.

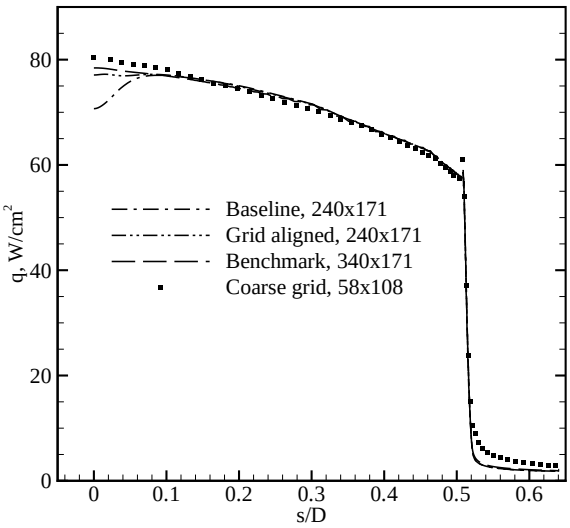

Figure 5.2: Effect of aligning the grid lines to the shock wave on the stagnation point heating rate.

Saunders $et\ al.$ [45] propose an algorithm to tailor the grid lines to the bow shock in order to eliminate the irregularities in the predicted heat flux. Starting with an initial grid and the corresponding solution, the algorithm generates a new grid by re-distributing the points so that the grid lines are better aligned to the bow shock. Simulations are performed on the modified grid, and the alignment procedure is repeated until the non-physical variation in heating rate is completely eliminated.

We use the above algorithm to rectify the heat flux variation in the nose stagnation region.

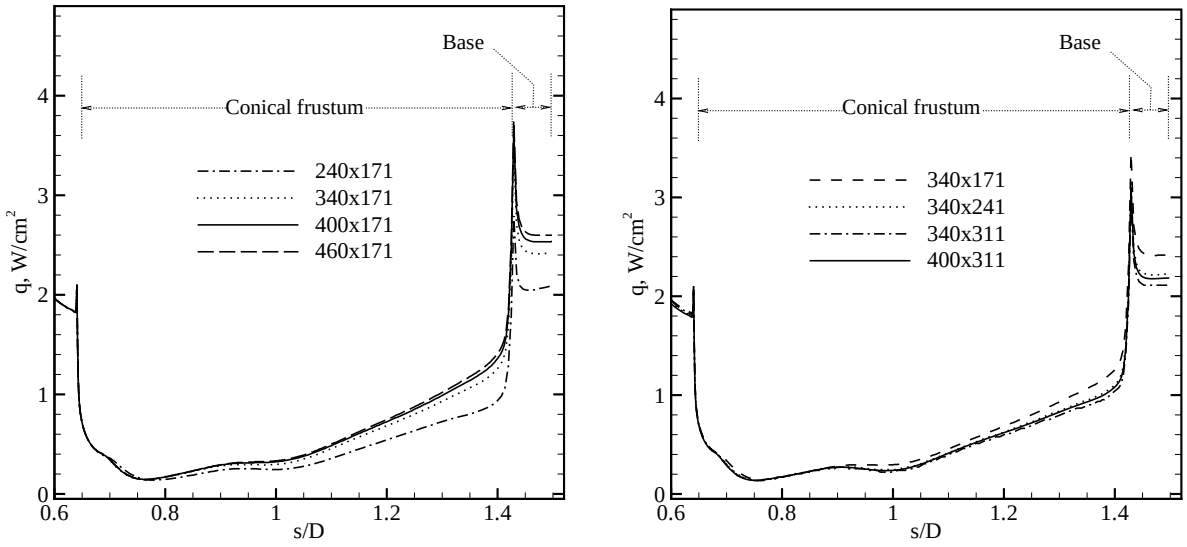

(a) (b)

Figure 5.3: Heat transfer rate obtained on successively refined grids on the afterbody: (a) wall-parallel, and (b) wall-normal directions.

Repeated application of the algorithm on the 240×171 grid presented above leads to a relatively monotonic variation of heating rate in the stagnation region, and the corresponding solution is marked as the grid-aligned solution in Fig. 5.2. Further improvement in the stagnation point heat flux prediction is achieved by additional grid refinement (by a factor of two in the i-direction on the forebody) and repeated alignment to the bow shock. One of the best results from the fine mesh simulations is presented as the benchmark solution and is used for further comparison.

For all the grids presented above, the wall-parallel grid spacing at the nose stagnation point is about 0.1 cm. It is found that a mesh with much larger grid spacing (approximately 0.9 cm) at nose results in a lower sensitivity of the computed solution to the grid-shock misalignment. Heating rate obtained from such a coarse grid simulation, with 58 wall-parallel grid points on the forebody, is shown in Fig. 5.2. It is fairly monotonic in the stagnation region ($s/D < 0.1$), even without extensive grid alignment. The coarse mesh heating rate prediction compares reasonably well with that of the benchmark solution, with a maximum deviation of about 2.5% at the stagnation point.

Next, grid sensitivity of afterbody solution is studied. Starting with the 240×171 grid presented above, successive refinement in the i-direction is performed without altering the grid-point distribution in the j-direction. The four grids presented in Fig. 5.3(a) have 140, 240, 300 and 360 wall-parallel points on the afterbody. The forebody is spanned by 100 points in

each case. All the solutions show similar heat flux variation along the afterbody. There is a converging trend in the heating values with successive refinement, and the two finest grids (400×171 and 460×171) predict practically the same heat transfer rate on the conical frustum. Maximum deviation between the two solutions occurs at the base stagnation point and is about 2.8%. Hence, 400 points in the wall-parallel direction with 300 points on the afterbody is taken to be sufficient to obtain a grid-independent solution.

Figure 5.3(b) shows the effect of refining the grid in the wall-normal direction, while keeping the wall-parallel grid unchanged. Three grids with 171, 241 and 311 wall-normal points are considered. Heating rate successively reduces with refinement such that minimal changes are observed between the two finer grids (340×241 and 400×311). Once again, maximum difference in heat flux is observed at the base stagnation point, and is about 4%. Further refinement in the j-direction is expected to give even smaller variation in surface heat flux. Hence, a total of 311 points in the wall-normal direction is taken to be adequate to obtain a grid-converged solution.

Based on the above study, a 400×311 grid with 100 points on the forebody and 300 points on the afterbody in the wall-parallel direction is selected for further simulations. The grid has a wall-normal spacing of 0.5×10^{-6} m and cell Reynolds number of 0.4 or less. Afterbody heat transfer rate obtained from this grid is shown in Fig. 5.3(b). However, as depicted in Fig. 5.2, a solution obtained on a mesh with 100 wall-parallel grid points on the forebody is sensitive to grid-shock mis-alignment, which causes irregularity in the computed heat flux. The grid-shock mis-alignment does not have an effect on afterbody solution and associated surface properties. Hence afterbody surface heat flux and wall pressure presented below are obtained from the full body simulations performed on the 400×311 grid.

Achieving a smooth variation in heating rate at the nose stagnation point on 400×311 mesh requires many grid-alignment iterations. This process is cumbersome and highly time consuming, when applied for all the altered reactivity simulations planned in this work. As an alternative, we use the coarse mesh (120×108) shown in Fig. 5.2 for further forebody simulations due to its robustness, and the results are expected to be accurate with in the limit specified above. The wall-normal spacing in the coarse mesh is 1×10^{-6} m and the corresponding cell Reynolds number is 0.83 or less.

5.2 Results

A brief description of the computed re-entry flowfield and surface properties is given below. Next, the details of the thermo-chemical state of the gas and chemical reactions in the boundary layer are presented. The effect of variation in the chemical reaction rates on heating predictions is explained subsequently.

Figure 5.4 shows the computed flowfield in terms of Mach number and temperature distribution. The prominent features like bow shock and flow expansion at the corners can be easily identified. The flow on the forebody is subsonic with Mach number approaching unity close to the first expansion corner. The post-shock temperature in the nose stagnation region is about 7000 K. Flow expansion at the first corner reduces the temperature to 1000 K. Further expansion around the second corner decreases the temperature to about 800 K.

The boundary layer remains attached on the forebody and shoulder, and separates immediately downstream of the second corner. The recirculation bubble on the afterbody is characterized by a single toroidal vortex that extends up to 1.53 diameter downstream of the base. In a majority of the separation bubble, the flow is subsonic with vortex core temperature of about 1800 K. The shear layer enclosing the recirculation region coalesce at the neck and a recompression shock wave is formed. The temperature of the gas in the neck region is close to 2500 K. The temperature in the inviscid region outside the separation bubble is about 1000 K and the Mach number is about 4.5. The reversed flow along the axis reaches a supersonic Mach number of 1.16. A normal shock is formed at the base (see Fig. 5.4(b)) to decelerate the flow to a subsonic Mach number.

Figure 5.5(a) shows the computed heat transfer rate on the forebody surface as a function of the normalized arc-length (s/D) measured from the nose of the vehicle. The heat transfer rate gradually decreases on the forebody from a maximum value of 80.49 W/cm^2 at the nose stagnation point. The heating rate falls rapidly at the expansion corner ($s/D = 0.52$) as the gas temperature drops due to flow expansion. The afterbody heat transfer rate is shown in Fig. 5.5(b), where the extent of the conical frustum and the base are identified. The expansion corners are marked by local peaks in the heat flux. In between the two expansion corners, the heating rate increases from the separation point at the shoulder to the base corner. The base stagnation point heat flux is 2.08 $\mathrm{W/cm^2}$, which is 2.7% of the nose stagnation point value. The minimum heat transfer rate observed on the conical frustum ($\sim$ 0.15 W/cm^2) is close to that measured on the Apollo afterbody ($\sim$ 0.2 W/cm ^{2}) at identical freestream conditions. [39]

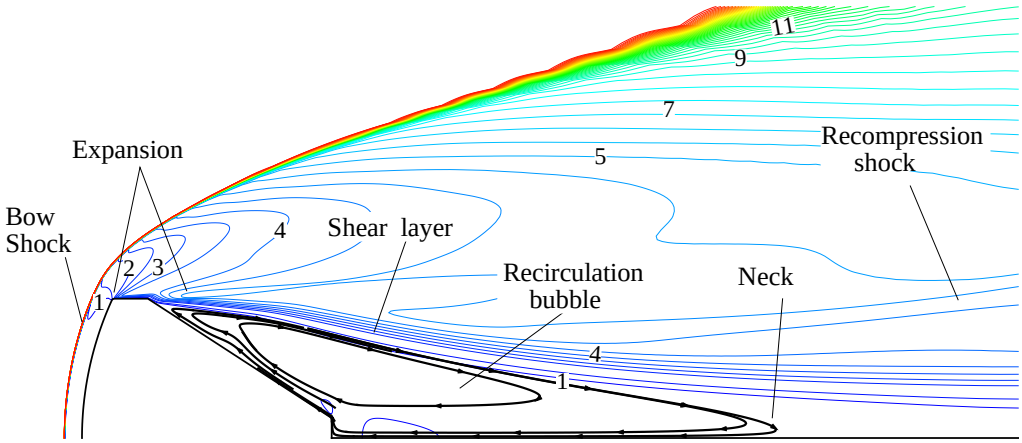

(a)

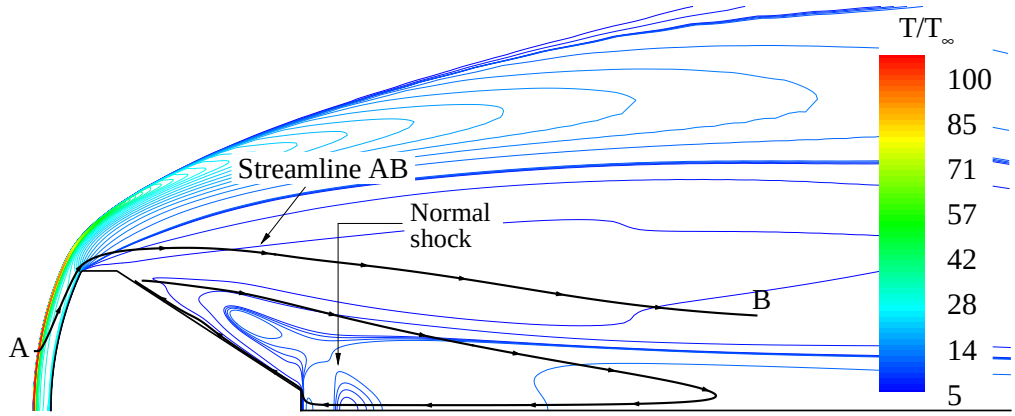

(b)

Figure 5.4: Computed flowfield around a re-entry capsule at Mach 26.2: (a) Mach number and (b) non-dimensional temperature distribution. Representative streamlines are shown on the afterbody to identify the recirculation bubble.

It is difficult to compare the computed and measured base heat fluxes because of a non-zero angle of attack during flight.

5.2.1 Boundary Layer Thermo-Chemistry

The variation of gas temperatures in the thermal boundary layer at the nose stagnation point is presented in Fig. 5.6(a). Local boundary-layer thickness is used to non-dimensionalize the wall-normal distance. Hence $l/\delta = 0$ represents the vehicle surface and $l/\delta = 1$ corresponds to the boundary-layer edge. Flow is in thermal equilibrium ($T \simeq T_v$) at the edge of the boundary layer, with both translational and vibrational temperatures around 6560 K. In the boundary layer, both

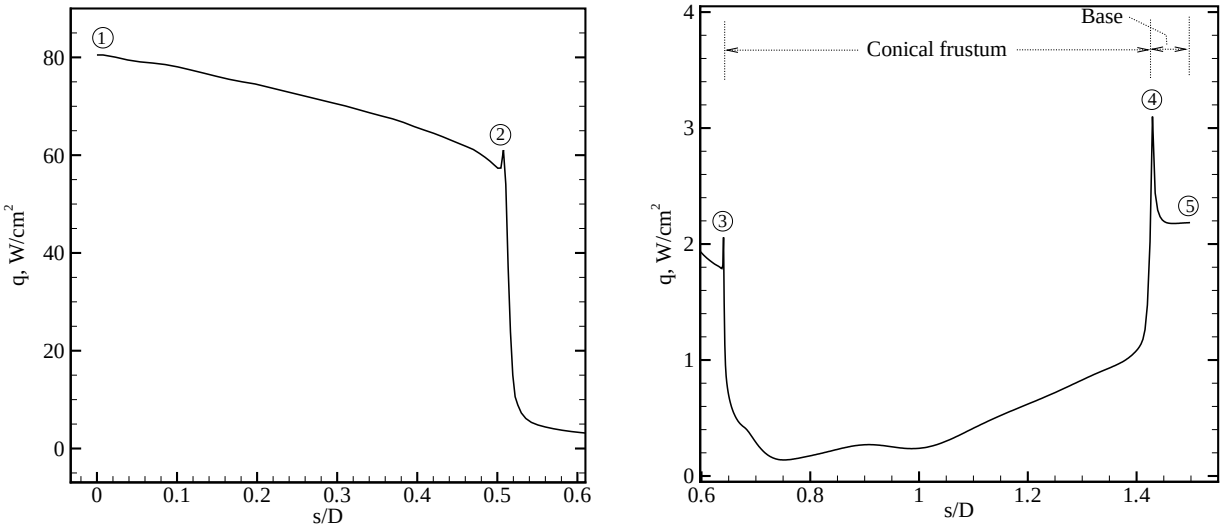

(a) (b)

Figure 5.5: Heat transfer rate obtained from the baseline simulation (rsf = 1): (a) forebody, and (b) afterbody. Geometry points 1, 2, 3, 4 and 5 are identified in Fig. 3.1(c).

temperatures decrease monotonically to reach the wall value of 553.5 K.

The freestream gas is composed of oxygen and nitrogen molecules, with mass fractions of 0.233 and 0.767 respectively. The high temperature of the gas in the shock layer causes complete dissociation of the oxygen molecules and a partial dissociation of the nitrogen molecules. As a result, mass fraction of N_2, N and O species attain values of 0.23, 0.54 and 0.23 respectively at the boundary-layer edge (see Fig. 5.6(b)). Concentrations of the remaining two species are negligible. The decrease of gas temperature in the boundary layer initiates chemical reactions. As a result, mass fraction of N_2 increases to 0.52 at the wall with a corresponding decrease in Y_{N}. However, Y_{O}, $Y_{\mathrm{O_2}}$ and Y_{NO} remain constant throughout the boundary layer. The change in gas composition across the boundary layer is explained below with the aid of Fig. 5.7, which depicts the chemical reaction rates and the species source terms in the boundary layer.

The chemical reactions and associated source terms are effective in the vicinity of the wall ($l/\delta < 0.05,\ i.e.$ 5% of the boundary-layer thickness). However, the concentrations of N_2 and N change throughout the boundary layer due to mass diffusion. The largest reaction rate corresponds to NO recombination (see Fig. 5.7(a)).

$$R_3 > 0 \qquad\qquad \mathrm{N + O + M \rightarrow NO + M}$$

The newly created NO molecules collide with the available N atoms to form N_2 molecules

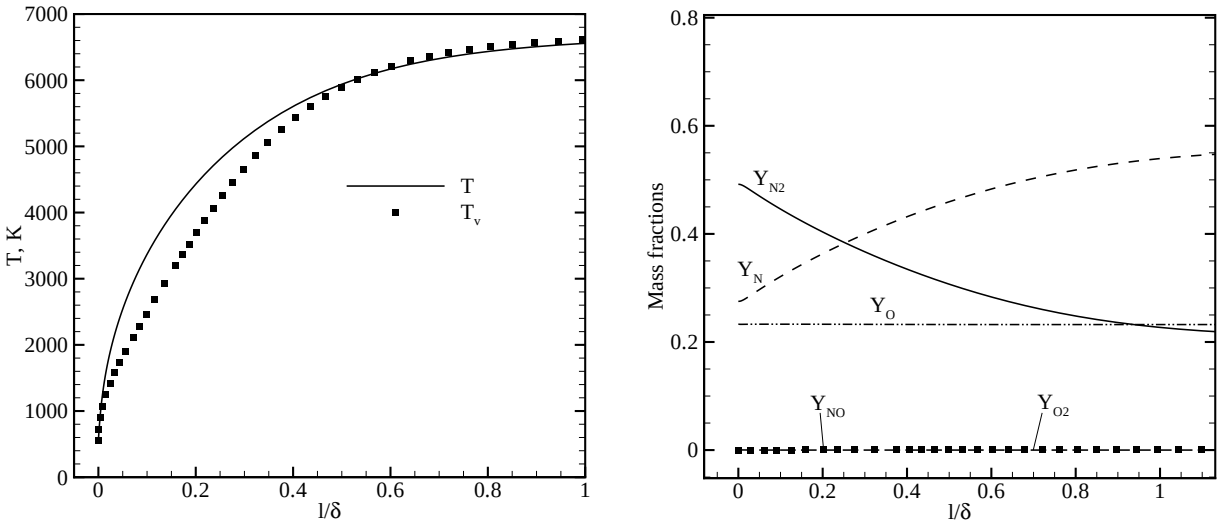

(a) (b)

Figure 5.6: Distribution of (a) temperatures and (b) species mass fraction in the thermal boundary layer at the nose stagnation point.

through exchange reaction (4)

$$R_4 > 0 \qquad \mathrm{NO + N \rightarrow N_2 + O}$$

For $l/\delta > 0.005$, it is seen that $R_3 \simeq R_4$, and therefore the net effect of the above two reactions is 2N $\rightarrow$ N_2 with negligible influence on O_2, O and NO. This results in equal and opposite source terms for N_2 and N (see Fig. 5.7(b)), and the other source terms (for O_2, O and NO) are approximately zero. The reaction rates R_3 and R_4 attain peak value at $l/\delta \approx 0.004$ leading to maximum $W_{\mathrm{N_2}}$ and minimum W_{N} at this location. A local peak in the source term of N_2 is also observed at $l/\delta \sim 0.012$, which is due to non-zero R_1 in this region.

Availability of NO molecules is critical for continuation of the exchange reaction. As R_3 drops to negligible values for $l/\delta < 0.004$, the magnitude of R_4 decreases (see Fig. 5.7(a)). For $0 < l/\delta < 0.004$, R_2 and R_5 attain non-negligible values and provide the NO required for reaction (4). The resulting reaction mechanism that leads to the recombination of N atoms is as follows. First, the recombination of oxygen atoms occurs via

$$R_2 > 0 \qquad \mathrm{O + O + M \rightarrow O_2 + M}$$

The newly formed oxygen molecules collide with N atoms, as per reaction (5), resulting in the formation of NO and O atoms

$$R_5 > 0 \qquad \mathrm{O_2 + N \rightarrow NO + O}$$

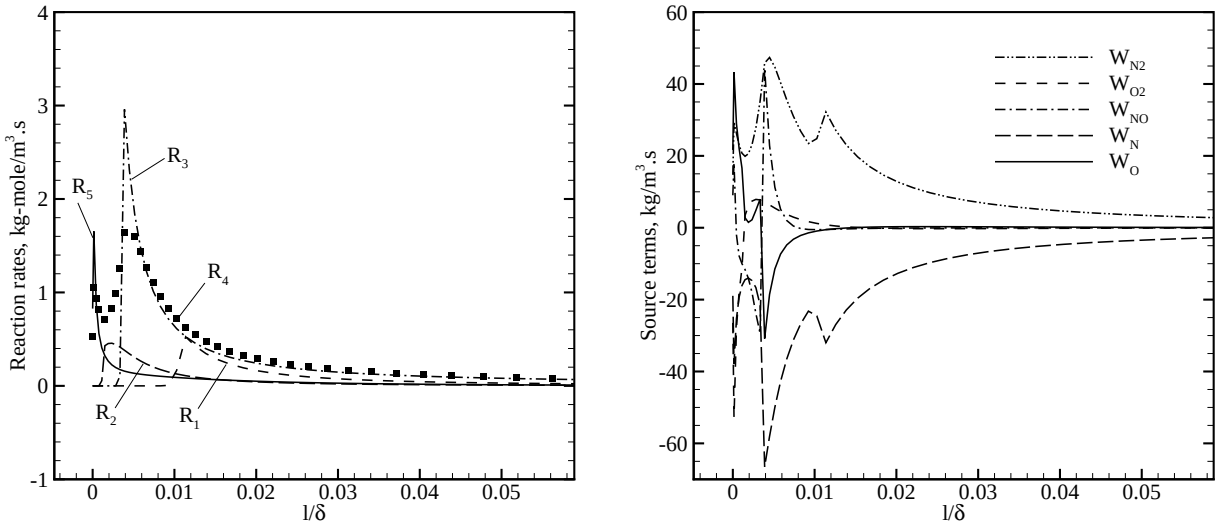

(a) (b)

Figure 5.7: Variation of (a) reaction rates and (b) species source terms in the thermal boundary layer at the nose stagnation point.

The newly created NO molecules collide with the available N atoms to form N_2 molecules via reaction (4)

$$R_4 > 0 \qquad\qquad \mathrm{NO + N \rightarrow N_2 + O}$$

The two exchange reactions (5) and (4) together result in the formation of N_2 and O while consuming N atoms. The newly formed O atoms again recombine as per reaction (2) to form O_2 molecules, which initiates reaction (5). Thus, the above three reactions constitute a chain mechanism, where O_2 molecules act as a catalyst in the conversion of N atoms to N_2 molecules with no net effect on O_2 and O concentration. This reaction mechanism is similar to that described by Park [**?**] for expanding nozzle flows. The chain reactions will cease when nitrogen recombination is complete. In the absence of N atoms, only recombination of oxygen will occur. At the current conditions, N atoms are not completely depleted, and therefore the concentrations of O_2 and O do not change. Note that $R_2 \neq R_4 \neq R_5$, with R_4 and R_5 attaining large local values in the immediate vicinity of wall. An imbalance in these three reactions produces local peaks in the source terms of O, O_2 and NO in the region $0 < l/\delta < 0.004$. However, there is no appreciable effect of these locally high values of the source terms on the corresponding species mass fractions (see Fig. 5.6(b)).

The conversion of N atoms to N_2 molecules in the boundary layer occurs via the two competing reaction mechanisms described above. The first mechanism (R_3-R_4) comprises re-

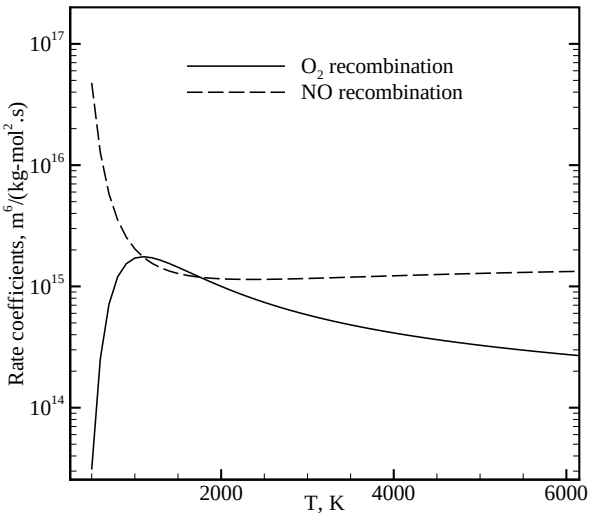

Figure 5.8: Comparison of baseline rate constant for O_2 and NO recombination.

actions (3) and (4), and is initiated by NO recombination. The second mechanism (R_2-R_5-R_4), consisting of reactions (2), (4) and (5), is initiated by O_2 molecules. The majority of the N_2 recombination occurs via the first mechanism. A preference for the R_3-R_4 mechanism can be explained by comparing the rate coefficients of NO and O_2 recombinations. The primary collision partners for these two reactions are N_2, N and O. The rate constants shown in Fig. 5.8 correspond to the case where the collision partner is an atom, and the temperature range spans the present boundary-layer conditions. The rate coefficient of NO recombination is higher than that of O_2 recombination, which indicates that NO recombination occurs at a faster rate than the latter. Hence, the R_3-R_4 mechanism initiated by NO molecules has a dominant contribution to N_2 formation. As N_2 recombination progresses, the concentration of N atoms decreases and leads to a sudden reduction in R_3 at $l/\delta = 0.004$ (see Fig. 5.7(a)). When NO molecules are not produced through reaction (3), O_2 recombination initiates the R_2-R_5-R_4 mechanism.

5.2.2 Altered Reactivity in the Boundary layer

Numerical simulations are performed by changing the rate constants of the five reactions individually and in groups to study their effect on the surface heat transfer rate. Magnitude of reaction rates, source terms and extent of N_2 formation obtained in the new simulations are compared with those in the baseline solution presented above. The reaction rate constants are first altered only in the boundary layer to study their local effects. Solutions are then computed by changing the rate constants in the entire domain.

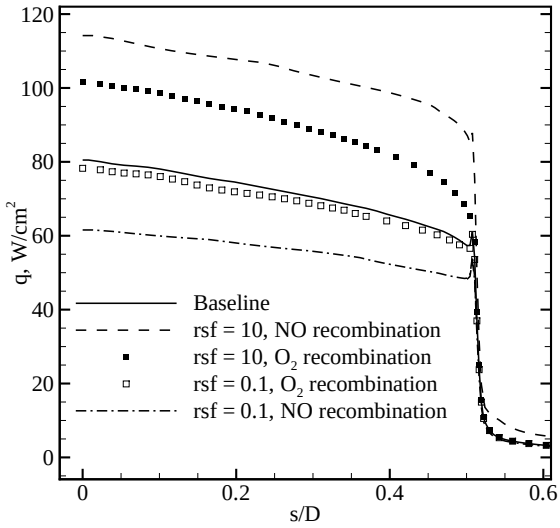

Figure 5.9: Forebody heating rate computed by changing reaction rates for NO and O_2 recombination. The baseline result (from Fig. 5.5(a) is reproduced for comparison.)

The rate constants of O_2 and NO recombination are varied initially as these two reactions initiate the two competing N_2-recombination mechanisms. The corresponding forebody heat transfer rates are plotted in Figure 5.9. It is found that a increase in the rate constant of NO recombination significantly enhances the heating rate on the entire forebody. Lowering the rate constants of this reaction decreases the surface heat flux. An increase in the O_2 recombination rate constants also leads to enhanced heating rate. However, the heat flux increment is lower than that obtained when NO recombination is enhanced. Further, decreasing the rate constant of O_2 recombination has minimal effect on the surface heat flux. The changes in gas chemistry due to altered reactivity in the boundary layer and the consequent variation in gas properties and surface heating rate are explained below.

Figure 5.10(a) shows the magnitude of reaction rates when rsf = 10 for NO recombination. The reaction rates qualitatively match those observed in the baseline simulation, as shown in Fig. 5.7(a). The R_3-R_4 mechanism is dominant, and the corresponding rates are increased over their baseline values. An enhanced production of NO molecules leads to an increase in magnitude of the exchange reaction rate R_4. The rates of other reactions (R_2 and R_5) remain relatively unchanged from their respective values in the baseline simulation. The associated changes in Y_{N_2} and Y_{N} are shown in Fig. 5.10(b). Formation of N_2 in the boundary layer is enhanced due to an increased magnitude of R_3 and R_4. Mass fraction of N_2 reaches a value of 0.68 at the wall, whereas Y_{N} decreases to 0.08.

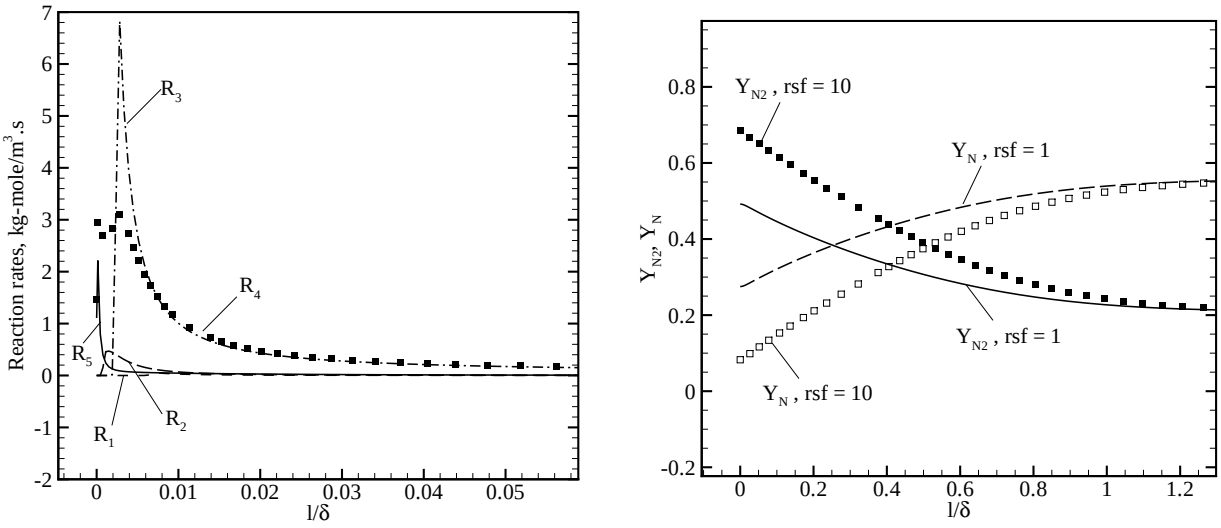

(a) (b)

Figure 5.10: Variation of (a) reaction rates and (b) gas composition in the boundary layer, when rsf = 10 for NO recombination.

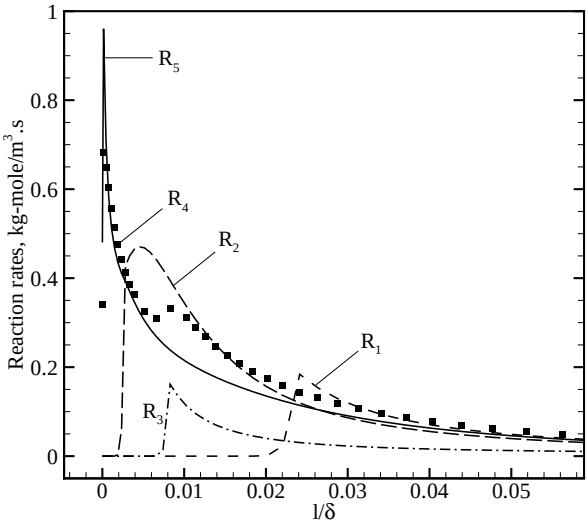

Figure 5.11: Magnitude of reaction rates when rsf = 0.1 for NO recombination.

Figure 5.11 shows the reaction rates obtained for the case with rsf = 0.1 for NO recombination. The magnitude of R_3 is greatly reduced compared to the baseline simulation, whereas the magnitude of R_2 is approximately equal to its baseline value. Note that the reduced NO recombination rate constant ($0.1 \times k_{b_3}$) is lower than the O_2 recombination rate constant k_{b_2} (Fig. 5.12). O_2 recombination therefore proceeds faster than NO recombination for this case, and formation of N_2 primarily occurs via the R_2-R_5-R_4 mechanism throughout the boundary layer. The reaction rates R_4 and R_5 are also found to be lower in this case than their respective

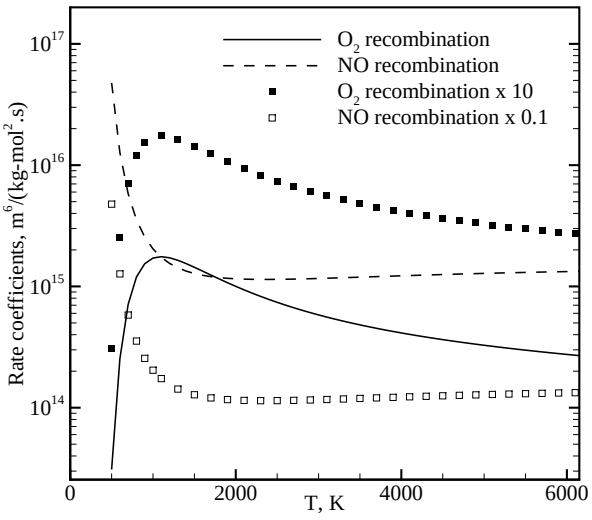

Figure 5.12: Comparison of altered rate constant for O_2 and NO recombination.

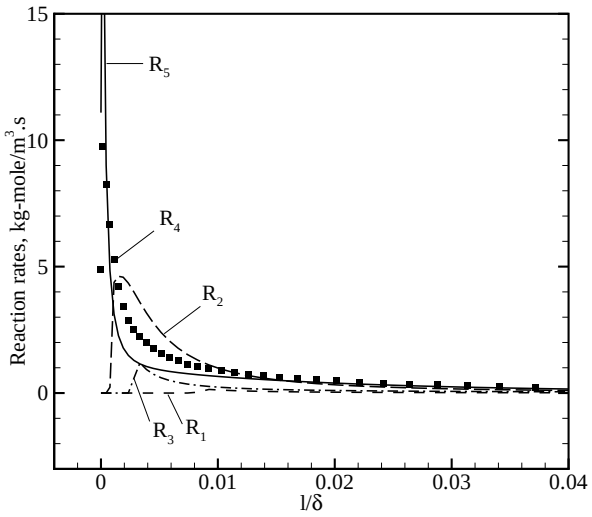

Figure 5.13: Magnitude of reaction rates when rsf = 10 for O_2 recombination.

baseline values. Overall, N_2 formation in the boundary layer is suppressed. Mass fraction of N_2 attains a value of 0.36 at the wall, as compared to the baseline value of 0.49.

Figure 5.13 presents the magnitude of reaction rates obtained when rsf = 10 for O_2 recombination. An increase in k_{b_2} makes the O_2 recombination proceed at a faster rate than NO recombination (see Fig. 5.12). Thus, the second mechanism (R_2-R_5-R_4) is favored for the formation of N_2 molecules in this case. The reaction rates R_2, R_5 and R_4 increase by a factor of ten, as compared to their respective baseline values. The higher reaction rates enhance N_2 formation near the wall, and result in a higher concentration of N_2 in the boundary layer (Y_{N_2}

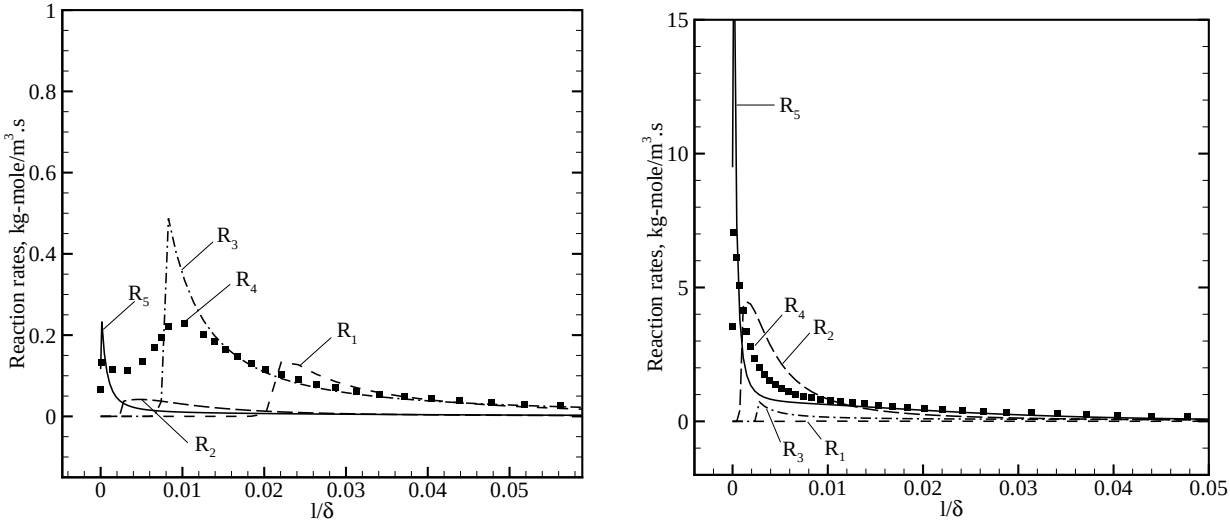

Figure 5.14: Magnitude of reaction rates when (a) rsf = 0.1, and (b) rsf = 10 for all reactions.

= 0.63 at the wall). On the other hand, when k_{b_2} is decreased, the magnitude of R_2 decreases by ten times and this results in suppression of R_2-R_5-R_4 mechanism in the vicinity of wall. Compared to the R_3-R_4 mechanism, which has a dominant contribution to N_2 formation in this case, suppression of R_2-R_5-R_4 mechanism has negligible effect on the extent of recombination. Mass fraction of N_2 approaches 0.48 at the wall, as compared to 0.49 in the baseline solution.

Altering the rate constants of exchange reactions (4) and (5), and N_2 recombination reaction (1) independently has negligible effect on the stagnation point heating rate. The essential species required for N_2 formation are O_2 or NO. The reactions (1), (4) and (5) do not produce the above two species in the boundary layer. Hence, changing the reactivity of these three reactions does not alter the N_2 formation process. On the other hand, increasing (decreasing) the reactivity of either O_2 or NO recombination enhances (suppresses) the respective mechanisms of N_2 production. Thus, we can say that O_2 and NO recombination reactions are the rate limiting steps in the N_2 recombination process.

Next, we alter the rate constants of all five chemical reactions simultaneously in the boundary layer, and the corresponding reaction rates are shown in Fig. 5.14. In case of the reduced reactivity (rsf=0.1), the N_2 recombination process is similar to that observed in the baseline simulation (Fig. 5.7(a)), but the magnitude of all reaction rates is lower than their corresponding baseline values. The majority of recombination occurs via the R_3-R_4 mechanism, and the R_2-R_5-R_4 mechanism is active in the immediate vicinity of wall. The key element in the above

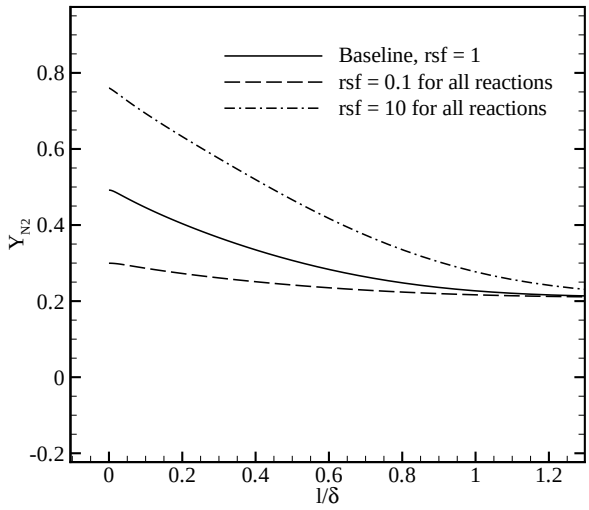

Figure 5.15: Variation of Y_{N_2} across the boundary layer for the baseline and the altered reactivity cases.

chain reactions is availability of either NO or O_2 molecules. A decrease in the rate constants of O_2 and NO recombination reduces the formation of O_2 and NO molecules respectively, and this leads to a reduction of the exchange reaction rates R_4 and R_5. Thus, there is a marginal recombination of N atoms across the boundary layer (see Fig. 5.15), with Y_{N_2} = 0.3 at the wall.

Figure 5.14(b) plots the reaction rates across the boundary layer for the higher reactivity simulation (rsf = 10 for all reactions). The reaction mechanism R_2-R_5-R_4 is preferred in this case for the recombination of N atoms. The rates of the three reactions are enhanced significantly. An increase in the rate constants of O_2 recombination results in a higher availability of O_2 molecules. This, along with an increased rate constant k_{b_5}, enhances the magnitude of R_5 more than ten times, as compared to its baseline value. A higher R_5 increases the production of NO and O, which in turn leads to an increase in the magnitude of R_4. This results in higher level of N_2 and O. The newly created O atoms again recombine to form O_2 molecules, which accelerate the loop reactions further. Thus, the present N_2 recombination is a chain mechanism and an increase in one reaction rate recursively enhances the other dependent reactions. The net effect is a large increase in the N_2-level in the boundary layer (see Fig. 5.15). The mass fraction of N_2 reaches a value of 0.76 at the wall, which is 55% higher than the baseline value.

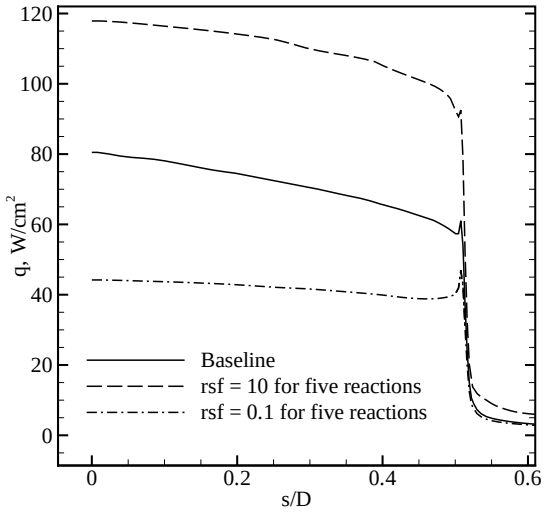

Figure 5.16: Effect of simultaneous alteration of rate constants on forebody heat transfer rate.

5.2.3 Effect on Surface Heat Flux

Increasing and decreasing the rate constants of five reactions simultaneously result in a stagnation point heating rate of 117.87 and 44.20 W/cm^2 respectively (see Fig. 5.16). The heating-rate enhancement obtained when all the reaction rates are increased is higher than that obtained when rate constants of O_2 or NO recombinations are increased individually (see Fig. 5.9). This is because all reactions in the boundary layer proceed in the exothermic direction and they favor the recombination process. An increase in the rate constant of an individual reaction therefore enhances N_2 formation, and increasing the rates of all five reactions simultaneously leads to the formation of N_2 to the highest extent. The corresponding heat release is highest when all the reaction rates are increased and it enhances the surface heat flux. On similar lines, the heat released due to exothermic reactions is minimum when the rates of all five reactions are decreased. The corresponding heat flux is lower than those obtained by reducing the rate constants of individual reactions.

The heat flux to the vehicle surface is a function of near-wall gas temperature and the mixture conductivity. The change in the heat flux due to varying reaction rates can, therefore, be expressed in terms of the changes in the thermal conductivity and the gas temperature adjacent to wall T_2.

$$\frac{\triangle q}{q} = \frac{\triangle \kappa}{\kappa} + \frac{\triangle T_2}{T_2 - T_w} \tag{5.1}$$

where higher-order terms are neglected. A quantitative analysis of the changes in heat flux, due

Table 5.2: Contribution of $\triangle\kappa/\kappa$ and $\triangle T_2/(T_2-T_w)$ to $\triangle q/q$ in the higher (rsf = 10) and lower (rsf = 0.1) reactivity cases at the nose stagnation point.

% change	rsf = 10	rsf = 0.1
$\triangle\kappa/\kappa$	-16.79	9.42
$\triangle T_2/(T_2-T_w)$	76.00	-49.85
$\triangle q/q$	46.46	-45.08

to varying reaction rates at different locations is given below.

Nose stagnation point

A budget of Eq. (5.1) for the stagnation point heat flux for the higher and lower reactivity simulations is shown in Table 5.2, where the changes are calculated with respect to the baseline simulation values. Enhancing the reactivity (rsf = 10) increases the gas temperature in the near-wall region by 76%, and the gas temperature decreases by about 50% when the reaction rates are reduced (rsf = 0.1).

At the current boundary-layer conditions, the relative magnitude of thermal conductivity among the species is:

$$\kappa_{\mathrm{N}} > \kappa_{\mathrm{O}_2} > \kappa_{\mathrm{NO}} > \kappa_{\mathrm{N}_2} > \kappa_{\mathrm{O}} \tag{5.2}$$

Molecular nitrogen has lower thermal conductivity than its atomic counterpart. Increasing (decreasing) the reaction rates results in a higher (lower) mass fraction of N_2, thereby reducing (enhancing) the overall mixture conductivity. It decreases by 16.79% for the higher reactivity simulation and increases by 9.42% in the lower reactivity case. The changes in conductivity are opposite to those in the near-wall gas temperature. The heat release or the temperature effect is found to be the dominant contribution to the surface heat transfer rate. The net effect is an enhancement in the stagnation point heating rate by 46.46% when the rate constants are increased, and a reduction in the heat flux by 45.08% when the rate constants are decreased. Note that the changes in thermal conductivity and temperature do not match the net change in q as per Eq. (7.5), because of the contributions of higher-order terms that are neglected in the analysis.

The equilibrium gas composition for the prescribed wall temperature and the computed

Table 5.3: Contribution of $\triangle\kappa/\kappa$ and $\triangle T_2/(T_2 - T_w)$ to $\triangle q/q$ at the shoulder ($s/D = 0.52$).

% change	rsf = 10	rsf = 0.1
$\triangle\kappa/\kappa$	-10.87	6.14
$\triangle T_2/(T_2 - T_w)$	57.14	-26.53
$\triangle q/q$	41.65	-21.25

wall pressure is Y_{N_2} = 0.767, Y_{O_2} = 0.233 and $Y_{NO} = Y_N = Y_O = 0.0$. In the present computations with the baseline rate constants, Y_{N_2} and Y_{O_2} values are 0.492 and 5×10^{-5} respectively at the nose stagnation point. The gas composition is far from its local equilibrium state. An increase in chemical rate constants takes the gas closer to the equilibrium state by promoting the recombination reactions. The mass fraction of N_2 for the higher reactivity case is 0.76 (see Fig. 5.15), $i.e.$ N_2 recombination is almost complete. On the other hand, Y_{O_2} approaches a value of 0.002 at the wall in the higher reactivity simulation. There is negligible O_2 formation in spite of the enhanced reactivity. This is because any O_2 molecule formed is used up by the subsequent reactions in the R_2-R_5-R_4 mechanism leading to N_2 formation. Any change in O_2 is expected to be seen only when N_2 recombination is complete and the chain mechanism is disrupted because of non-availability of N atoms.

Forebody

Note that the changes in heat flux to the variation in reaction rates is highest at the nose stagnation point, and it decreases along the forebody and shoulder. For example, the stagnation point heat flux decreases by about 36 W/cm^2 in the lower reactivity solution presented in Fig. 5.16, where as the variation is less than 17 W/cm^2 near the shoulder ($s/D = 0.5$). Similar trends are observed in the gas composition across the boundary layer. The changes in Y_{N_2} at the nose stagnation point (see Fig. 5.15), due to variations in the rate constants, are higher than those at the shoulder location. This is because the gas is in a chemical non-equilibrium state at the stagnation point, and approaches a frozen state as the flow expands along the body. The degree of non-equilibrium progressively decreases from the nose to the shoulder.

Table 5.3 shows a budget of Eq. (5.1) at the first expansion corner ($s/D = 0.52$) for the higher and lower reactivity cases, when all the reactions rates are altered simultaneously. The changes are calculated with respect to the baseline solution. The mixture conductivity decreases

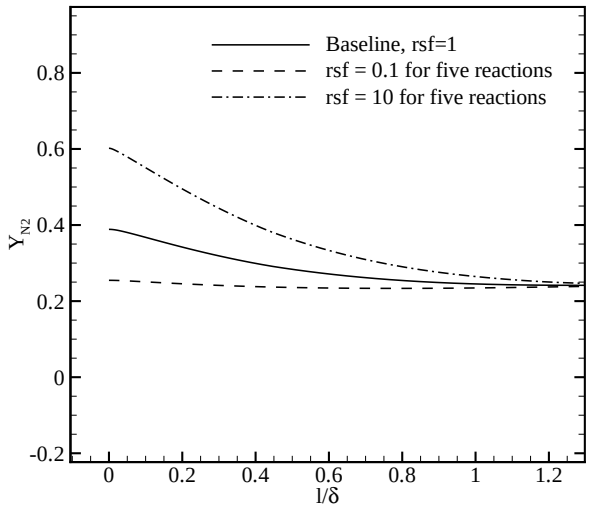

Figure 5.17: Effect of alteration of reaction rates in the boundary layer on N_2 recombination at the shoulder ($s/D = 0.52$).

Table 5.4: Contribution of $\triangle\kappa/\kappa$ and $\triangle T_2/(T_2 - T_w)$ to $\triangle q/q$ at the base stagnation point ($s/D = 1.5$).

% change	rsf = 10	rsf = 0.1
$\triangle\kappa/\kappa$	-7.52	4.39
$\triangle T_2/(T_2 - T_w)$	15.38	-7.69
$\triangle q/q$	10.55	-5.96

by 10.87 % in the higher reactivity solution. This is because of a higher N_2 concentration and a lower amount of N in the rsf = 10 solution. This is countered by an increase in near-wall gas temperature (by 57.14 %) due to enhanced recombination reactions. The net effect is an increase in heating rate by 41.65% when the rate constants are increased. Opposite trends are observed in case of lower reactivity simulation. The mixture conductivity increases by 6.14 % and the near-wall gas temperature decreases by 26.53 %, resulting in a net reduction in heating rate by 21.25 %. At this location also the changes in the thermal conductivity and temperature do not add up to the net change in q as per Eq. (7.5), because of the contributions of higher-order terms that are neglected in the analysis.

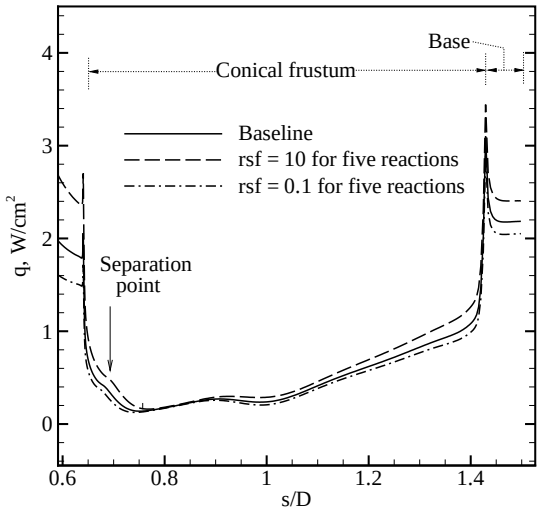

Figure 5.18: Effect of variation in reaction rates on afterbody heating rate. The location of the separation point on the conical frustum (s/D = 0.69) is shown for the baseline case.

Afterbody

Figure 5.18 depicts changes in the afterbody heat transfer rate when the rate constants are altered for the five reactions in the boundary layer. The location of the separation point on the conical frustum differs slightly among the three simulations. Downstream of the separation point the heating rate computed from the higher reactivity simulation gradually increases above the baseline heating rate. Maximum enhancement is observed at the base stagnation point ($s/D = 1.5$), which is about 10.55% of the baseline value.

The changes in the afterbody heating rate due to the reaction rate variation are much lower than those observed on the forebody. This is due to the low density of the gas on the afterbody that results in a frozen chemical state. This inhibits the recombination reactions in the near-wall region, and a constant value of Y_{N_2} is observed throughout the boundary layer in all the three simulations. Thus, altering the rate constants in the thermal boundary layer on the afterbody surface has negligible effect on the surface heat flux. The variation in the afterbody heating rate, observed in Fig. 5.18, is primarily because of changes occurring at the edge of the boundary layer. In the baseline simulation, the edge value of Y_{N_2} is 0.344, whereas it is 0.487 and 0.254 in higher and lower reactivity simulations respectively. The reason for this is similar to that reported in Sec. 4.2.4 and is described below.

The gas that is trapped in the afterbody recirculation bubble originates from the forebody boundary layer, where the gas composition is affected by changes in the reaction rates. Hence,

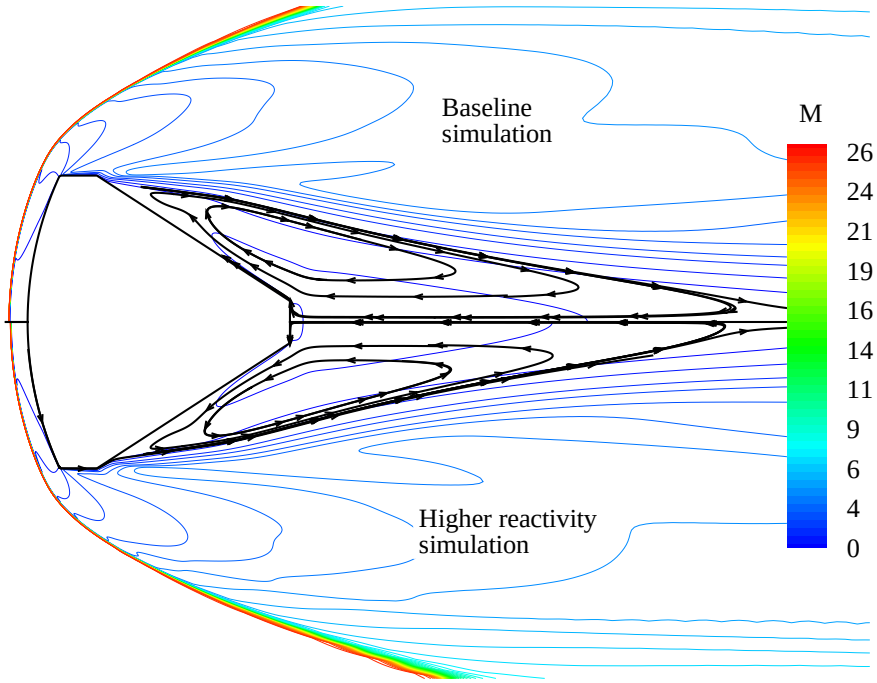

Figure 5.19: Comparison of Mach number distribution and separation bubble obtained from the baseline (top half) and higher reactivity (bottom half) simulations. Streamlines are drawn to demarcate the separation point and recirculation bubble size.

appreciable changes in Y_{N_2} are observed in the vortex core and free shear layer, although the reaction rates are not altered in these regions. This alters the gas composition at the edge of the afterbody boundary layer. Similar to the gas composition, temperature of the gas also differs at the boundary-layer edge among the three simulations. The changes in the boundary-layer edge values of composition and temperature alter the surface heat flux. The percentage change in κ and T_2 at the base stagnation point are listed in Table 5.4. For the higher reactivity case, conductivity decreases by 7.52% and T_2 increases by 15.38%, which result in a net enhancement of heating rate by 10.55%. Opposite effect is observed for rsf = 0.1 with a net decrease of heating rate by 5.96%.

5.2.4 Increased Reactivity in the Entire Domain

Next, numerical simulations are performed by varying the rate constants in the entire domain. This is to study the effect of shock layer thermo-chemistry on flow predictions. Figure 5.19 compares the flowfield solutions obtained from the baseline simulation (top half) and a higher reactivity simulation in which the rate constants are increased (rsf = 10) for all five reactions

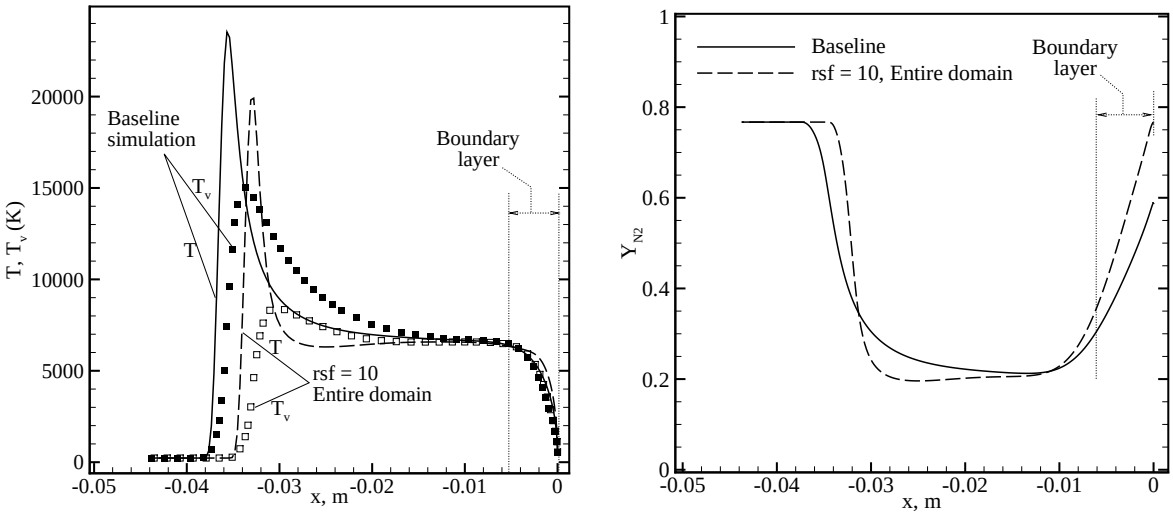

(a) (b)

Figure 5.20: Changes in (a) T and T_v and (b) Y_{N_2} on the stagnation streamline due to variation in rate constants. The flow is from left to right and the wall is located at $x = 0.0$ m.

uniformly over the entire computational domain. The two solutions are almost identical, except for a smaller stand-off distance (by 7.69%) in the higher reactivity case. The difference in the shock location can be clearly seen in Fig. 5.20(a), which plots T and T_v along the stagnation streamline for the two cases. This is due to the higher amount of dissociation at the shock wave in the higher reactivity simulation. The enhanced rate constants also result in reduced peak values of T and T_v by about 3600 and 6600 K respectively compared to the baseline solution.

Comparing the translational temperatures given by the two simulations in Fig. 5.20(a), a large difference is noticed in the vicinity of the shock wave and the difference reduces as we go downstream. Both solutions approach $T = 6300$ K close to the boundary-layer edge. Comparison of vibrational temperatures obtained from the two cases show a similar trend. In both the baseline and higher reactivity solutions, the gas is in a thermal non-equilibrium state in majority of the shock layer, and it reaches thermal equilibrium ($T = T_v$) close to the boundary-layer edge. Thus, all the temperatures plotted in Fig. 5.20(a) attain a value of 6300 K at the edge of the thermal boundary layer.

Figure 5.20(b) compares Y_{N_2} along the stagnation streamline for the two solutions. Similar to the temperature plot, there is a noticeable difference between the Y_{N_2} values obtained from the two simulations in the post-shock region. In the higher reactivity case, the chemical reactions equilibriate immediately downstream of the shock at $x \simeq$ -0.03 m, and the composition remains

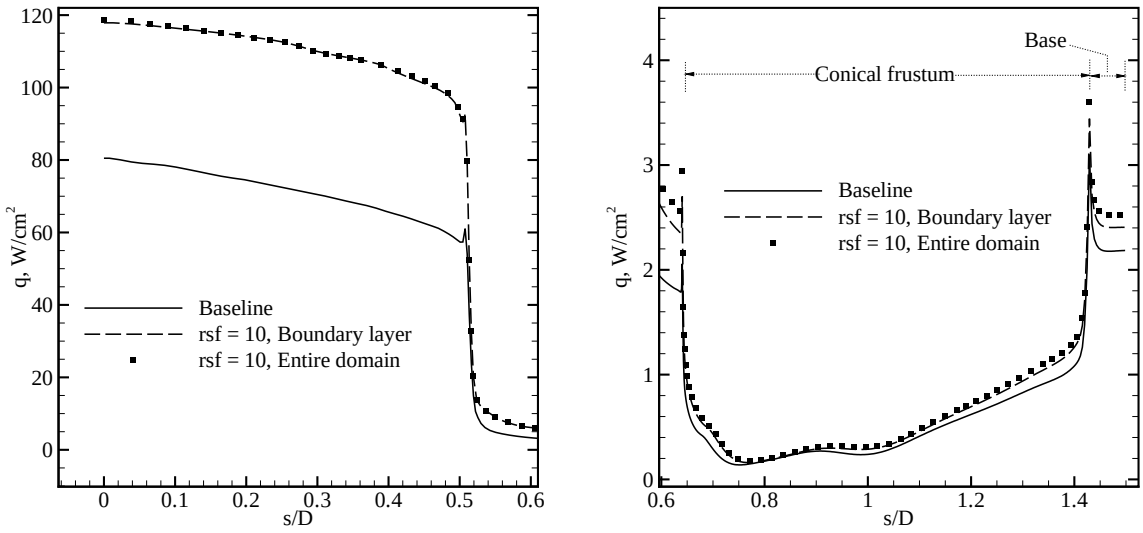

Figure 5.21: Effect of increasing the rate constants in the entire domain on heating rate: (a) forebody, and (b) afterbody.

constant thereafter. By comparison, there is a slower decrease in Y_{N_2} behind the shock in the baseline simulation, and the gas approaches chemical equilibrium close to boundary-layer edge ($x \simeq$ -0.008 m). Overall, the gas composition and temperatures obtained using higher reaction rate constants match those in the baseline simulation at the boundary-layer edge, in spite of large differences in the vicinity of the shock wave.

The variation of Y_{N_2} in the thermal boundary layer is also shown in Figure 5.20(b). Y_{N_2} obtained from the higher reactivity case reaches a higher value at the wall compared to the baseline simulation. This is similar to that observed when the reaction rate constants are increased only in the boundary layer (see Fig. 5.15). The wall value of Y_{N_2} obtained from the two higher reactivity simulations (entire domain and boundary layer) are almost identical. The concentration of nitrogen atoms show a similar trend. The mass fraction of other species, Y_{O_2}, Y_{O} and Y_{NO}, remain constant across the boundary layer, as observed in the baseline solution.

Figure 5.21(a) presents forebody heat flux obtained from the baseline and the two higher reactivity simulations. The heating rate enhancement due to increased reactivity in the entire domain is identical to that obtained when the reaction rate constants are altered only in the boundary layer. This is due to identical gas composition and temperatures across the boundary layer in the two higher reactivity simulations, as described above.

Comparison of afterbody heat transfer rate obtained from the above three simulations is

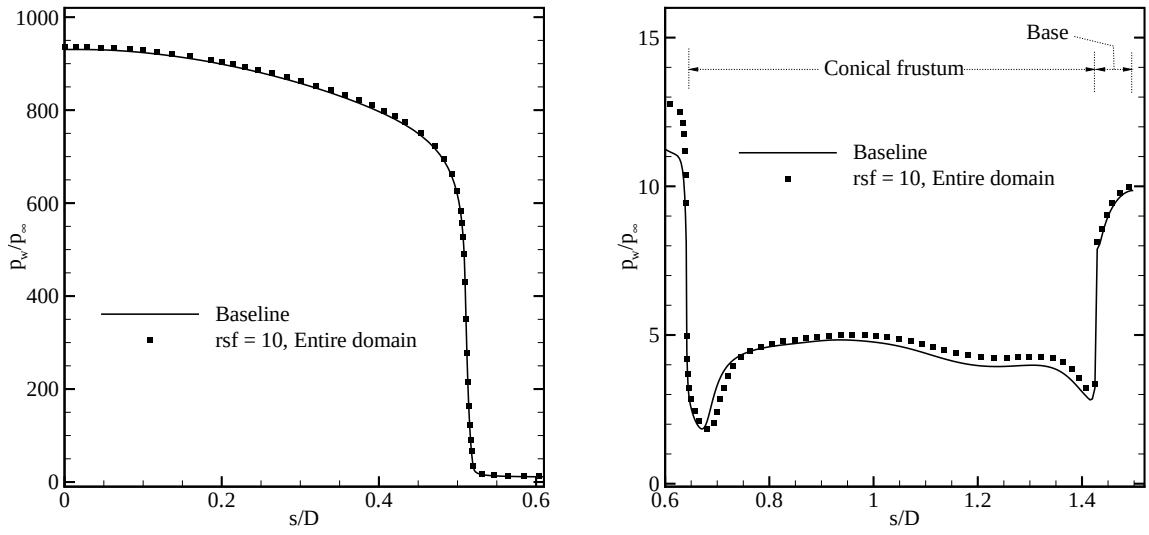

(a) (b)

Figure 5.22: Effect of increasing the rate constants in the entire domain on normalized surface pressure: (a) forebody, and (b) afterbody.

presented in Fig. 5.21(b). On the conical frustum, the higher reactivity simulations predict higher heating rate compared to the baseline solution and there is negligible difference between the two higher reactivity solutions. At the base ($s/D = 1.5$), the simulation with enhanced reactivity in the entire domain predicts higher heat transfer rate among the three solutions. As explained in Sec. 5.2.3, variation in the base heat flux is determined primarily by the boundary-layer edge conditions. Enhancing the reactivity in the entire domain significantly alters the boundary-layer edge values of gas composition and temperature and results in higher heating rate by 16% as compared to the respective baseline value. Similar effect, but to a smaller extent, is also observed when the rate constants are altered only in the boundary layer (see Sec. 5.2.3).

The boundary-layer edge effect can be clearly noticed at the shoulder ($s/D = 0.64$). The enhancement in heating rate when reactivity is increased in the entire domain, is higher than that obtained when rate constants are increased only in the boundary layer. Flow expansion around the shoulder causes exothermic recombination reactions in the outer inviscid flow. Therefore, an increased reactivity outside the boundary layer results in higher amount of heat release, elevating the boundary-layer edge temperature and thus enhancing the heat flux at the shoulder.

The wall pressure variations due to the changes in reaction rate constants are lower than those of the surface heat flux. The forebody pressure is found to increase marginally by about 50 Pa over the baseline value, when the reactivity is enhanced in entire domain (see Fig. 5.22(a)).

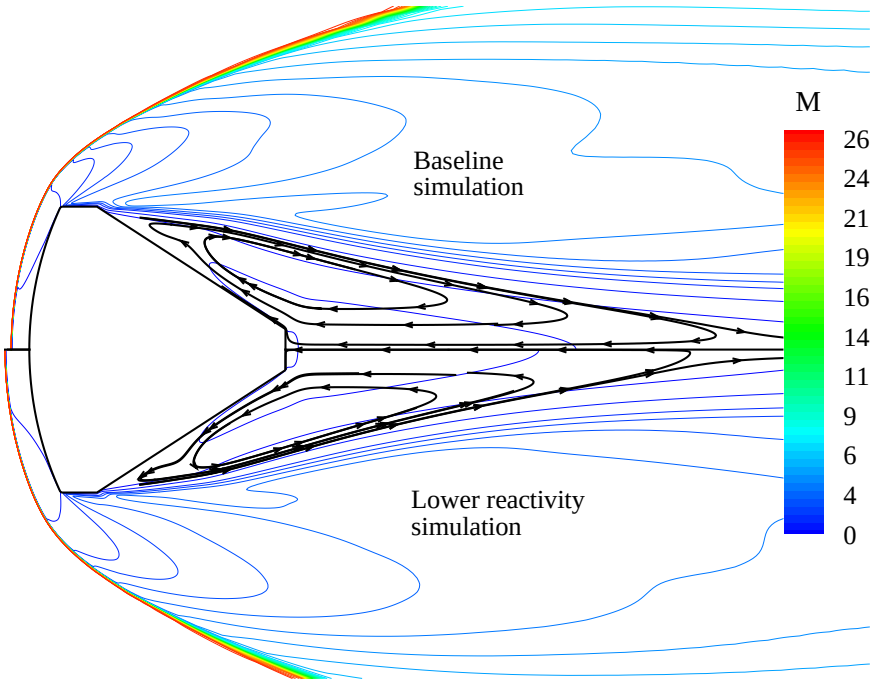

Figure 5.23: Comparison of Mach number distribution and separation bubble obtained from the baseline (top half) and lower reactivity (bottom half) simulations. Streamlines are drawn to demarcate the separation point and recirculation bubble size.

This is due to a greater amount of dissociation in the shock layer, leading to a smaller shock stand-off distance in the higher reactivity simulation. The largest variation is observed at the shoulder ($s/D = 0.62$) and is about 14.18%. This is due to the additional recombination reactions occurring in the inviscid region at the shoulder in the enhanced reactivity solution. Increasing the rate constants also yields a higher surface pressure on the afterbody (see Fig. 5.22(b)). It also results in a small delay in flow separation, as identified by the separation shock pressure rise at $s/D \simeq 0.7$. Altering the reaction rate constants only in the boundary layer does not affect the surface pressure distribution, and hence the corresponding data is not plotted in Fig. 5.22.

5.2.5 Decreased Reactivity in the Entire Domain

The Mach number distribution around the capsule in a lower reactivity simulation is compared to the baseline results in Fig. 5.23. The data in the lower half is obtained using reduced rate constants (rsf=0.1) for all five reactions in the entire computational domain, while the upper half corresponds to the baseline simulation. The lower reactivity simulation yields a larger shock stand-off distance (by 34%) due to suppression of chemical reactions in the shock layer. The

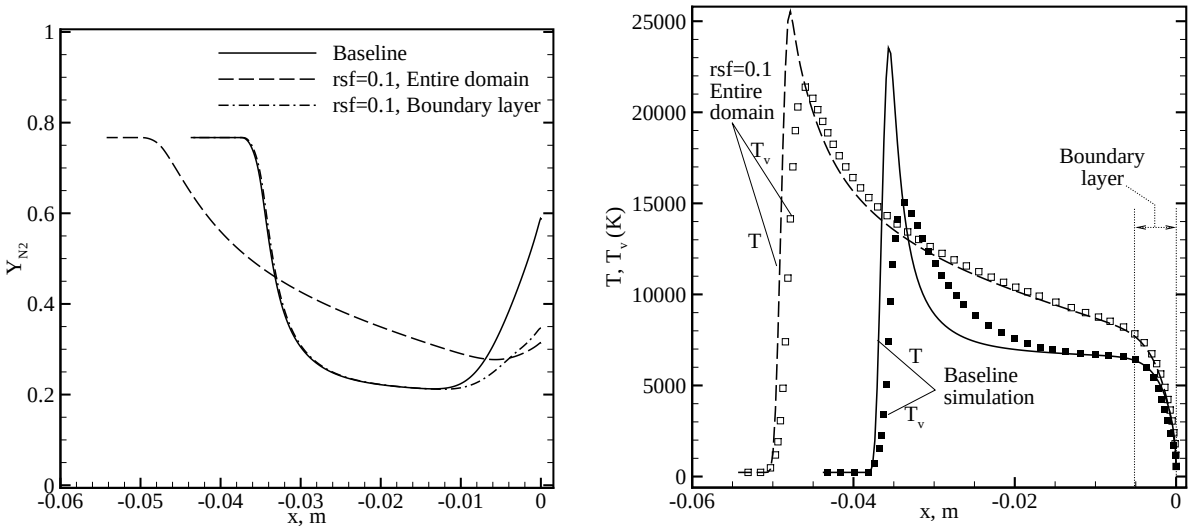

(a) (b)

Figure 5.24: Changes in (a) Y_{N_2} and (b) T and T_v along the stagnation streamline due to decreasing rate constants in the entire domain.

afterbody flow pattern looks similar in both cases. The vortex core temperature differs by about 260 K.

The N_2 mass fraction and temperature along the stagnation streamline are plotted in Fig. 5.24. The reduced rate constants decrease the amount of dissociation at the shock wave. This results in a slower decrease in Y_{N_2} at the shock and a higher peak translational temperature (by 2000 K). The peak vibrational temperature also increases by 6300 K compared to the baseline simulation. The lower reactivity solution has a higher gas temperature (by 1500 K) and an increased level of Y_{N_2} (by 0.06) at the boundary-layer edge compared to the respective baseline values.

A comparison of Y_{N_2} across the thermal boundary layer of the two solutions (see Fig. 5.24(a)) show significant differences. With the reaction rates reduced over the entire domain, Y_{N_2} reaches a value of 0.31 at the wall, and is lower than the corresponding baseline value of 0.49, but close to the Y_{N_2} obtained when the reactivity is decreased only in the boundary layer (Fig. 5.24(a)). This is due to a compensating effect of lower dissociation at the shock and a lower degree of recombination in the boundary layer, when the reaction rates are altered in the entire domain.

The forebody heat transfer rate obtained (see Fig. 5.25(a)) when the rate constants are decreased in the entire domain is lower than that of the baseline value. The heat flux at the surface is determined by the amount of heat release in the boundary layer due to recombination

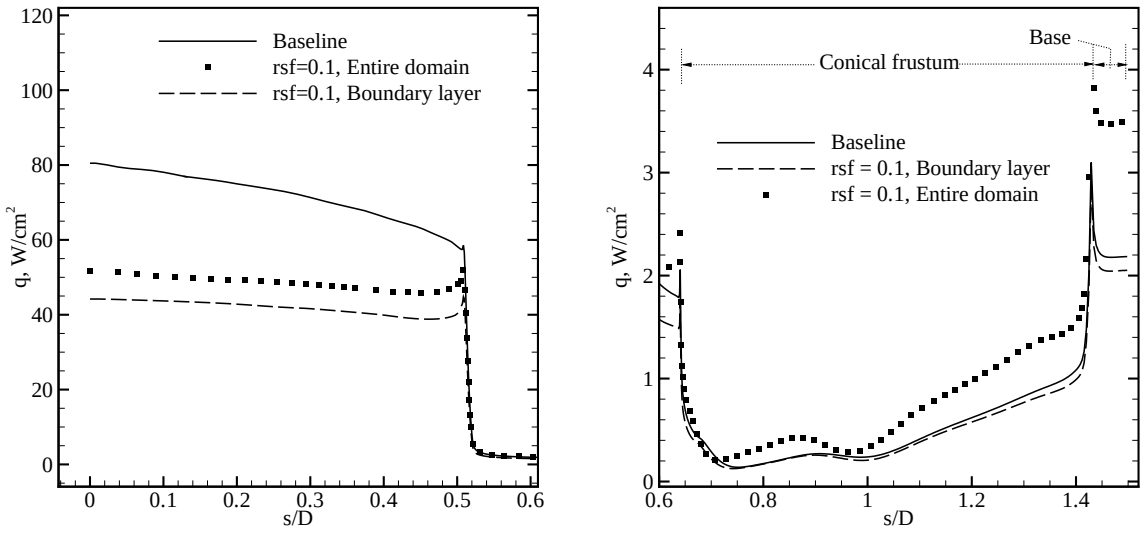

(a) (b)

Figure 5.25: Effect of decreasing the rate constants in the entire domain on heating rate: (a) forebody, and (b) afterbody

reactions and the boundary-layer edge temperature. The boundary-layer heat release is the dominant factor in this case. A lower heat release due to reduced exothermic reactions leads to a lower heat flux compared to the baseline value. On the other hand, the boundary-layer edge temperature plays a dominant role while comparing the two lower reactivity simulations, which have comparable amount of recombination in the boundary layer. A higher boundary-layer edge temperature obtained when the reaction rate constants are reduced in the entire domain results in higher heating rate compared to that obtained when reactions are suppressed only in the boundary layer.

The afterbody heating rate (see Fig. 5.25(b)) shows an interesting effect. Reducing the rate constants results in a large increase in the afterbody heat flux compared to baseline value. The heating rate increases by upto 78% at $s/D = 0.86$ on the frustum and by about 60% at $s/D = 1.5$ on the base. This is in contrast to the trends observed earlier, where reducing the reactivity leads to lower heat flux. The enhancement in the afterbody heating rate is because of changes in the forebody shock layer, where reduced rate constants leads to lower degree of dissociation and a higher gas temperature. This relatively hotter gas convects into the afterbody separation bubble resulting in a higher vortex core temperature compared to the baseline simulation. Hence the gas temperature at the edge of the thermal boundary layer is higher, leading to an enhanced heat flux to the afterbody surface. The afterbody heat flux is primarily determined

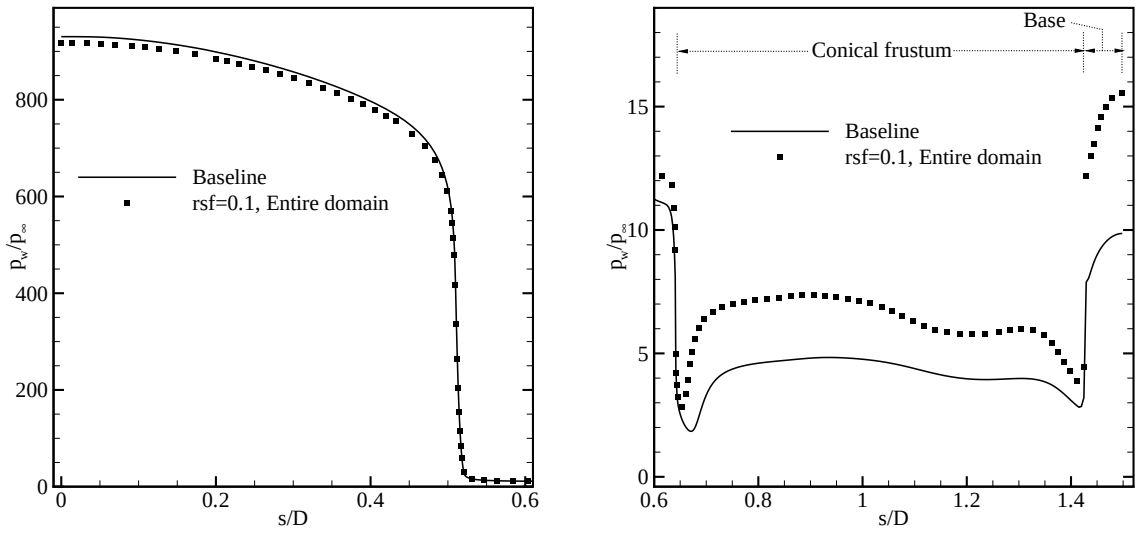

(a) (b)

Figure 5.26: Effect of decreasing the rate constants in the entire domain on normalized surface pressure: (a) forebody, and (b) afterbody

by the boundary-layer edge temperature, as there is negligible chemical activity in the vicinity of the wall on the conical frustum and base. A similar enhancement in heating rate (by 17.35%) is also observed at the shoulder ($s/D = 0.64$).

Figure 5.26 shows the surface pressure obtained from the lower reactivity and baseline simulations. There is a small reduction in the forebody wall pressure when the reaction rates are decreased. This corresponds to a lower degree of dissociation in the shock layer and a larger shock stand-off distance in the reduced reactivity simulation. By comparison, the reduced-reactivity simulation yields significantly higher pressure on the afterbody. The base stagnation point pressure is elevated by 58% as compared to the baseline value, and the pressure on the conical frustum is increased by about 50%. This is primarily due to the higher gas temperature in the separation bubble, as pointed above; the two solutions have comparable gas density in the vortex core. Reducing the reaction rate constants also move the separation point upstream.

The variations in the afterbody heat transfer rate due to a decrease in reaction rate constants is much higher than those observed on the forebody and the shoulder. Even though the afterbody density is low and the chemistry is frozen, flow separation on the afterbody plays a dominant role in determining the surface heat flux. Changes in gas properties in the forebody shock layer due to reduced reactivity is convected around the vehicle and trapped in the recirculation vortex. This non-local effect results in a large increase in the heat transfer rate on the conical frustum

and the base. Note that an increase in the afterbody heat flux in this case is opposite to the trend that is usually observed when the reaction rate constants are reduced. The afterbody pressure shows a similar variation.

5.3 Summary

A re-entry flowfield at Mach 26.2 and 70 km altitude condition is numerically simulated, and the thermo-chemistry is analyzed along the stagnation stream line. At this condition, dissociation of N_2 and O_2 occurs in the shock layer, with a partial recombination of nitrogen atoms at the wall. Mass fractions of other species remain constant in the boundary layer. Rate limiting steps in the N_2 recombination process are identified. Numerical experiments are performed by systematically varying the reaction rates and studying their effect on the computed flowfield and associated surface properties. The heat flux is most sensitive to the rate-limiting reactions, namely, the NO and O_2 recombination rates. The heat flux variations are highest in the stagnation region, and they decreases with flow expansion along the forebody and shoulder. Variation of reaction rates in the shock layer has a significant effect on the afterbody surface properties. On the afterbody, the aerothermal predictions are primarily influenced by the gas properties in the separation bubble. The changes occurring on the forebody, due to variation in rate constants, are convected into the recirculation region, which in turn alter the surface properties. Most notably, the reduced dissociation rates in the shock layer results in a large increase in the afterbody heat flux and pressure.

Chapter 6

Heating Rate Variations at 62 km Altitude

The Chapter contains analysis of heating rate variations at an intermediate altitude flight condition. A typical re-entry flight at intermediate trajectory point consists of moderately high stagnation enthalpy and relatively low density. The freestream conditions at 62 km point along AS-202 [39] re-entry trajectory are chosen as the intermediate altitude case for the present analysis; the corresponding values are listed in Table. 6.1. The stagnation enthalpy at this condition is higher than that of the 35 km condition, but lower than that of 70 km altitude. The gas density at 62 km altitude is comparable to that of 70 km condition.

6.1 Simulation Methodology

The simulation methodology and boundary conditions used are similar to that presented in Sec. 4.1.1 and hence not repeated here. Since the freestream Reynolds number based on body diameter is 6.40 $\times 10^4$, laminar simulations are performed. The grid convergence study performed at this condition is presented below.

A fine grid spacing at the nose stagnation point is found to give irregularities in the heat flux. This is similar to that observed at 70 km altitude condition. Therefore, the coarse grid 58x108, that is used at 70 km condition is chosen to alleviate non-smooth variation in the heat transfer rate. Even with the above coarse mesh irregularities in the heat flux at the nose stagnation point are found to persist. Hence grid-alignment algorithm presented in Sec. 5.1.1 is used to smoothen the heat flux on the coarse mesh. The forebody surface properties presented here, are obtained on the coarse grid 58$\times$108. A separate grid-convergence study is performed to resolve the heat flux gradients on the afterbody. A brief summary of the same is given below.

Table 6.1: Freestream conditions at 62 km altitude trajectory point.

Free-stream Conditions	
ρ_∞ (kg/m^3)	0.000281
U_∞ (m/s)	5970
T_∞ (K)	239
M_∞	19.2
$Re_{\infty D}$	6.40×10^4
H_0 (MJ/kg)	18.06

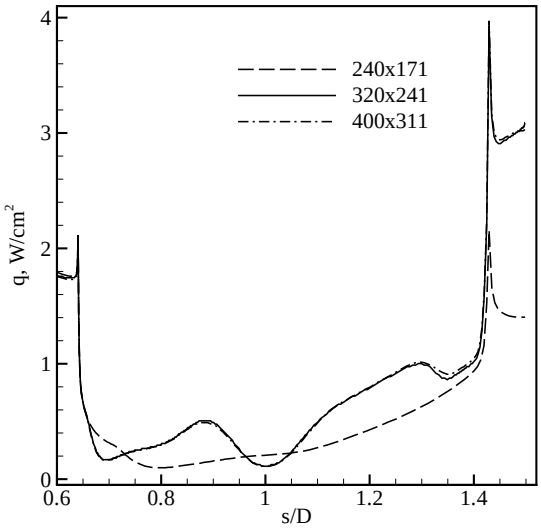

Figure 6.1: Effect of successive grid refinement on the afterbody heat flux.

6.1.1 Grid Convergence

Figure 6.1 shows afterbody heating rates obtained on three successively refined grids. The three grids shown in the figure have 100 wall-parallel points on the forebody with identical distribution, and they spanned by 140, 220 and 300 points on the afterbody. In the wall-normal direction the three grids have 171, 241 and 311 points respectively. The heat transfer rate is plotted as a function of the normalized arc length (s/D) measured from the nose stagnation point. The heat flux obtained on the 240$\times$171 grid shows a monotonic variation from s/D = 0.77 to 1.39. Solutions obtained on the other two grids show a different trend. The heating rates are marked by local peaks and dips on the conical frustum.

The afterbody flowfields obtained on the 240$\times$171 and 320$\times$241 grids are shown in Figure

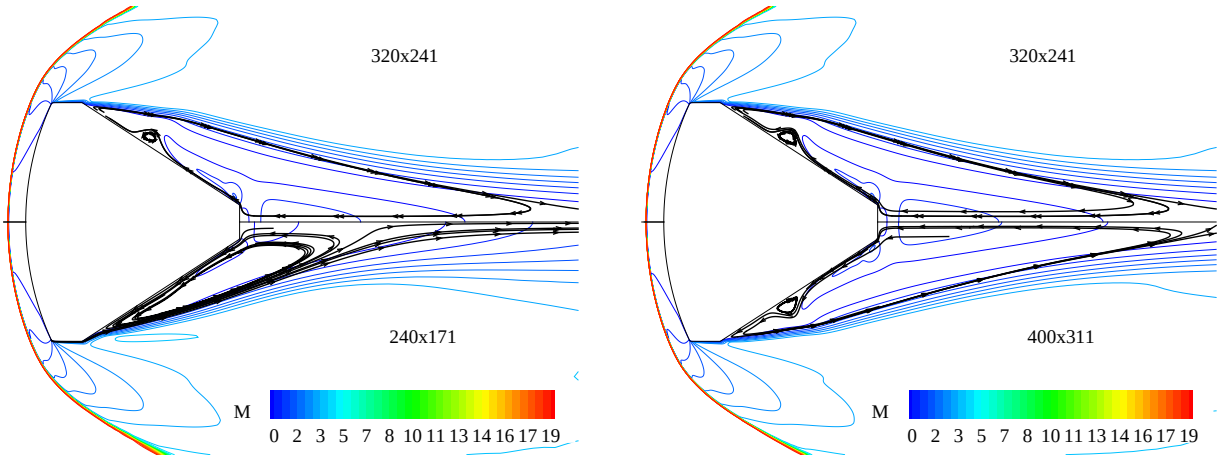

(a) (b)

Figure 6.2: Comparison of afterbody flowfields obtained on (a) 240×171 and 320×241 grids, and (b) 320×241 and 400×311 grids.

6.2(a). Significant differences can be noticed between the two solutions. The coarser grid solution is characterized by a single toroidal vortex and extends upto 0.56 times diameter of the vehicle along the axis. On the other hand, the afterbody flowfield obtained from the fine mesh, has multiple vortices. The separation bubble extends upto 1.4 times diameter of the vehicle. These multiple vortices lead to the local peaks and dips in the afterbody heating rate as shown in the Fig. 6.1.

The grid is further refined to study the sensitivity of multiple vortices to the grid point density. The solutions obtained from the two finer grids are compared in the Fig. 6.2(b). The location and number of vortices donot change with grid refinement. The afterbody flow pattern is approximately same in both the cases. As a result, the afterbody heating rates obtained from the two grids are approximately same (see Fig. 6.2(b)). The maximum deviation between the two solutions is about 5% and it is observed at $s/D \approx 1.35$. Hence 320 and 241 points in the wall-parallel and wall-normal directions respectively are taken to be sufficient to obtain a grid independent solution and it is used for the further analysis.

6.2 Results

A brief description of the computed re-entry flowfield and surface properties is given below. Next, the details of the thermo-chemical state of the gas and chemical reactions in the boundary

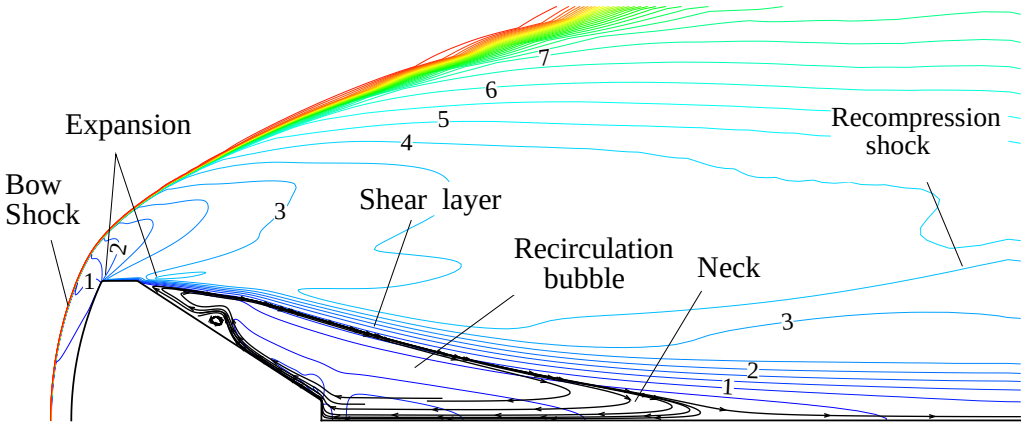

(a)

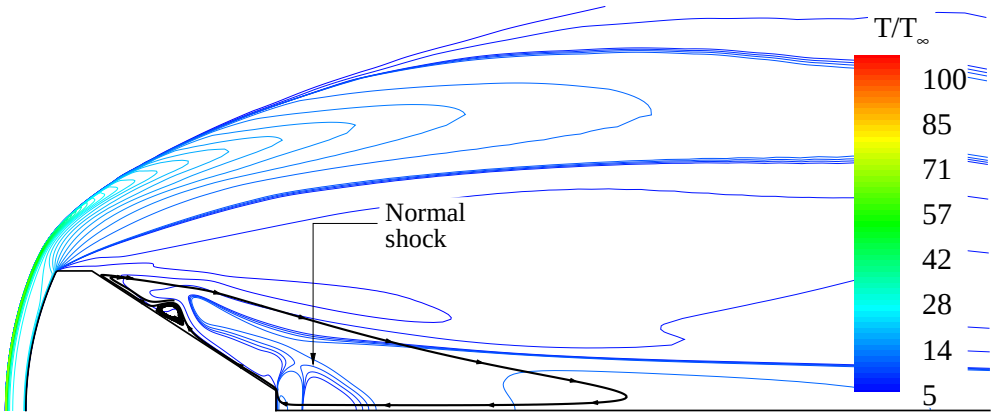

(b)

Figure 6.3: Computed flowfield around a re-entry capsule at Mach 19.2: (a) Mach number and (b) non-dimensional temperature distribution. Representative streamlines are shown on the afterbody to identify the recirculation bubble.

layer are presented. The effect of variation in the chemical reaction rates on heating predictions is explained subsequently.

The computed flowfield in terms of Mach number distribution is shown in Fig. 6.3(a). The prominent features such as bow shock and flow expansion at the corners can be easily identified. The flow on the entire forebody is subsonic with Mach number approaching unity close to the first expansion corner. The post-shock temperature in the nose stagnation region is about 5800 K. Flow expansion at the first corner results in decrease of temperature to 2500 K. Further expansion around the second corner decreases the temperature to about 1000 K.

The boundary layer remains attached on the forebody and shoulder, and separates immediately downstream of the second corner. The recirculation bubble extends up to about 1.45

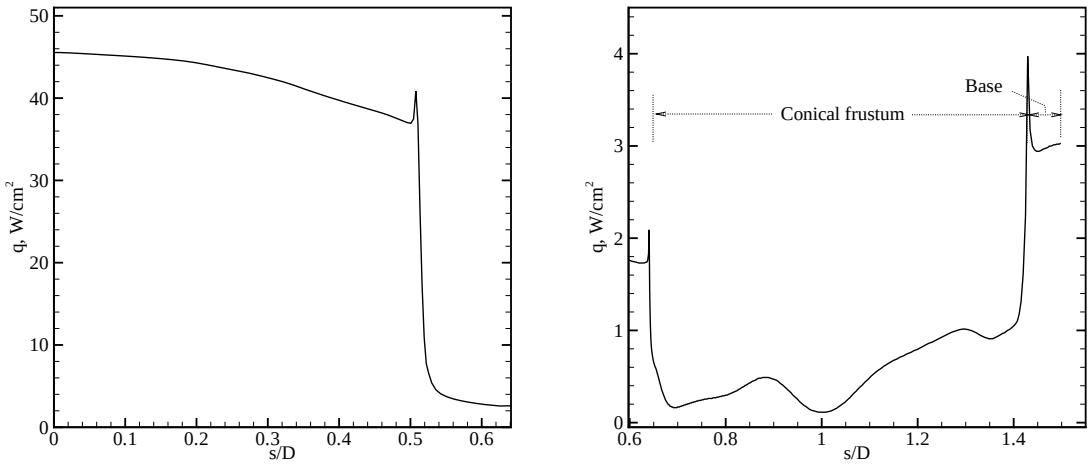

(a) (b)

Figure 6.4: Variation of (a) temperatures and (b) mass fraction of species in the thermal boundary layer at the nose stagnation point.

diameters downstream of the base. A secondary flow separation is observed on the conical frustum. Hence a smaller separation bubble forms at the secondary flow separation point. The gas temperature in the vortex core is about 1800 K. The shear layer enclosing the recirculation region coalesce at the neck, and a recompression shock wave is generated. The temperature of the gas in the neck region is close to 2500 K. The temperature in the inviscid region outside the wake is about 1100 K and the Mach number there is about 4.2. The reversed flow along the axis becomes supersonic, and a normal shock is formed at the base (see Fig. 6.3(b)) to slowdown the flow to a subsonic Mach number. Another supersonic pocket is also observed at the afterbody expansion corner.

Figure 6.4(a) shows the computed heat transfer rate on the forebody surface as a function of the normalized arc-length (s/D) measured from the nose of the vehicle. The heat transfer rate gradually decreases on the forebody from a maximum value of 47 W/cm^2 at the nose stagnation point. The heating rate falls rapidly at the expansion corner ($s/D = 0.52$) as the gas temperature drops due to flow expansion. The afterbody heat transfer rate is shown in Fig. 6.4(b), where the extent of the conical frustum and the base are identified. The expansion corners are marked by local peaks in the heat flux. The secondary flow separation causes a local minimum in the heating rate at $s/D \approx 1$. The base stagnation point heat flux is 3.02 $\mathrm{W/cm^2}$, which is 6.42% of the nose stagnation point value.

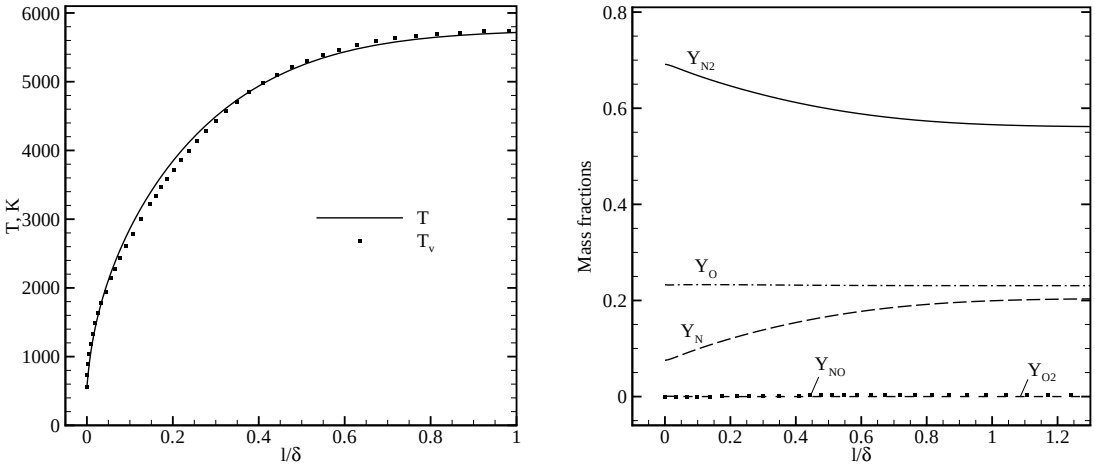

(a) (b)

Figure 6.5: Variation of (a) temperatures and (b) mass fraction of species in the thermal boundary layer at the nose stagnation point.

6.2.1 Thermo-Chemistry

Figure 6.5(a) shows the variation of gas temperature in the thermal boundary layer at the nose stagnation point. Local thermal boundary layer thickness is used to non-dimensionalize the wall normal distance. Hence $l/\delta = 0$ and 1 represent the wall and boundary-layer edge respectively. Flow is in thermal equilibrium ($T \simeq T_v$) at the edge of the boundary layer with both translational and vibrational temperatures around 5700 K. In the boundary layer both temperatures decrease to reach 553.5 K at the wall due to isothermal condition.

The freestream gas is composed of oxygen and nitrogen molecules with mass fractions of 0.23 and 0.77 respectively. The high temperature of the gas in the shock layer causes complete dissociation of oxygen molecules and partial dissociation of nitrogen molecules. As a result, mass fraction of N_2, N and O species attain values of 0.57, 0.2 and 0.23 respectively at the edge of the boundary layer (see Fig. 6.5(b)). Concentrations of the remaining two species are negligible. The decrease of gas temperature in the boundary layer initiates chemical reactions. Therefore Y_{N_2} increases to 0.69 at the wall with a corresponding decrease in Y_{N}. However, mass fractions of atomic and molecular oxygen and NO remain same throughout the boundary layer.

The above change in gas composition is due to N_2 recombination through R_3-R_4 and R_2-R_5-R_4 reaction mechanisms as identified in Sec. 5.2.1. Figure 6.6 depicts the chemical reaction rates in the boundary layer. The first mechanism (R_3-R_4) consists of recombination of NO molecules: N + O $\rightarrow$ NO; and exchange reaction: NO + N $\rightarrow$ N_2 + O. It is active for

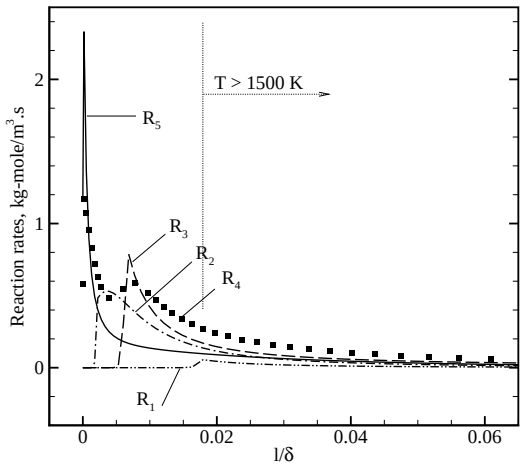

Figure 6.6: Variation of reaction rates in the thermal boundary layer at the nose stagnation point

$l/\delta > 0.005$. It is noticed that $R_3 \approx R_4$ in this region. Therefore the net effect of these two reactions is 2 N $\rightarrow$ N_2. The reaction rate R_2 has non-negligible values for $l/\delta \leq 0.02$ and attains a peak value of 0.5 at $l/\delta = 0.04$. The second mechanism (R_2-R_5-R_4) is active in the immediate vicinity of the wall.

The R_2-R_5-R_4 mechanism is initiated by oxygen recombination: O + O + M $\rightarrow$ O_2 + M, and followed by the two exchange reactions: O_2 + N $\rightarrow$ NO + O and NO + N $\rightarrow$ N_2 + O. The overall effect is formation of N_2. Thus, the two reaction sequences constitute chain mechanisms, where O_2 and NO molecules act as catalyst in the recombination of N atoms. There is no significant effect on O_2, O and NO mass fractions. The chain reactions will cease when nitrogen recombination is complete. In the absence of N atoms, only recombination of oxygen will occur. At the chosen conditions, N atoms are not completely depleted, and hence the concentrations of O_2, O and NO do not change.

6.2.2 Altered Reactivity in the Entire Domain

Simulations are performed by varying the rate constants in the boundary layer and in the entire domain independently. The trends observed when the rate constants altered only in the boundary layer are similar to those observed at the higher altitude condition. For the sake of brevity, these results are not presented here. The results described below are obtained from the altered reactivity simulations, where the rate constants are varied in the entire domain.

Figure 6.7 compares the flowfield solutions obtained from the altered reactivity simulations with that of the baseline simulation. The forebody solutions are identical except for a

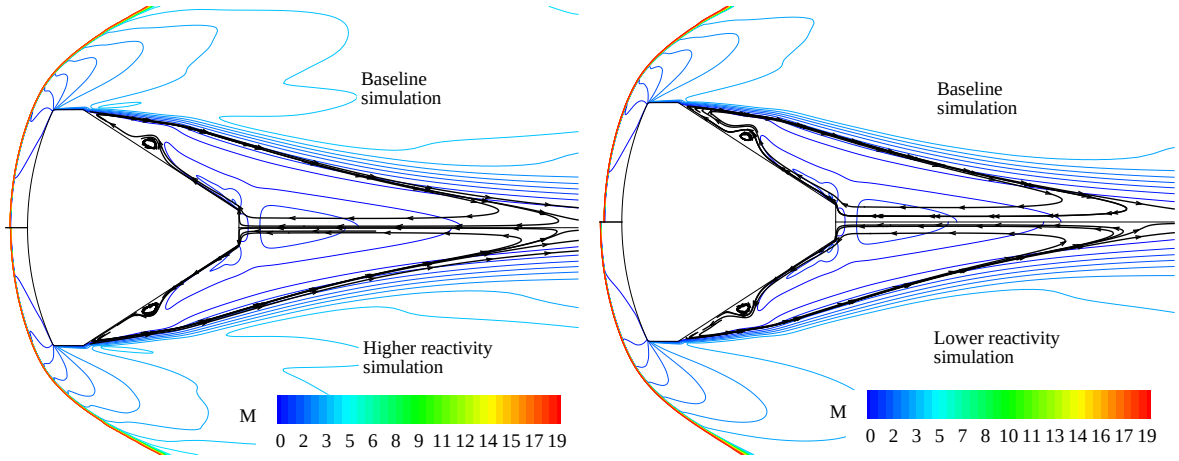

(a) (b)

Figure 6.7: Comparison of computed Mach number distribution around the capsule obtained from the baseline and (a) higher reactivity, and (b) lower reactivity simulations. Representative streamlines are shown on the afterbody to identify the recirculation bubble.

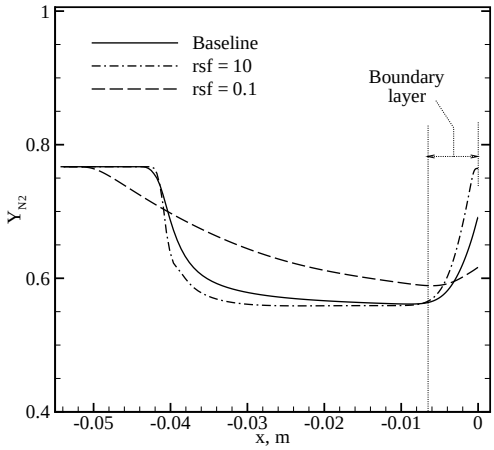

Figure 6.8: Variation of Y_{N_2} along the stagnation streamline due to variation in rate constants. The flow is from left to right and the wall is located at $x = 0$.

difference in the predicted shock stand-off distance. Increasing the reactivity reduces the shock stand-off distance by 3%, on the other hand reducing the rate constants increases the stand-off distance by 23%. The pattern of afterbody flowfield in both the higher and lower reactivity solutions is similar to that of the baseline solution. That is, variations in the rate constants do not alter the size and number of vortices on the afterbody at this condition.

Figure 6.8 plots variation of Y_{N_2} along the stagnation streamline. Mass fraction of N_2 obtained from the lower reactivity solution shows a different trend compared to those of the

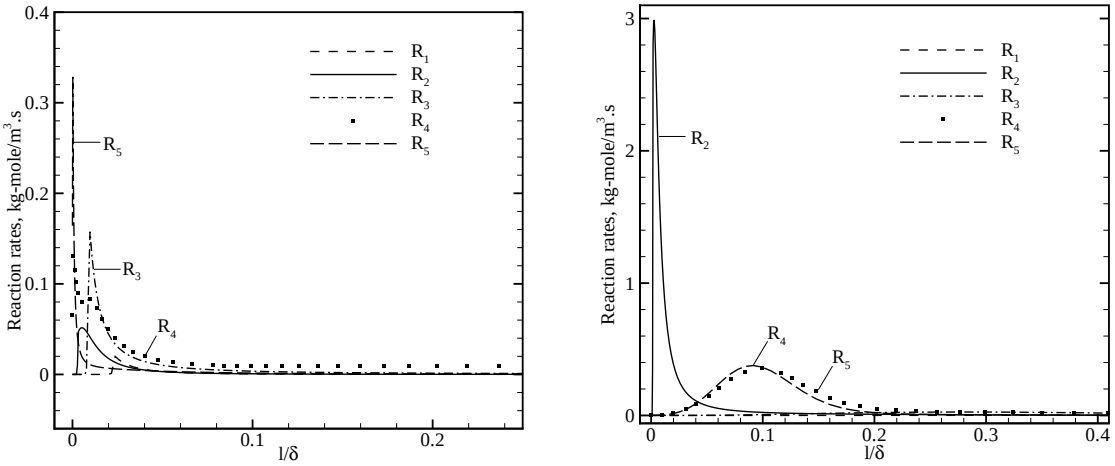

Figure 6.9: Variation of reaction rates at the nose stagnation point: (a) lower reactivity simulation, and (b) higher reactivity simulation.

baseline and higher reactivity solutions. Rapid decrease of Y_{N_2} is not observed at the shock wave and its corresponding value is considerably higher than that of the baseline value. Hence the degree of dissociation is significantly lower and this increases the shock stand-off distance by 23%. Further Y_{N_2} decreases at a slower rate compared to the other two solutions in the shock layer, and it doesn't reach chemical equilibrium in the entire shock layer. Its value at the boundary-layer edge is higher than that of the baseline solution. The higher reactivity and baseline solutions show a sharp decrease in Y_{N_2} at the shock wave. However the reduction in Y_{N_2} is marginally higher in rsf = 10 simulation. Hence the dissociation level is approximately same in the both solutions. As a result, the difference between the shock stand-off distances predicted from the two solutions is not significant. Mass fraction of N_2 obtained from the higher reactivity simulation approximately remains constant in the shock layer so that its value matches with that obtained from the baseline solution at the boundary-layer edge.

Figure 6.8 shows variation of Y_{N_2} in the boundary layer also. Mass fraction of N_2 obtained from the higher reactivity simulation increases at a faster rate than the other two solutions. As a result Y_{N_2} reaches a higher value at the wall compared to that of the baseline value. An opposite trend is observed in the lower reactivity simulation. Mass fraction of N_2 increases by a small amount, and its value at the wall is lower compared to that of the baseline value. The above variations in Y_{N_2} is explained with the aid of Fig. 6.9 which shows the reaction rates in the boundary layer, that is obtained from the altered reactivity simulations.

The variation of reaction rates at the nose stagnation point, when the rate constants are reduced in the entire domain is shown in Fig. 6.9(a). The variation of reaction rates is similar to that observed in the baseline simulation (see Fig. 6.6). However the magnitude of all reaction rates decreases significantly compared to their respective baseline values. Both R_3-R_4 and R_2-R_5-R_4 mechanisms contribute to N_2 recombination. Amount of N_2 formed in the near-wall region is lower due to decrease in the magnitude of reaction rates. As a result, the wall value of Y_{N_2} is lower than that observed in the baseline solution (see Fig. 6.8). As N_2 recombination has not approached completion, mass fractions of O_2, NO and O do not vary in the boundary layer, similar to that observed in the baseline simulation.

The reaction rate pattern in the higher reactivity simulation is different from that observed in the baseline simulation. The magnitudes of reaction rates are higher compared to their respective baseline values. The dominant N_2 recombination mechanism is R_5-R_4, and it is active for $0.025 < l/\delta < 0.2$. Both reaction rates have a peak value of about 0.38 kg-mole/m^3.s at $l/\delta \approx 0.1$. It can be noticed that $R_5 \approx R_4$ in this region, therefore the net effect is 2 N$\rightarrow$ N_2. This mechanism leads to complete recombination of N_2 as can be noticed from Fig. 6.10. The mass fraction of N reduces to negligible values at the wall, and correspondingly Y_{N_2} reaches a value of 0.76 at the wall (see Fig. 6.8). Reaction 3 is not active in the entire boundary layer and therefore contribution of R_3-R_4 mechanism to N_2 recombination is negligible.

Recombination of O_2 is significant for $l/\delta < 0.07$ and its rate attains a peak value of 3 kg-mole/m^3.s very close to the wall $l/\delta \approx 0.003$. As N atoms are completely depleted, the newly formed O_2 molecules accumulates in the near-wall region, which result in increase of Y_{O_2}. It reaches a value of 0.05 at the wall (see Fig. 6.10). The newly formed O_2 molecules diffuse away from the wall. This diffusion process provides the necessary oxygen molecules required for R_5-R_4 mechanism of N_2 recombination in the region $0.025 < l/\delta < 0.2$. The other difference noticed is that, the reaction rates spreads over 20% of boundary-layer thickness, where as in the baseline simulation the chemistry is confined to 5% of boundary-layer thickness. Thus the increased reactivity results in recombination reactions to the larger extent than that observed in the baseline simulation, and increases the wall values of Y_{N_2} and Y_{O_2} compared to their respective baseline values.

The effect of varying the rate constants on shock-layer gas temperature is shown in Fig. 6.11. The difference in shock stand-off distance can be clearly noticed among the three solutions. The peak temperature in the higher reactivity simulation is lower by 1790 K compared to that

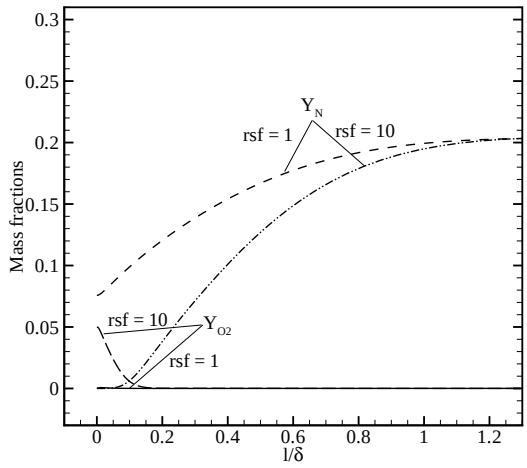

Figure 6.10: Variation of Y_{O_2} and Y_N at the nose stagnation point in the higher reactivity simulation.

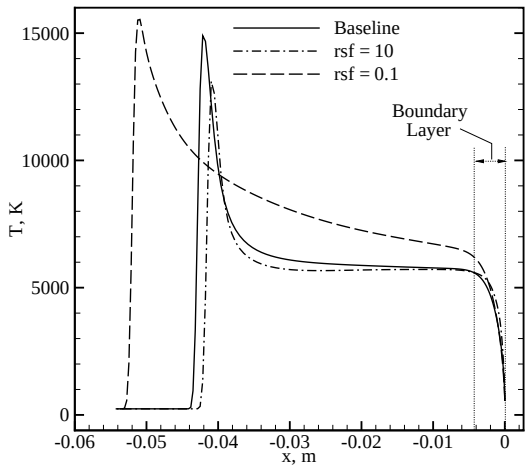

Figure 6.11: Gas temperature along the stagnation streamline obtained from the baseline and altered reactivity simulations.

of baseline value. The difference between the gas temperatures obtained from the two solutions persist in the shock layer. However both the baseline and higher reactivity solutions approach approximately same temperature value at the boundary-layer edge. The peak temperature obtained from the lower reactivity simulation is higher by 615 K compared to that of the baseline value. This is essentially due to a lower amount of dissociation at the shock wave. The temperature difference between the two solutions persist in the entire shock layer. The temperature of the gas at the boundary-layer edge is higher by 604 K compared to the respective baseline value. Thus the entire shock layer in the rsf = 0.1 solution is hotter than the other two solutions.

Table 6.2: Contribution of $\triangle\kappa/\kappa$ and $\triangle T_2/(T_2-T_w)$ to $\triangle q/q$ in the higher (rsf = 10) and lower (rsf = 0.1) reactivity cases at the nose stagnation point.

% change	rsf = 10	rsf = 0.1
$\triangle\kappa/\kappa$	-3.50	5.70
$\triangle T_2/(T_2-T_w)$	38.10	-31.55
$\triangle q/q$	33.40	-27.65

Forebody Heating Rate

Forebody heating rate computed from the baseline and altered reactivity solutions is shown in Fig. 6.12. Increasing the reactivity leads to higher heating rate on the entire forebody compared to the baseline prediction. As explained above, an increase in the rate constants promotes the recombination reactions. The additional heat release due to exothermic reactions enhances the surface heat flux. An opposite trend is observed in the reduced reactivity simulation. Lower dissociation in the shock layer leads to a higher boundary-layer edge temperature compared to the baseline value (see Fig. 6.11). This tends to enhance the surface heating rate, but is countered by the more dominant boundary layer effect. The extent of recombination in the boundary-layer is significantly lower. The heat release in the near-wall region is therefore lower and it leads to a lower heating rate compared to the baseline value.

The change in the heat flux due to varying reaction rates can, be expressed in terms of the changes in the thermal conductivity and the gas temperature adjacent to wall T_2.

$$\frac{\triangle q}{q} = \frac{\triangle \kappa}{\kappa} + \frac{\triangle T_2}{T_2 - T_w} \tag{6.1}$$

where higher-order terms are neglected. A budget of Eq. (6.1) for the stagnation point heat flux for the higher and lower reactivity simulations is shown in Table 6.2, where the changes are calculated with respect to the baseline simulation values. Enhancing the reactivity (rsf = 10) increases the gas temperature in the near-wall region by 38%, and the gas temperature decreases by about 32% when the reaction rates are reduced (rsf = 0.1).

At the current boundary-layer conditions, the relative magnitude of thermal conductivity among the species is:

$$\kappa_{\mathrm{N}} > \kappa_{\mathrm{O}_2} > \kappa_{\mathrm{NO}} > \kappa_{\mathrm{N}_2} > \kappa_{\mathrm{O}} \tag{6.2}$$

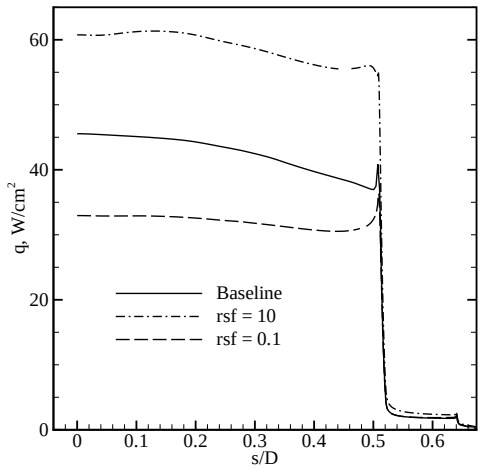

Figure 6.12: Comparison of forebody heating rate obtained from the baseline and altered reactivity simulations.

Molecular nitrogen has lower thermal conductivity than its atomic counterpart, where as molecular oxygen has higher thermal conductivity than atomic oxygen. An increase in the mass fraction of N_2 due to enhanced recombination reactions (rsf = 10) tends to decrease the mixture conductivity. On the other hand, an increase in Y_{O_2} has tendency to increase the thermal conductivity. These two effects compete each other resulting in a small decrease in the mixture conductivity ($\approx 4\%$). On the similar note, lowering reaction rates leads to increase in the conductivity by 6%.

It is observed that the changes in conductivity counter those in the near-wall gas temperature. The heat release or the temperature effect is found to be the dominant contribution to the surface heat transfer rate. The net effect is an enhancement in the stagnation point heating rate by 33% when the rate constants are increased, and a reduction in the heat flux by 28% when the rate constants are decreased. Note that the changes in thermal conductivity and temperature do not match the net change in q as per Eq. (6.1), because of the contributions of higher-order terms that are neglected in the analysis.

Afterbody Heating Rate

The afterbody heating rates obtained from the three simulations is shown in Fig. 6.13. In the later part of the conical frustum (for $s/D > 1$) the heat flux obtained from the increased reactivity solution is higher than that of the baseline solution. At the base stagnation point, the heating rate is higher by 10%.

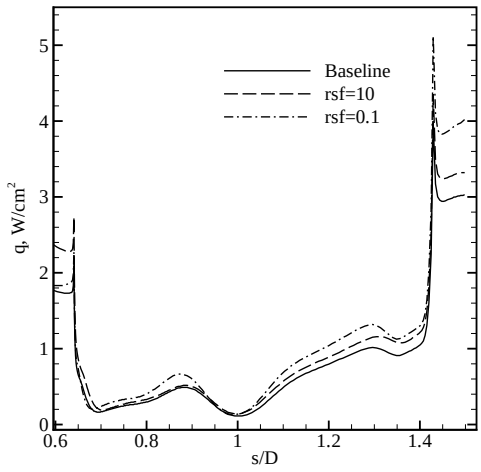

Figure 6.13: Comparison of afterbody heat flux obtained from the baseline and altered reactivity simulations.

The lower reactivity heating rate values are higher than those of the baseline and higher reactivity values on the entire afterbody. The enhancement in the afterbody heating rate is because of the changes in the forebody shock layer, where the reduced rate constants leads to lower degree of dissociation and a higher gas temperature. This relatively hotter gas convects into the afterbody separation bubble, and results in a higher vortex core temperature compared to the baseline solution. Hence, the gas temperature at the edge of the thermal boundary layer is higher. In the absence of chemical reactions occurring in the vicinity of the wall, the afterbody heat flux is primarily determined by the boundary-layer edge temperature. The higher boundary-layer edge temperature in case of lower reactivity simulation, leads to an enhanced heat flux to the afterbody surface. A similar enhancement in the heating rate is also observed at the shoulder ($s/D = 0.64$).

Surface Pressure

The changes in the forebody surface pressure due to the variation in rate constants is much lower than that of the forebody heat flux. Pressure obtained from the higher reactivity simulation is approximately same as that of baseline value (see Fig. 6.14(a)). However lowering the rate constants leads to a reduction in pressure by 211 Pa. This is due to a lower degree of dissociation in the shock layer and a larger shock stand-off distance. The variations in the afterbody surface pressure are shown in Fig. 6.14(b). The variations between the higher reactivity and baseline solutions are lower than 4%. The reduced-reactivity simulation yields significantly

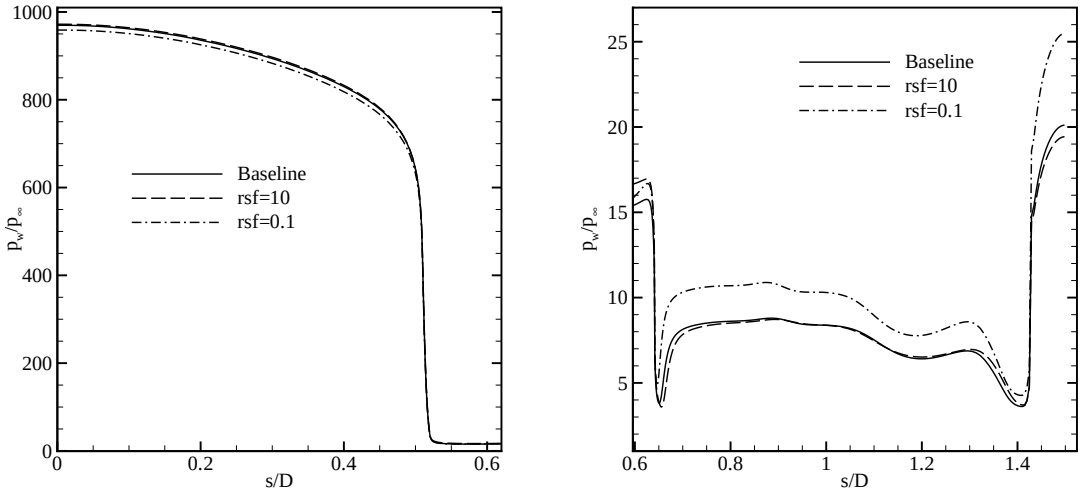

(a) (b)

Figure 6.14: Effect of varying the reaction rates on normalized surface pressure (a) forebody, and (b) afterbody.

higher pressure on the entire afterbody. The base stagnation point pressure is elevated by 26% as compared to the baseline value. This is primarily due to the higher gas temperature in the separation bubble, as pointed above; the two solutions have comparable gas density in the vortex core.

6.3 Summary

The flowfield over FIRE II re-entry capsule at Mach 19.2 and 62 km altitude condition is computed. Thermo-chemistry along the stagnation streamline is analyzed. The chemistry in shock layer and boundary layer is similar to that occur at the 70 km altitude condition. Numerical simulations are performed by varying the rate constants, to study their effect on the computed flowfield and surface predictions. Similar to 70 km condition, at this trajectory point also, the heat flux changes are influenced by the NO and O_2 recombination rate constants. Enhancing the reactivity leads to complete recombination of N atoms and partial recombination of O atoms in the boundary layer. This increases the heat flux by 33% at the nose stagnation point. Lowering the rate constants leads to significant enhancement in surface heating and pressure on the entire afterbody.

Chapter 7

Variation with altitude

The thermo-chemistry in the flowfields at 35, 62 and 70 km are critically analyzed in this Chapter. This is to bring-out the effect of altitude on the thermo-chemistry and degree of non-equilibrium in the flowfield. The heating rate variations at the nose stagnation point for the three trajectory points are thoroughly analyzed to understand the role of density and stagnation enthalpy on the heating rate variations.

7.1 Chemical Reactions

7.1.1 Shock-layer Chemistry

The onset temperature for O_2 dissociation is around 2000 K. Post shock temperature of about 2000 K is observed for flight velocities near 2 km/s. At temperatures above 4000 K most of the oxygen molecules are dissociated. This corresponds to a velocity of about 4 km/s. At the lowest enthalpy condition, the freestream velocity is 5 km/s, and oxygen is completely dissociated in the shock layer. The mass fraction Y_{O_2} is 1.16×10^{-3} at the edge of the boundary layer. At higher enthalpies, the dissociation level of O_2 is much higher. Its mass fraction is 6.0×10^{-5} at the intermediate enthalpy condition, and decreases to 1.0×10^{-5} in the highest enthalpy simulation. Although the magnitude of Y_{O_2} is negligible at these high enthalpy conditions, O_2 plays a significant role in the boundary layer chemistry, as explained below.

Dissociation of N_2 molecules begins at about 4000 K. Nitrogen dissociation can be observed in the shock layer for flight velocities above 4 km/s. Mass fraction of N atoms in the shock layer for the 35km simulation in 0.05. It increases to 0.20 at the intermediate altitude

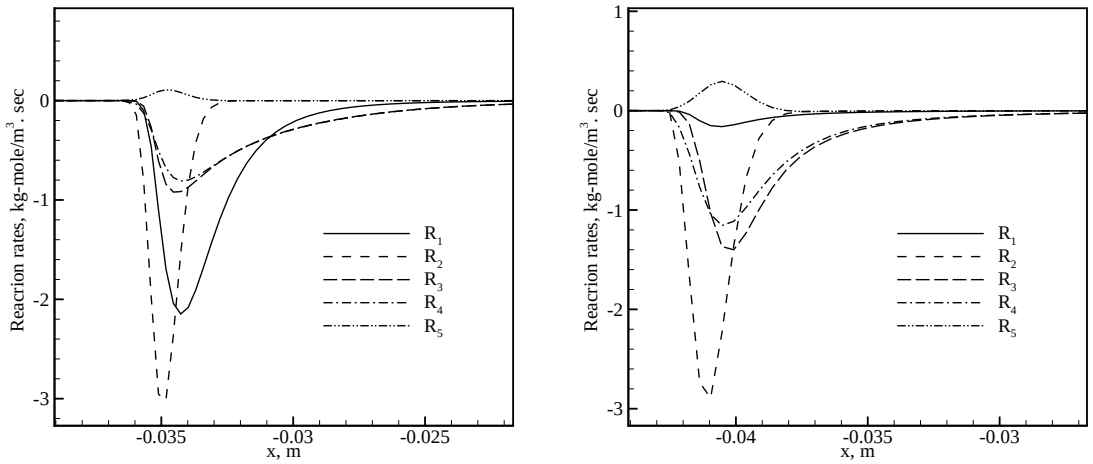

Figure 7.1: Reaction rates at the shock wave along the stagnation streamline for (a) 70 km and (b) 62 km.

condition and further to 0.54 at the highest altitude simulation. The corresponding N_2 dissociation levels for the three trajectory points are 6.5%, 25.97% and 70.13% respectively. The dissociation level is calculated from $Y_{\mathrm{N}}/Y_{\mathrm{N}_2} \times 100$.

Dissociation of oxygen primarily occurs via reaction: O_2 + M $\rightarrow$ 2 O+ M. The maximum reaction rate at the shock wave corresponds to R_2 in both the 70 km and 62 km altitude simulations (see Fig. 7.1) and its magnitude is comparable at both the altitudes. Dissociation of N_2 can happen through reaction (1), or (4), or both. The activation energy of Reaction (1) is higher than that of Reaction (4). The corresponding characteristic reaction temperatures are 113200 K and 38400 K respectively. At moderate enthalpies, for example, at 62 km (18 MJ/kg), majority of N_2 dissociation occurs through Reaction (4). This can be noted in Fig. 7.1(b), which compares the reaction rates at the shock wave in the 62 km altitude solution. As the enthalpy increases further, R_1 contribution to N_2 dissociation increases, as can be seen in the higher altitude simulation (see Fig. 7.1(a)). For this condition, with a stagnation enthalpy of 32 MJ/kg, the magnitude of R_1 is higher than that of R_4. This is opposite to that observed in the intermediate enthalpy solution.

7.1.2 Temperature Variation with Altitude

The variation of gas temperature in the shock layer at the three altitudes is shown in Fig. 7.2(a). As the altitude increases, the Mach number and stagnation enthalpy of the flow increases and

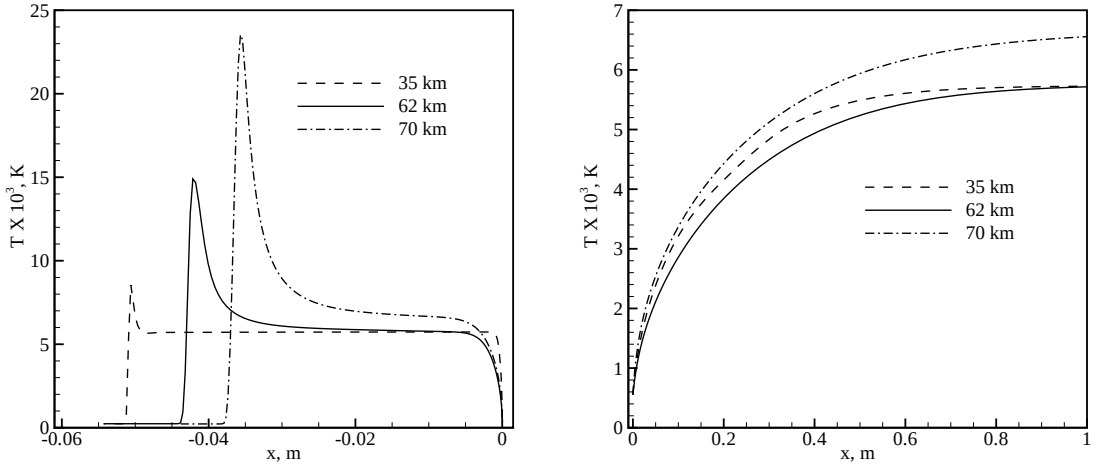

Figure 7.2: Comparison of gas temperatures for the three altitudes in (a) shock layer and, (b) boundary layer.

the shock stand off distance correspondingly decreases. The increase in freestream velocity also results in a higher peak temperature at the shock wave (see Fig. 7.2(a)). The peak temperature at the highest altitude condition, corresponding to a freestream velocity of 8 km/s is 24000 K. The corresponding values for the intermediate and low altitude conditions are 15000 K and 8500 K respectively.

Temperature of the gas decreases rapidly due to endothermic dissociation reactions behind the shock wave and approaches comparable values in the later part of the shock layer in the three solutions. The boundary layer edge temperature in the 70 km altitude simulation is 6556 K, where as it is 5715 K and 5726 K in the 60 km and 35 km altitude solutions respectively. The temperature of the gas decreases in the boundary layer to the isothermal wall value of 553.3 K. This initiates recombination of N and O atoms. The variation in gas temperature in the boundary layer is comparable for the three cases (see Fig. 7.2(b)), but the boundary layer chemistry is different due to differences in the gas composition at the edge of the boundary layer. The concentrations of the species at the boundary layer edge is determined by the shock layer chemistry, which is in turn a function of the stagnation enthalpy of the flow.

7.1.3 Boundary-layer Chemistry

The boundary layer chemistry is dominated by recombination reactions, and the dominant reactions are identified for different altitudes and stagnation enthalpy conditions. Similar to N_2

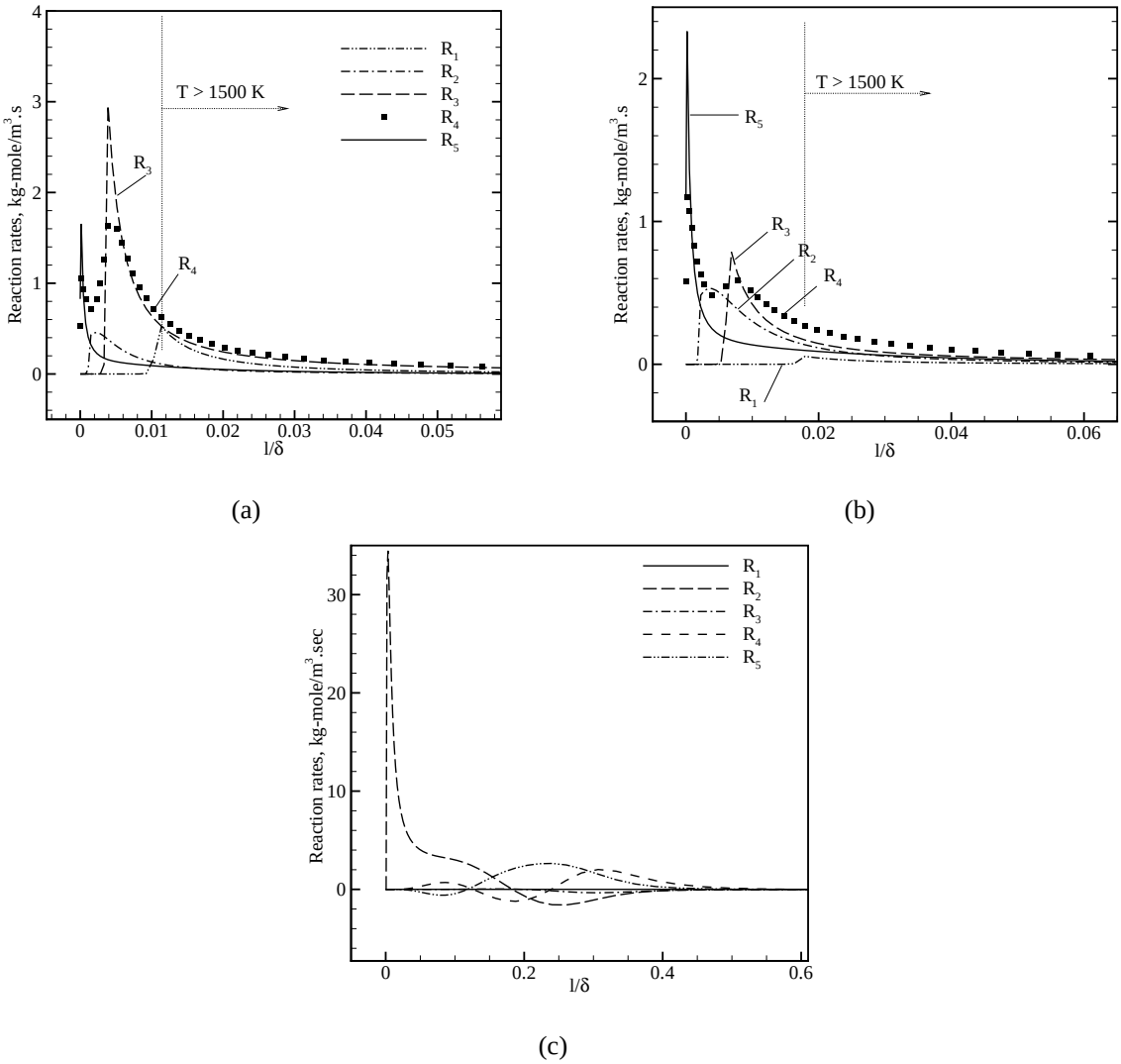

Figure 7.3: Variation of reaction rates at the nose stagnation point (a) 70 km, (b) 62 km, and (c) 30 km.

dissociation, the recombination of N atoms can occur via backward reactions (1) and (4), and their relative contributions are compared. In the 70 km simulation, we observe that R_1 and R_4 are of comparable magnitude in the boundary layer for temperatures above 1500 K (see Fig.7.3(a)). On the other hand, R_1 is much lower than R_4 for the same temperature range at 60 km altitude. The reasons for this trend are explained below.

The backward reaction (1) is a three body recombination: N + N + M $\rightarrow$ N_2 + M, with N_2, N and O as the primary collision partners. The reaction rate is approximated as $R_1 \approx C_{\mathrm{N}} C_{\mathrm{N}} k_{b_1} C_{\mathrm{M}}$, where the forward reaction rate is neglected. As the flight altitude and the stagnation enthalpy of the flow decreases, the N_2 dissociation level in the shock layer is reduced.

This results in a lower concentration of N atoms at the boundary layer edge. As $R_1 \propto C_{\mathrm{N}}^2$, a lower value of C_{N} leads to a decrease in the magnitude of R_1. The peak value of R_1 at 62 km altitude (0.02 kg-mole/m^3.sec) is therefore much lower than the corresponding value (0.52 kg-mole/m^3.sec) in the 70 km simulation. At 35 km altitude, reaction (1) is not active in the boundary layer (see Fig. 7.3(c)).

The backward reaction (4) is N + NO $\rightarrow$ N_2 + O and the reaction rate can be approximated as $R_4 \approx C_{\mathrm{N}} C_{\mathrm{NO}} k_{b_4}$. As earlier, the contribution of the forward reaction is neglected in the boundary layer. With a decrease in altitude and stagnation enthalpy, the level of N_2 and O_2 dissociation in the shock layer reduces. It is observed that this results in an increase of C_{NO} at the boundary layer edge. As $R_4 \propto C_{\mathrm{N}} C_{\mathrm{NO}}$, a decrease in C_{N} due to lower enthalpy is countered by an increase in C_{NO}, resulting in comparable magnitudes of R_4 in the three simulations. The peak values of the reaction rate are 1.7 kg-mole/m^3.s, 1.2 kg-mole/m^3.s and 2.0 kg-mole/m^3.s in the 70 km, 62 km and 35 km altitude simulations respectively.

The trends in R_1 discussed above holds for temperature above 1500 K in the boundary layer. This region corresponds to $l/\delta > 0.01$ in the 70 km altitude solution (see Fig. 7.3(a)) and $l/\delta > 0.02$ in the 62 km altitude simulation (see Fig. 7.3(b)). In the immediate vicinity of the wall ($553.3 < T < 1500$ K), R_1 is not active. On the other hand, R_4 attains large values in this region and it is a major contributor to N_2 recombination. Over all, the contribution of the three body recombination of N atoms towards N_2 formation in the boundary layer is negligible at all the conditions studied in this work.

The sustainability of N_2 recombination via reaction (4) depends on the availability of NO molecules, which can be produced by either backward reaction (3): N + O + M $\rightarrow$ NO + M or backward reaction (5): O_2 + N $\rightarrow$ NO + O. A preference for one of these reactions over the other at different altitudes is explained by the following analysis. At 70 km altitude condition, the gas in the boundary layer is mainly composed of N_2, N and O; their concentrations are of the order 10^{-4} kg-mole/m^3 (see Fig. 7.4). The concentrations of the remaining two species, O_2 and NO are comparatively lower and they are around 10^{-7} kg-mole/m^3. The above numbers are representative of the gas composition in the majority of the boundary layer. Reaction (3) proceeds primarily in the backward direction and its rate can be approximated as $R_3 \approx k_{b_3} C_{\mathrm{N}} C_{\mathrm{O}} C_M$. Assuming N_2, N and O as the primary collision partners yields $R_3 \approx k_{b_3} 10^{-12}$. In a similar way, the rate of reaction (5) can be approximated as $R_5 \approx k_{b_5} C_{\mathrm{N}} C_{\mathrm{O}_2} \approx k_{b_5} 10^{-11}$. The backward rate constant $k_{b_3} \approx 10^2 k_{b_5}$ for the range of temperatures observed in the boundary layer. This results

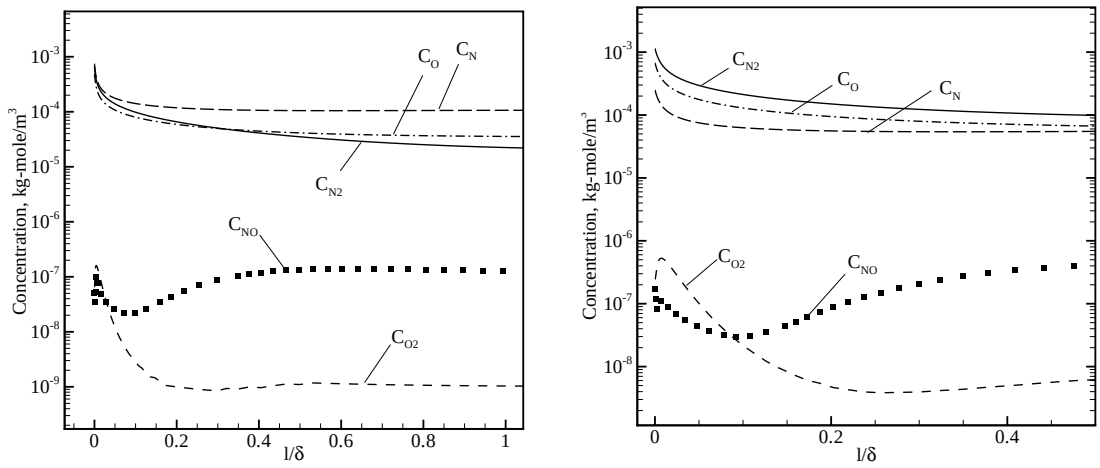

Figure 7.4: Variation of concentration of the species in the boundary at (a) 70 km and (b) 62 km altitude conditions.

in R_3 being 10 times higher than R_5. Therefore, N_2 recombination mechanism consisting of reactions (3) and (4) is preferred at 70 km altitude condition as discussed in Sec. 5.2.1

It is observed that the magnitude of R_5 increases at lower altitudes and it is comparable to R_3 when

$$k_{b_5} C_{\mathrm{N}} C_{\mathrm{O_2}} \approx k_{b_3} C_{\mathrm{N}} C_{\mathrm{O}} C_{\mathrm{M}} \tag{7.1}$$

At relatively high altitudes (62-70 km), the dominant species in the boundary layer are N_2, N and O, (see Fig. 7.4) and the changes in their concentration for varying altitudes are relatively low. On the other hand, O_2 is present at very low levels, and the changes in $C_{\mathrm{O_2}}$ with altitude are large compared to its magnitude. The variation in O_2 concentration is found to affect the magnitude of R_5 considerably (Eq. 7.1). It can be seen that

$$C_{\mathrm{O_2}} \approx \frac{k_{b_3}}{k_{b_5}} C_{\mathrm{O}} C_{\mathrm{M}} \approx 10^2 C_{\mathrm{O}} C_{\mathrm{M}} \tag{7.2}$$

results in $R_5 \approx R_3$. This is observed at the 62 km altitude condition, where the concentrations of N_2, N and O in the boundary layer are comparable to those of the 70 km case (of the order 10^{-4} kg-mole/m^3). The concentration of O_2 at 62 km altitude is of the order 10^{-6} kg-mole/m^3 (see Fig.7.4(b)), and it satisfies Eq. 7.2. The rates of reaction (3) and (5) are therefore comparable; both R_5-R_4 and R_3-R_4 mechanisms contribute to N_2 recombination in the boundary layer.

As shown above, the preference for R_5 over R_3 depends on the local concentration of O_2 in the boundary layer. If $C_{\mathrm{O_2}} > 10^{-6}$ kg-mole/m^3 then $R_5 > R_3$. This is observed in the

altered reactivity simulations, when the rate constant of O_2 recombination is enhanced (rsf = 10 simulations at 70 km and 62 km). Similar observation is also made when the rate constants of all five reactions are increased at the intermediate and higher altitude conditions. In these simulations, concentration of O_2 exceeds 10^{-6} kg-mole/m^3 and R_5-R_4 mechanism of N_2 formation is preferred over R_3-R_4 mechanism in the boundary layer. In the baseline simulation of 35 km altitude case, R_3 is negligible in the boundary layer; N_2 recombination occurs via R_5-R_4 mechanism in the region $0.24 < l/\delta < 0.45$ (see Fig.7.3(c)).

The above N_2 recombination mechanisms can be summarized as follows. As the vehicle descends into atmosphere the stagnation enthalpy of the flow decreases. Hence the dissociation level of N_2 and O_2 decreases; C_{O_2} increases and C_N decreases. This combination favors the R_5-R_4 mechanism. Hence the contribution of this mechanism to the N_2 recombination progressively increases as the altitude decreases. In the present study, at 70 km altitude R_5-R_4 mechanism contributes very little to N_2 formation where as at the lower altitude (35 km) only R_5-R_4 mechanism results in the N_2 recombination.

Recombination of O_2 occurs in the boundary layer via backward reaction (2): O + O + M $\rightarrow$ O_2 + M at temperatures below 4000 K. O_2 molecules act as a catalyst in the conversion of N atoms to N_2 via reaction (5). Therefore, accumulation of O_2 is not observed until N atoms are completely depleted from the gas mixture. At high and intermediate altitude simulations presented here, recombination of N_2 is not complete in the boundary layer. As a result, mass fraction of O_2 remains at negligible levels. At lower altitudes, for example, at 35 km altitude condition, N_2 recombination is mostly complete in the region $0.24 < l/\delta < 0.45$ (see Fig. 7.3(c)). Reaction (2) picks up for $l/\delta < 0.24$ and reaches peak values very close to wall. The rates of other reactions are small compared to reaction (2). As a result, O_2 build up in the near wall region and Y_{O_2} high values at the wall.

7.2 Degree of Non-equilibrium

7.2.1 Thermal Non-equilibrium

Across a shock wave, kinetic energy of the gas first converts into translational energy. Energy exchange between the translational and vibrational modes results in an increase in the vibrational energy. Thus vibrational temperature lags behind the translational temperature resulting

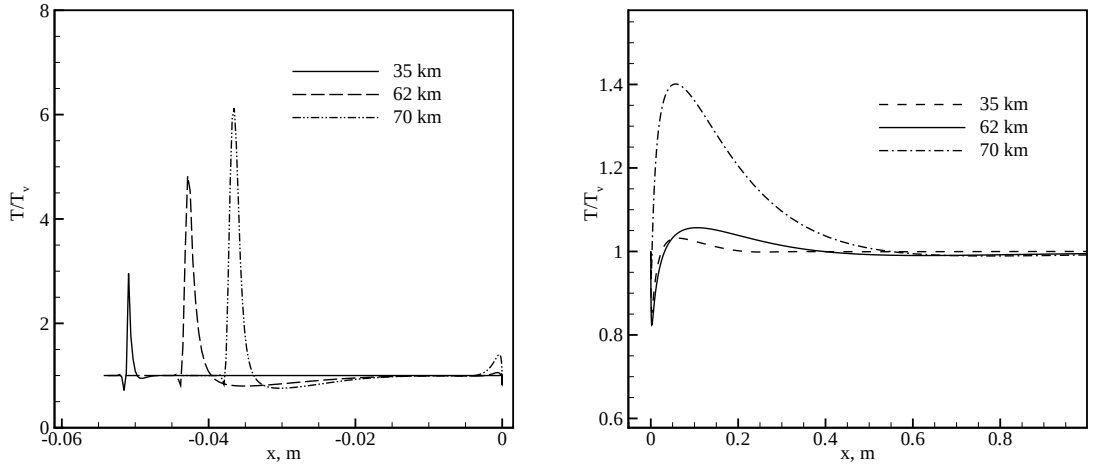

Figure 7.5: Extent of thermal non-equilibrium along the stagnation streamline at 35 km, 62 km and 70 km altitude conditions. (a) shock layer (b) boundary layer

in a thermal non-equilibrium state. Figure 7.5(a) shows the temperature ratio T/T_v along the stagnation streamline. It attains high values at the shock wave for all the three test cases. The peak value of the temperature ratio is 2.95 at the 35km condition. At 62 and 70 km conditions, peak values of the temperature ratio are 4.82 and 6.13 respectively. Thus, the degree of thermal non-equilibrium, as indicated by the magnitude of T/T_v, increases with altitude. This is because of a decrease in the freestream density at higher altitudes (see Tables 3.1, 5.1 and 6.1).

Translational and vibrational temperatures attain comparable values downstream of the shock wave. At the 35 km condition, the gas reaches equilibrium ($T = Tv$), immediately behind the shock wave. At higher altitudes, it takes longer to reach thermal equilibrium. The gas is in thermal non-equilibrium state ($T \neq T_v$) in majority of the shock layer. This is once again due to the relatively low post-shock density at the high altitude conditions.

Decrease of gas temperature in the boundary layer increases the gas density by an order of magnitude compared to the post shock value. Hence the degree of thermal non-equilibrium in the boundary layer is lower than that in the shock layer (see Fig. 7.5(b)). At the lowest altitude condition, the gas is in thermal equilibrium ($T \approx T_v$) in the entire boundary layer. Similarly, the degree of thermal non-equilibrium is negligible ($T/T_v < 1.1$) in the intermediate altitude solution. On the other hand, at the highest altitude condition, the gas is in thermal non-equilibrium state in a significant portion of the boundary layer. Local gas density in this case is not high enough for adequate energy exchange between the translational and vibrational modes.

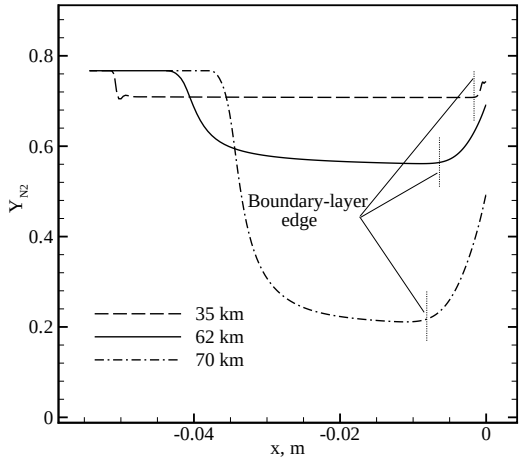

Figure 7.6: Variation of Y_{N_2} along the stagnation streamline at 35 km, 62 km and 70 km altitude conditions.

Note that the temperature ratio falls below 1 in the immediate vicinity of the wall. Recombination reactions occurring in this region produce molecules with finite vibrational energy. This increases the vibrational energy of the gas mixture, which results in $T_v > T$. At the wall, both T and T_v attain the isothermal wall temperature specified in the simulation.

7.2.2 Chemical Non-equilibrium

Similar to thermal non-equilibrium discussed above, the chemical state of the gas is also determined by its density. Figure 7.6 shows the variation of Y_{N_2} along the stagnation streamline for the three cases. In the 35 km solution, the mass fraction attains a value of 0.71 immediately behind the shock wave and remains constant thereafter. The constant value corresponds to the local equilibrium composition. Thus, the gas is in chemical equilibrium in the entire shock layer.

At 62 km, there is a rapid drop in Y_{N_2} at the shock wave followed by gradual decrease in the mass fraction. It reaches a value of 0.56 at the boundary-layer edge, which is higher than the local equilibrium value. Mass fractions of the other species follow identical trend. Variation of gas composition at 70 km altitude is similar to that of 62 km case (see Fig. 7.6), as the gas density is of the same order in the two simulations. However, the degree of dissociation is much higher at the higher altitude condition due to the higher stagnation enthalpy. Mass fraction of N_2 drops to 0.22 at the boundary-layer edge, which is again higher than the local equilibrium value. Hence, the gas is in chemical non-equilibrium state in majority of the shock layer at both

62 km and 70 km altitude conditions.

Table 7.1: Gas composition and extent of recombination at the stagnation point for three altitude conditions.

Altitude	$(Y_{N_2})_w$	$(Y_{O_2})_w$	$(Y_{N_2})_{EQ}$	$(Y_{O_2})_{EQ}$	χ
35 km	0.74	0.18	0.767	0.233	0.92
62 km	0.69	1.7×10^{-4}	0.767	0.233	0.69
70 km	0.49	6.0×10^{-4}	0.767	0.233	0.49

Figure 7.6 also shows the variation of Y_{N_2} in the near-wall region. The N_2 mass fraction increases in the boundary layer for all three cases. Same is true for O_2 mass fraction. As explained above, this is due to the recombination reactions occurring in the boundary layer. Mass fractions of N_2 and O_2 at the wall are compared to their equilibrium values in Table 7.1. The equilibrium composition corresponds to the wall condition for the three test cases. The degree of chemical non-equilibrium at the wall can be quantified as

$$\chi = \frac{(Y_{N_2} + Y_{O_2})_{wall}}{(Y_{N_2} + Y_{O_2})_{EQ}}, \tag{7.3}$$

which is the ratio of molecular mass fraction (N_2 and O_2) computed at the wall to the corresponding equilibrium value.

The equilibrium composition corresponding to the specified isothermal cold-wall temperature is identical to the freestream gas composition. It therefore represents maximum attainable mass fractions of the molecular species. Thus, the parameter χ represents the extent of recombination at the wall, and a value of $\chi = 1$ corresponds to complete recombination. At 35 km condition, the computed values of Y_{N_2} and Y_{O_2} are close to their equilibrium levels (see Table 7.1). For the 62 km case, oxygen is completely in its atomic state at the wall and recombination of nitrogen atoms is partially complete. The mass fractions of molecules are therefore far from their equilibrium values. A similar trend is observed at 70 km condition. Note that the equilibrium composition for the specified wall temperature ($T_w = 553.5$ k) is independent of pressure and therefore is same at the three cases.

The extent of recombination at the wall varies with altitude; χ values for the three cases are listed in Table 7.1. At the lowest altitude condition, recombination of atoms is mostly complete, as indicated by a high value of χ. Therefore the gas is close to the chemical equilibrium state.

This is because of a high gas density at the wall (1.07 kg/m^3). On the other hand, the gas density at the wall is 0.05 kg/m^3 in the intermediate altitude simulation and it is about 20 times lower compared to that at 35 km altitude. As a result, the recombination reactions are partially complete and the gas is in chemical non-equilibrium state at the wall. Similarly, boundary layer chemistry is in non-equilibrium state at the 70 km condition. However, the degree of non-equilibrium is the highest for this case, as indicated by a low value of χ (see Table 7.1).

The flow expansion from the nose stagnation region to the shoulder and further to the afterbody is associated with decrease of pressure, temperature and density. The decrease of temperature promotes recombination reactions in the outer inviscid flow. However the decrease of density inhibits the chemical reactions to occur at a faster rate. Thus degree of non-equilibrium in the shock layer progressively increases from the nose stagnation point to the shoulder. A similar effect is observed in the boundary layers which are located away from the nose stagnation region. Hence the extent of recombination at the wall progressively decreases from the nose stagnation point to the shoulder (see Sec. 4.2.3). On the afterbody, density of the gas is one order of magnitude lower than freestream value ($\rho_{afbd} = 0.1\rho_\infty$). At these density levels, chemical reactions occur at very slow rate and gas can be treated as in chemically frozen state. Hence recombination reactions do not occur in the boundary layer and gas composition freezes at the edge values (see Fig. 4.12(a)).

7.3 Heating Rate Variations

Heating rate to the vehicle surface can be written in terms of the temperature and thermal conductivity of the gas adjacent to the wall.

$$q = -\kappa \frac{\partial T}{\partial \eta} = -\kappa \frac{T_2 - T_w}{\triangle \eta} \tag{7.4}$$

where T_2 is the gas temperature at the first cell next to the wall, T_w is isothermal wall temperature and $\triangle\eta$ is wall-normal distance. The thermal conductivity κ is function of the gas composition next to the wall. The near-wall gas composition and temperature are directly influenced by chemical reactions occurring in the boundary layer. They are also affected by the gas temperature and composition at the edge of the boundary layer. The boundary-layer edge conditions in turn depends on the shock-layer chemistry.

The shock-layer chemistry is dominated by dissociation of molecules and these are endothermic in nature. On the other hand, boundary layer chemistry is dominated by exothermic

Table 7.2: Contribution of $\triangle\kappa/\kappa$ and $\triangle T_2/(T_2 - T_w)$ to $\triangle q/q$ at the nose stagnation point for the three altitudes.

	35 km		62 km		70 km	
% change	rsf=10	rsf=0.1	rsf=10	rsf=0.1	rsf=10	rsf=0.1
$\triangle\kappa/\kappa$	1.91	-4.61	-3.50	5.70	-16.79	9.42
$\triangle T_2/(T_2 - T_w)$	0.48	-4.08	38.10	-31.55	76.00	-49.85
$\triangle q/q$	2.40	-8.50	33.40	-27.65	46.46	-45.08

recombination reactions. These reactions are driven by the cold wall temperature specified in the simulation. The boundary-layer chemistry is independent of variations in the wall temperature for values around 550 K. This is because of the fact that chemical activity in the gas mixture ceases at such low temperatures.

The chemical reactions in the boundary layer are determined by the gas composition at the boundary-layer edge. For the conditions considered in this work, the edge temperature is in the range of 5500 to 6500 K (see Fig. 7.2(b)). Majority of the recombination occurs in the near-wall region ($l/\delta < 0.1$), where the gas temperature is between 1000 and 2000 K. It is therefore observed that boundary-layer chemistry is relatively insensitive to the edge temperature.

When the reaction rates are altered from their baseline values, the variation in heating rate can be expressed as

$$\frac{\triangle q}{q} = \frac{\triangle \kappa}{\kappa} + \frac{\triangle T_2}{T_2 - T_w} \tag{7.5}$$

The quantities T_w and $\triangle\eta$ in Eq.7.4 are identical in the baseline and altered reactivity simulations. The variation in the near wall gas temperature ($\triangle T_2$) depends on the heat release in the exothermic recombination reactions. Mixture conductivity is determined by the gas composition in the near-wall region, which in turn depends on the extent of chemical reactions in the boundary layer. The contribution of $\triangle T_2$ to the variation in surface heat flux is usually higher compared to that of $\triangle\kappa$ (see Table. 7.2).

7.3.1 Critical Factors

The surface heat flux variations due to the uncertainty in reaction rates depends on the following three factors: (1) the dominant chemical reaction(s) in the gas mixture; (2) the chemical state of

the gas–equilibrium, non-equilibrium or frozen; (3) the extent of recombination in the boundary layer. In the boundary layer, an increase in the rate constants enhances the recombination reactions and it results in a higher heat release. This enhances the near-wall gas temperature, which has a tendency to increase the surface heating rate over the baseline level. The higher reaction rates also increase the molecular mass fractions in the gas, which may increase or decrease the thermal conductivity at the wall. Opposite effects are observed when the rate constants are decreased, leading to a decrease in the stagnation point heat flux (see Table. 7.2).

The effect of shock-layer chemistry on the surface heat flux exhibit a trend that is opposite to the boundary-layer effect. A higher reactivity enhances the endothermic dissociation reactions at the shock wave. This results in a lower gas temperature at the boundary-layer edge, which tends to reduce the surface heat flux. Decreasing the reaction rates has an opposite effect. Altering the dissociation rate constants in the shock layer affects the gas composition at the boundary-layer edge. The resulting mass fractions of different species at the edge of the boundary-layer has a significant effect on the surface heat flux, as mentioned above. It is observed that the changes in the heating rate to the variation in rate constants is higher when the gas is in chemical non-equilibrium state. On the other hand, if the gas is in chemical equilibrium or frozen state, the changes in the heat flux are relatively less.

A brief summary of the variation in heating rate at the nose stagnation point for the 35 km, 62 km and 70 km is presented. The effect of above factors are highlighted at each trajectory point. The specific rate constants to which the heating rate is sensitive to at the three conditions are given below.

7.3.2 Heating Rate Variations at the Nose Stagnation Point

At 35 km altitude, the stagnation enthalpy and density of the flow is 12 MJ/kg and 0.0082 kg/m^3. The dominant chemical activity in the shock layer is dissociation of oxygen molecules and recombination of oxygen atoms in the boundary layer. Due to high post-shock density, thermo-chemistry in the shock layer approaches equilibrium. Increasing and decreasing the rate constants doesn't change the boundary-layer edge conditions. Thermo-chemical state of the gas in the boundary layer is close to equilibrium with a high degree of recombination at the wall (see Table. 7.1). The near-wall gas composition and temperature change marginally when the rate constants are increased and the resulting enhancement in surface heating rate is small (see Table. 7.2). When the rate constants are decreased, recombination of oxygen atoms

is suppressed. The corresponding variations in κ and T_2 are given in the Table. 7.2. The overall reduction in heating rate is relatively higher. Note that the heating rate is influenced by only oxygen atom recombination rate, k_{b_2} in the boundary layer.

At 62 km trajectory point, the stagnation enthalpy and density of the flow are 19.2 MJ/kg and 0.000281 kg/m^3. The primary chemical activity in the shock layer is partial dissociation of N_2 molecules along with a complete dissociation of O_2 molecules. The chemistry is dominated by forward reactions 2, 3 and 4 in the shock layer. Reaction 2 results in complete dissociation of O_2 molecules, and variation in k_{f_2} has no appreciable effect on the flowfield solution. The magnitude of R_3 and R_4 determine the degree of N_2 dissociation in the shock layer. Composition of the gas, specifically Y_{N} and Y_{N_2} at the boundary-layer edge is sensitive to the variation in k_{f_3} and k_{f_4}. In the boundary layer, partial recombination of N atoms is observed and reactions 2, 3, 4 and 5 participate in this process. Reactions 2 and 3 are rate limiting steps. Hence heating rate is mainly affected by a variation in the corresponding rate constants, k_{b_2} and k_{b_3}. Further the gas is in non-equilibrium state in the shock layer as well as in the boundary layer. Variations in the rate constants therefore result in large changes in the near-wall gas temperature (see Table. 7.2). The corresponding changes in the surface heat flux are significantly larger than those of the lower altitude case.

The stagnation enthalpy and density of the flow at 70 km altitude are 31.53 MJ/kg and 0.000152 kg/m^3. Thermo-chemistry is similar to that of 62 km case, but the degree of N_2 dissociation in the shock layer is larger. Also reaction 1 has a major contribution at the shock wave, that is not observed at the intermediate altitude condition. Shock-layer solution is therefore sensitive to k_{f_1}, k_{f_3} and k_{f_4}. Boundary-layer chemistry is once again dominated by N_2 recombination, with reactions 2 and 3 as rate limiting steps. Thus the heating rate changes are influenced by the backward rate constants k_{b_2} and k_{b_3}. Trends in $\triangle\kappa$ and $\triangle T_2$ are similar to 62 km case, but higher heat flux variations are observed due to higher degree of non-equilibrium (see Table. 7.2).

7.3.3 Effect of Stagnation Enthalpy

In summary, it is found that the changes in heating rate to the variation in rate constants depends on the stagnation enthalpy and density of the flow. As the vehicle descends into atmosphere its velocity decreases consequently stagnation enthalpy of the flow decreases. H_0 determines the level of dissociation in the shock layer, which in turn determines the recombination process

in the boundary layer. At low H_0, only recombination of O_2 is observed. At intermediate H_0, recombination of O_2 and N_2 occur. At higher H_0, only N_2 recombination is observed. The reaction mechanisms involved in the recombination process and the rate limiting steps are enthalpy dependent. At low enthalpies (around 12 MJ/kg), heating rate is affected by only k_{b_2}. At intermediate and high H_0 (between 19 and 32 MJ/kg), heat flux is influenced by both k_{b_2} and k_{b_3}. Based on similar analysis, the shock layer chemistry at high H_0 (around 32 MJ/kg) is found to be sensitive to k_{f_1}, k_{f_3} and k_{f_4}, which are involved in N_2 dissociation. As the enthalpy decreases, the contribution of reaction 1 to N_2 dissociation decreases. Therefore the flowfield solution in the shock layer is sensitive to only k_{f_3} and k_{f_4} for flow enthalpies around 19 MJ/kg. At low enthalpies (around 12 MJ/kg), the shock layer chemistry is sensitive to k_{f_2}, rate constant of oxygen dissociation. For the entire range of H_0 considered in this work the forward rate constants of reaction 5 don't alter the surface heat flux noticeably.

7.3.4 Effect of Density

The gas density determines the chemical state of the gas in the flowfield. When the gas is in equilibrium state increasing the rate constants has a small effect on the gas properties and the surface heat flux. On the other hand, decreasing the rate constants lowers the heating rate significantly. Opposite is true when the gas is in frozen chemical state. Decreasing reaction rates has a negligible effect here, whereas there is noticeable increase in heating rate when the reaction rates are enhanced. When gas is in non-equilibrium state, both increasing and decreasing the reaction rates have significant effect on the gas properties and on heat transfer rate. Hence level of heat flux variations to the uncertainty in rate constants depends on density of the gas.

7.4 Summary

The thermo-chemistry along the stagnation streamline of a re-entry flowfield is analyzed as a function of the altitude. Dissociation of oxygen occurs via Reaction (2), on the other hand N_2 dissociation can happen through Reactions (1), or (4), or both. As enthalpy of the flow increases the contribution of Reaction (1) to the N_2 dissociation increases. Recombination reactions occur in the boundary layer, which are function of the gas composition at the boundary-layer edge. First recombination of N atoms occurs through Reaction (4) which requires NO as a reactant.

NO is produced by either Reaction (3) or (5). The concentration of oxygen molecules determine the preference for either of these two reactions. When the nitrogen atoms are completely depleted from the gas mixture, oxygen recombination occurs via Reaction (2). The degree of thermo-chemical non-equilibrium in the shock layer increases with the increase of altitude. The degree of chemical non-equilibrium is quantified in terms of extent of recombination at the wall. A higher value of extent of recombination at the wall is observed at the 35 km condition due to higher gas density. The heating rate is influenced by only oxygen atom recombination rate, k_{b_2} in the boundary layer at the 35 km altitude condition. At higher altitude conditions, heating rate is mainly influenced by the rate limiting steps in the N_2 recombination $i.e.$ Reactions (2) and (3). The heating rate variations are large at these conditions due to relatively low gas density, where as at the low altitude condition, the changes in the heat flux are lower due to high gas density.

Chapter 8

Conclusions and Future Work

8.1 Conclusions

At high temperatures, the closure of species mass, vibrational and total energy conservation equations require chemical reaction rate constants. These parameters are usually measured in shock or ballistic tunnels. Hence, there is always some amount of uncertainty in their measurement. Previous research has shown that uncertainty in the rate constants can lead to a significant variation in the re-entry flow features and associated surface properties. In this thesis, an attempt has been made to study the effects of variation in the rate constants on the computed flowfield and associated surface properties at flight conditions. The objective is to understand the underlying physical mechanisms and to identify the critical factors which influence the sensitivity of aero-heating predictions to the variation in chemical reaction rate constants. The study is performed at three trajectory points. These points represent low, intermediate and high altitude conditions in an earth re-entry trajectory.

High enthalpy flowfield over a re-entry capsule is simulated by solving Navier-Stokes equations along with the species conservation equations and a thermal non-equilibrium model. Finite rate chemistry is considered with Arrhenius rate constants evaluated using curve fits of Park to experimental data. An In-house CFD code based on finite volume method is used to compute the flowfields. Implicit time integration, along with a data parallel implementation, is used to reach steady state results. The code has implicit and parallel capabilities and has been applied to several hypersonic configurations. The re-entry flow computations are validated against the FIRE II flight data at 35 km condition. The predicted heating rate at nose stagnation point and on the conical frustum compare well with the in-flight measurements.

The computed solutions are analyzed in detail in terms of the gas properties and chemical activity in different parts of the flowfield. Increase of gas temperature across the shock wave initiates endothermic dissociation reaction, where as the decrease of gas temperature in the thermal boundary layer adjacent to vehicle wall results in recombination reactions. Similarly decrease of temperature due to flow expansion result in exothermic recombination reactions. Thus, the nature of chemical reactions in a re-entry flowfield is determined by the gas dynamic processes. The energy released or absorbed in the chemical reactions in turn affects the local gas temperature. The reactions also alter the gas composition which influences the mixture density, viscosity and conductivity. Thus, there is a two-way influence between the gas dynamics and chemical reactions in a re-entry flowfield. This mutual interaction plays an important role in understanding the effect of varying reaction rates on aero-heating predictions.

The sensitivity of aero-heating predictions to the variations in reaction rate constants depends on the dominant chemical reactions occurring in the flowfield. The stagnation enthalpy of the flow determines the amount of dissociation in the shock layer. At low enthalpy condition, corresponding to 35 km altitude trajectory point, dissociation of oxygen molecules at the shock wave and recombination of oxygen atoms in the boundary layer are the primary reactions. For higher altitude cases, dissociation of N_2 is noticed in addition to dissociation of oxygen molecules. Varying degree of nitrogen dissociation is observed depending on the total enthalpy of the flow. The recombination reactions in the boundary layer depends on the gas composition at the boundary-layer edge. In the presence of nitrogen atoms, nitrogen recombination occurs first, for example, at 62 and 70 km altitude conditions. When the nitrogen atoms are completely depleted from the gas mixture, recombination of the oxygen atoms is observed.

Changes in aero-heating predictions are investigated by systematically varying the reaction rates over their uncertainty range. The flow solutions computed by altering the reaction rates are carefully analyzed to understand the physical effects that influence the surface heat transfer rate. In general, an increase in rate constants increases the chemical activity in the flowfield. Particularly, the recombination reactions in the boundary layer are enhanced. The corresponding heat release enhances the near-wall gas temperature. This elevates the heat flux. An opposite effect is observed when the rate constants are decreased.

The magnitude of the heating rate variation depends on the local chemical state of the gas –equilibrium, non-equilibrium or frozen. This in turn is a function of the gas density which varies by almost three orders of magnitude in a re-entry flowfield. When the gas is in chemical

equilibrium state, the reactions are complete. Increasing the rate constants further has a small effect on the gas properties and the surface heating rate remains unaltered. This is observed at the nose stagnation point of 35 km altitude solution. On the other hand, when the gas is in non-equilibrium state, the recombination/dissociation processes is partially complete. An increase in rate constants can therefore induce significant changes in the gas properties. This can lead to large variation in the heat flux predictions. Similarly, decrease in rate constants suppresses the recombination reactions and therefore heating rate decreases significantly. This trend is observed at the shoulder region of 35 km condition, and at the nose stagnation points of the higher altitude cases.

The gas is in chemical frozen state on the afterbody and the extent of recombination is very low. However, the changes in the forebody shock layer, due to variation in rate constants, convect into the afterbody separation bubble. This alters the separation bubble size and the gas properties in the vortex core. The resulting changes in gas temperature and composition at the boundary layer edge influence the surface predictions. For example, the reduced reactivity simulation at 62 and 70 km altitude results in base pressure and heat flux that are much higher than the baseline values. This is because of a hotter gas in the forebody shock layer, due to reduced dissociation level, which is convected to afterbody and alters the surface predictions significantly.

In summary, the analysis presented in the thesis identifies three critical factors that determines the variation in aero-thermodynamic predictions due to changes in chemical reaction rates.

1. The dominant chemical reactions occurring in the shock layer, the shoulder expansion region and the thermal boundary layer on a re-entry capsule.

2. The local chemical state of the gas – equilibrium, non-equilibrium, frozen – in different parts of the reentry flowfield.

3. The extent of recombination achieved at the isothermal wall boundary.

It is found that the stagnation enthalpy of the flow and the free-stream density are the parameters which control the interaction between the gas dynamics and chemical reactions in the flow. The variation of these two parameters at different flight conditions spanning a re-entry trajectory and their influence on the heat flux prediction is discussed.

Based on the analysis presented in the thesis and the specific conclusions drawn from the work, the following directions of future work are envisaged.

8.2 Future Work

1. Catalysis of thermal protection system material is another important parameter which affects the heat transfer rate. The catalysis promotes the recombination reactions at the surface, thus providing another path for the formation of molecules on the surface. In this way, catalysis affects the extent of recombination at the wall. Therefore, the heating rate variations due to uncertainty in the rate constants with a catalytic wall will be different than those obtained with a non-catalytic wall. Similar to the rate constants, there is an uncertainty in the measurement of catalytic properties of the wall. Variation in the wall catalycity changes the amount of recombination at the surface, and hence heating rate. The present analysis can be extended to investigate the above catalytic effects on heat flux variations.

2. Diffusion process has a significant effect on the boundary-layer gas composition. Molecules (either N_2 or O_2) are created in close proximity to the wall due to the recombination reactions, and the diffusion phenomena propagates or moves the molecules from high concentration region to low concentration regions. A variation in diffusion coefficients can therefore alter the gas composition in the near-wall region. This can have a significant effect on the reaction mechanisms and heat flux. These variations could be much higher if the surface is catalytic. An analysis similar to that presented in the thesis, can be performed to understand the effects of diffusion on chemical reactions and heat flux on catalytic and non-catalytic surfaces.

3. Stagnation enthalpy (H_O) of the flow in a freestream determines the chemical kinetics at the shock wave. For Earth entry, if H_O is above 30 MJ/kg, ionization of the species occur in addition to chemical reactions at the shock wave. Depending on the level of ionization air can be modeled as a mixture of seven species (N_2, O_2, NO, N, O, NO^+ and e^-) or eleven species (N_2, O_2, NO, N, O, NO^+, O^+, N^+, N_2^+, O_2^+ and e^-). Ionization process posses many challenges to computational predictions. The energy exchange mechanisms between electrons, atoms and molecules should be considered and appropriate energy ex-

change terms should be included in the mixture vibrational and total energy equations. The present procedure can be extended to identify the critical reactions affecting the electron number density and heat transfer rate at ionization conditions.

References

[1] Gnoffo, P.A., Weilmuenster, K.J., Hamilton II, H.H., Olynick, D.R., and Venkatapathy, E., "Computational Aerothermodynamic Design Issues for Hypersonic Vehicles," *Journal of Spacecraft and Rockets*, Vol. 36, No. 1, January-February 1999, pp. 21-43.

[2] Nompelis, I., Candler, G.V., "Investigation of Hypersonic Double-cone Flow Experiments at High Enthalpy in the LENS Facility," AIAA Paper 2007-0203, 2007.

[3] Anderson Jr., J.D., "Hypersonic and High Temperature Gas Dynamics", AIAA Education series, 1989.

[4] Schneider, S.P., "Laminar-Turbulent Transition on Reentry Capsules and Planetary Probes," *Journal of Spacecraft and Rockets*, Vol. 43, No. 6, November-December 2006.

[5] Fay, J.A., and Riddell, F.R., "Theory of Stagnation Point Heat Transfer in Dissociated Air," *Journal of the Aeronautical Sciences*, Vol. 25, No. 2, February 1958, pp. 73-85.

[6] Pratt, D.T., Radhakrishnan, K., "Physical and numerical sources of computational inefficiency in integration of chemical kinetic rate equations - etiology, treatment, and prognosis", NASA TP-2590, 1986.

[7] Candler, G.V., "The Computation of weakly ionized hypersonic flows in thermo-chemical nonequilibrium", Ph.D dissertation, Department of Aeronautics and Astronautics, Stanford University, 1988.

[8] Josyula, E., and Shang, S.J., "Numerical study of hypersonic dissociated flow past blunt bodies," *AIAA Journal*, Vol. 29, No. 4, 1990, pp. 704-711.

[9] Park, C., Non-Equilibrium Hpersonic Aerothermodynamics, A Wiely-Interscience Publication, New York, 1990.

[10] Tirskiy, G.A., “Up-to-date gasdynamic models of hypersonic aerodynamics and heat transfer with real gas properties”, Annual reviews of Fluid mechanics, Vol 25, pp.151-81, 1993.

[11] Grasso F., Capano G., “Modeling of ionizing hypersonic flows in nonequilibrium”, *Journal of Spacecraft and Rockets*, Vol. 32, No. 2, March-April 1995, pp. 217-224.

[12] Olejniczak, J., and Candler, G.V., “Vibrational Energy Conservation with Vibration-Dissociation Coupling: General Theory and Numerical Studies”, Phy. Fluids 7 (7), July 1995.

[13] Josyula, E., and Shang, S.J., “Computation of Nonequilibrium Hypersonic Flowfields Around Hemisphere Cylinders,” *Journal of Thermophysics and Heat Transfer*, Vol. 7, No. 4, October-December 1993, pp. 668-679.

[14] Tchuen, G., and Zeitoun, D., “Effects of Chemistry in Nonequilibrium Hypersonic Flow Around Blunt Bodies,” *Journal of Thermophysics and Heat Transfer*, Vol. 23, No. 3, July-September 2009, pp. 433-442.

[15] Nompelis, I., Candler, G.V., Holden, M.S., and Wadhamas, T.P., “Computational Investigation of Hypersonic Viscous/Inviscid Interactions in High Enthalpy Flows,” AIAA Paper 2003-3642, 2003.

[16] Nompelis, I., “Computational Study of Hypersonic Double-cone Experiments for Code Validation”, Ph.D dissertation, Department of Aerospace Engineering, University of Minnesota, 2004.

[17] Dogra, V.K., Moss, J.N., Wilmoth, R.G., Taylor, J.C., Hassan, H.A., “ Effects of Chemistry on Blunt-Body Wake Structure”, *AIAA Journal*, Vol 33, No. 3, 1995, pp.463-469.

[18] Hollis, B.R., “Experimental and Computational Aerothermodynamics of a Mars Entry Vehicle”, NASA-CR-201633, December 1996.

[19] Grasso, F. and Pettinelli, C., “Analysis of Laminar Near-Wake Hypersonic Flows”, *Journal of Spacecraft and Rockets*, Vol 32, No. 6, 1996.

[20] Bose, D., and Wright, M.J., “Uncertainty Analysis of Laminar Aeroheating Predictions for Mars Entries,” AIAA Paper 2005-4682, 2005.

[21] Palmer, G.E., "Uncertainty Analysis of CEV LEO and Lunar Return Entries," AIAA Paper 2007-4253, 2007.

[22] Wright, M.J., Candler, G.V., and Bose, D., "Data-Parallel Line Relaxation Method for the Navier-Stokes Equations," *AIAA Journal*, Vol. 36, No. 9, 1998, pp. 1603-1609.

[23] Blottner, F.G., Johnson, M., and Ellis, M., "Chemically Reacting Viscous Flow Program for Multi-component Gas Mixtures," Sandia Laboratories Report No. SC-RR-70-754, Albuquerque, New Mexico, 1971.

[24] Svehla, R.A., "Estimated viscosities and thermal conductivities of gases at high temperatures", NASA TR R-132, 1962.

[25] Gupta, R.N., Yos, J.M., Thompson, R.A., and Lee, K., "A Review of Reaction Rates and Thermodynamic and Transport Properties for an 11-Species Air Model for Chemical and Thermal Non-equilibrium Calculations to $30,000\ K$", NASA RP-2953, 1990.

[26] Vincenti, W.G., and Kruger, C.H., *Introduction to Physical Gas Dynamics*, Krieger Publications, Malabar, Florida, 1986, pp. 407.

[27] Wilke, C.R., "A Viscosity Equation for Gas Mixtures," *Journal of Chemical Physics*, Vol. 18, 1950, pp. 517-519.

[28] Olejniczak, J., Candler, G.V., Wright, M.J., Hornung, H.G., and Leyva I, "High Enthalpy Double-Wedge Experiments", AIAA Paper 96-2238, 1996.

[29] Marrone, P.V., and Treanor, E.C., "Chemical Relaxation with Preferential Dissociation from Excited Vibrational Levels", $Physics\ of\ Fluids$, Vol 6, Number 9, 1963, pp.1215-1221.

[30] Macheret, S.O., and Rich, J.W., "Nonequilibrium dissociation rates behind strong shock waves: Classical model", $Journal\ of\ Chemical\ Physics$, 174, 1993, pp. 25-43.

[31] Park, C., "Assessment of Two-temperature Kinetic Model for Dissociating and Weakly Ionizing Nitrogen" , AIAA paper 86-1347, 1986.

[32] Lee, J.H., "Basic Governing Equations for the Flight Regime of Aero assisted Orbital Transfer Vehicles, Thermal Design of Aero assisted Orbital Transfer Vehicles", ed H.F. Nelson, Progress in Aeronautics and Astronautics, Vol 96.

[33] Millikan, R.C., and White, D.R., "Systematics of Vibrational Relaxation", $Jouranal\ of\ Chemical\ Physics$, Vol. 39, 1963, pp. 3209-3213.

[34] Spalart, P.R., and Allmaras, S.R., "A One-equation Turbulence Model for Aerodynamic Flows," AIAA Paper 92-0439, 1992.

[35] MacCormack, R.W., and Candler, G.V., "The Solution of the Navier-Stokes Equations Using Gauss-Siedel Line Relaxation," *Computers and Fluids*, Vol. 17, No. 1, 1989, pp. 135-150.

[36] Slocumb, T.H., "Project FIRE Flight II Afterbody Temperatures and Pressures at 11.35 Kilometers per Second," NASA TM X-1319, 1966.

[37] Lees, L., "Hypersonic Wakes and Trails," *AIAA Journal*, Vol. 2, No. 3, March 1964.

[38] Wright, M.J., Loomis, M., and Papadopoulos, P., "Aerothermal Analysis of the Project Fire II Afterbody Flow," *Journal of Thermophysics and Heat Transfer*, Vol. 17, No. 2, April-June 2003.

[39] Wright, M.J., Prabhu, D.K., and Martinez, E.R., "Analysis of Apollo Command Module Afterbody Heating Part I: AS-202," *Journal of Thermophysics and Heat Transfer*, Vol. 20, No. 1, January-March 2006.

[40] Sinha, K., "Reynolds-Averaged Navier-Stokes Simulation of Fire II Re-entry Configuration," 25^{th} *International Symposium on Shock Waves*, Indian Institute of Science, Bangalore, India, 2005.

[41] Cornette, E.S., "Forebody Temperatures and Calorimeter Heating Rates Measured During Project FIRE II Reentry at 11.35 Kilometers per Second," NASA TM X-1305, 1966.

[42] Richardson, N.R., "Project FIRE Instrumentation for Radiative Heating and Related Measurements," NASA TN D-3646, 1966.

[43] Bourdon, C.J., Smith, K.M., Dutton, J.C., and Mathur, T., "Planar Visualization of Large Scale Turbulent Structures in Axisymmetric Supersonic Base Flows," AIAA paper 98-0624, 1998.

[44] Nompelis, I., and Candler, G.V., "Investigation of Hypersonic Double-Cone Flow Experiments at High Enthalpy in the LENS Facility," AIAA Paper 2007-203, 2007.

[45] Saunders, D., Yoon, S., and Wright, M., “An Approach to Shock Envelope Grid Tailoring and Its Effect on Reentry Vehicle Solutions ,” AIAA Paper 2007-207, 2007.

List of Publications Based on Present Work

Refereed Journals

1. Reddy, D.S.K., and Sinha, K., "**Hypersonic Turbulent Flow Simulation of FIRE II Re-entry Vehicle Afterbody**," *Journal of Spacecraft and Rockets*, Vol. 46, No. 4, July-August 2009, pp.745-757.

2. Reddy, D.S.K., and K. Sinha, "**Effect of chemical reaction rates on aero-heating predictions of re-entry flows**," *Journal of Thermophysics and Heat Transfer*, Vol. 25, No. 1, January-March 2011, pp.21-33.

3. Reddy, D.S.K., and Sinha, K., "**Analysis of High-Enthalpy Air-chemistry and its Effect on Stagnation Point Heat Flux**," Under Reivew, *Journal of Thermophysics and Heat Transfer*, June 2011.

4. Reddy, D.S.K., and Sinha, K., "**Effect of Chemical Reaction Rates on High-enthalpy Flow Prediction Around a Re-entry Capsule**," Under Review, *Journal of Thermophysics and Heat Transfer*, June 2011.

Conference Proceedings

1. Reddy, D.S.K., and K. Sinha, "**Hypersonic Turbulent Reacting Flow Simulation of Fire II Re-entry Vehicle**, *AIAA Paper 2007-805, 2007*.

2. Reddy, D.S.K., and K. Sinha, "**Analysis of Non-Equilibrium Thermo-Chemistry in**

Fire II Re-entry FlowField," *34^{th} Fluid Mechanics Fluid Power Conference*, BITS, Ranchi, India, Dec. 10-12, 2007.

3. Reddy, D.S.K., and K. Sinha, "**Effect of Transport Coefficients on Aero-heating Predictions of Re-entry Capsules**," *Fourth Symposium on Applied Aerodynamics and Design of Aerospace Vehicles*, Bengaluru, India, Dec 10-12, 2009.

4. Reddy, D.S.K., and K. Sinha, "**Effect of Chemical Reaction Rates on Aero-heating Predictions of Re-entry Capsules**," *AIAA paper 2010-630, 2010*.

5. Reddy, D.S.K., and K. Sinha, "**Analysis of High-enthalpy Air-chemistry and its Effect on Stagnation Point Heat Flux**," *AIAA Paper 2012-3002, 2012*.

Acknowledgments

I am greatly indebted to **Prof. Krishnendu Sinha** and **Prof. Viren Menezes** for their earnest guidance and kind suggestions during the course of this work. I am thankful to my research committee members Prof. A.W. Date, Prof. A.G. Marathe, Prof. K. Sudhakar, Prof. Preeti Aghalayam, Prof. B.Puranik and Prof. A. Chowdhury for their valuable suggestions and advice. I express my sincere gratitude to Prof. G.R. Shevare who introduced me to my advisor, Prof. Krishnendu Sinha. This facilitated my dream of pursuing a doctoral thesis in my cherished subject *Computational Re-entry Aero-thermodynamics*.

I am indebted to Prof. K.P.J Reddy, Head, Laboratory for Hypersonics and Shock wave Research, Indian Institute of Science, for giving an opportunity to do experiments in the free piston shock tunnel. The help of supporting staff of the lab is highly appreciable. I am thankful to my co-guide, Prof. Viren Menezes for financially supporting these experiments.

I would like to acknowledge Rajhansa Sridhara, an alumni of IIT Bombay, for his assistance in the shock-grid alignment simulations presented in this thesis.

I express my sincere thanks to all my lab mates and fellow doctoral students in the institute, who made my stay at IIT Bombay, a memorable experience. Special thanks to Parag, Murugan, Amjad, Russell, Vijay, Velan, Sreekanth, Vighnesh, Rajhansa, Nitin, Manindar, Nithya, Bala Sridhar, Sarvesh and Bijay Lakshmi, for their technical discussions and friendly conversations.

I would like to express my thanks to Mr. R. Velusamy, Head R&D Engines, Mahindra&Mahindra Ltd, MRV, Chennai for inducting me into their R&D team. I am also overwhelmed by the support given by all my colleagues which greatly helped me to complete thesis writing in time.

Finally, I am grateful to my parents whose moral support during this work has been a constant source of strength that kept me moving forward towards attaining this goal.

This work was assisted through funds granted by Ministry of Human Resources Development, Government of India and Indian Space Research Organization (ISRO) under the RE-

SPOND program.

Date: 18-09-2012

D. Siva Krishna Reddy